THE UNIVERSITY OF CHICAGO

FIRST-PRINCIPLES STUDIES OF WATER AT SEMICONDUCTOR INTERFACES

A DISSERTATION SUBMITTED TO
THE FACULTY OF THE PRITZKER SCHOOL OF MOLECULAR ENGINEERING
IN CANDIDACY FOR THE DEGREE OF
DOCTOR OF PHILOSOPHY

BY
ZIFAN YE

CHICAGO, ILLINOIS
DECEMBER 2023

To my parents

Essentially, all models are wrong, but some are useful.

- George E.P. Box

TABLE OF CONTENTS

LIST OF FIGURES

LIST OF TABLES

ACKNOWLEDGMENTS

Nine years ago, in October, I left my parents for the first time to start a journey of education. At that time, I couldn't have foreseen that in the same October, I would conclude my student years with this doctoral thesis.

Throughout my PhD journey, I have been involved in projects directly relevant to everyday life. This connection has repeatedly convinced me that my research is meaningful. However, as I conclude this thesis, I realize that my years as a PhD student did not contribute to the advancement of the field. I am also uncertain about whether I will continue to pursue a career in research in the future. Nevertheless, the years dedicated to studying fundamental science, along with numerous moments of witnessing brilliant minds pushing the boundaries of human knowledge, will forever remain cherished in my life.

With this in mind, I would like to express my gratitude to the many individuals who have supported me over past years.

Foremost, I am grateful to my advisor Professor Giulia Galli. Her guidance and mentorship have shaped me in every aspects of being an independent researcher.

I am fortunate to have collaborated with exceptional experimental researchers: Professor Bozhi Tian, Dr. Aleksander Prominski, Professor Yuanwen Jiang for their invaluable contributions.

My appreciation extends to the friends I had the privilege of meeting in London and Chicago. Their colorful life experiences have illuminated my life.

Lastly, I would like to express my deepest gratitude to my parents Lin Ye and Yan Li, who believe that education is not solely about making a living, but about having the right to make choices. Their 27 years of investment and unwavering support, have empowered me with freedom to pursue my dreams.

ABSTRACT

Water plays an essential role in many physical and chemical processes, in addition to being the so-called molecule of life. For example, in several batteries, photoelectrochemical cells, and bioelectronic devices, solid-water interfaces are present and critically influence the devices' properties. Water also plays a key role in geochemical processes. It constitutes a major portion of the Earth's crust and mantle, participating in geological phenomena under high-pressure, high-temperature conditions, including metasomatism, carbon transport, and continental crust evolution. To understand the electronic characteristics and structural modifications of water molecules at interfaces or in extreme environments, computational modeling at the atomistic scale is an essential tool.

In this thesis, we employed first-principles molecular dynamics simulations to study semiconductor-water interfaces and water under extreme conditions. We focused on hydrogenated silicon (Si) surfaces interfaced with water, given silicon's widespread use in electronic devices, including photocathodes. Furthermore, we investigated water under pressures and conditions relevant to the Earth's interior (11 GPa and 1000 K).

In our interfacial studies, we explored the electronic structure of the hydrogenated Si(100) and water interfaces by performing first-principles molecular dynamics simulations in the presence of an electric field. We correlated the computed flat-band potential and tunneling current images at the interface with experimentally measured capacitive and Faradaic currents. Consistent with chronoamperometry measurements, our simulations indicate that the capacitive currents at the interface are voltage-dependent, while the Faradaic currents are weakly dependent on the applied voltage but are related to surface defects. Next, we investigated the dynamic and vibrational properties of water at the electrified interface. We analyzed the H-bond structures and orientation of water molecules, and we related the structural properties of interfacial water molecules to the OH stretching mode in Raman spectra. The calculated spectra reveal a combined effect of the surface and the electric field

on the Raman features observed at the interface. The presence of the surface leads to low-coordinated hydrogen bonding configurations and, hence, a blue-shift of the O-H stretching band relative to that of bulk water. The electric field regulates the orientation of interfacial water molecules, resulting in a stable H-bond network that gives rise to specific Raman peaks in the low-frequency region of the spectrum. Our computational studies provided comprehensive insights into the electronic and dynamic properties of Si-based electrochemical or photoelectrochemical devices.

In our study of water in extreme conditions, we carried out calculations of photoelectron spectra of water and a simple solution of NaCl under high pressure and high temperature. We combined first-principles and deep-potential molecular dynamics with dielectric-dependent hybrid functionals. We found notable changes in the spectra relative to ambient conditions; in particular, we observed anion energy levels closer to the valence band maximum of the liquid than those observed at ambient conditions, indicating that as pressure and temperature are increased, the defect levels of Cl^- and OH^- in water may eventually lie below the valence band maximum of water. We also elucidated the electronic states associated with proton transfer events at high pressure by calculating the projected density of states. Our results represent an important first step in predicting the electronic properties of solutions in supercritical conditions.

CHAPTER 1

INTRODUCTION

Water is the fundamental molecule of life; it plays a vital role in climate change [6, 7], energy conversion [8, 9], and geological evolution [10]. The strong hydrogen bonding interaction and weak van der Waals forces lead to numerous unusual properties of liquid water [11], such as high surface tension, high boiling/melting point, decreased viscosity under pressure, and maximum density at 4°C. Furthermore, due to its polar nature, water possess the ability to dissolve and dissociate a wide range of solutes, and it is considered a universal solvent.

Solid/water interfaces represent an important topic in water research. Electrochemical devices, e.g. several batteries [12, 13, 14], photoelectrochemical cells [15, 16, 17], and biosensors [18, 19, 20] rely on the interactions between electrode materials and water-based electrolytes. In these systems, water not only acts as a solvent for ions but actively participates in chemical reactions at surfaces, enabling, for example, the charge transfer and generation of currents, leading to distinct structural and dynamical properties of interfacial water compared to its bulk form [21, 22]. The interplay between the structural and electronic properties of electrode materials and those of interfacial water significantly influences the performance of electrochemical devices, and gaining detailed insight into the properties of aqueous interfaces requires molecular-level investigations. This involves deriving atomistic structural models and conducting in-depth research on electronic states at solid/water interfaces. It also encompasses the study of adsoprtion properties of ions on electrode surfaces, the analysis of hydrogen bonding patterns of interfacial water, and the investigation of water dissociation at catalyst surfaces under applied electric fields.

Another active topic in water research relevant to Earth and planetary science is the study of the properties of the fluid at extreme conditions. High pressure and temperature (HPT) affect the structural properties and dissociation processes of water [23, 24], which are crucial in geochemical environments. However, experimental characterization of water

at extreme condition is challenging due to the corrosive properties of the liquid [25, 26]. As a result, the behavior and electronic properties of aqueous fluids under extreme conditions are not very well known and have been studied using a limited number of techniques, such as vibrational spectroscopy and, theoretically, classical molecular dynamics simulations.

The chemical complexity of solid/water interfaces and the challenges involved in probing HPT water call for the use of computational methods capable of addressing multiple properties of the fluid under multiple conditions. One powerful theoretical tool is density functional theory (DFT) [27, 28], which is based on the fundamental physical principles of quantum mechanics. The use of DFT coupled with molecular dynamics simulations, known as first-principles molecular dynamics (FPMD) [29], enables the description of both electronic interactions and dynamical properties of aqueous interfaces. This method has also been employed for the exploration of systems at high pressures and high temperatures, providing valuable insights into the structural behavior of HPT water [30, 31], and amorphous solids [32, 33].

In Chapter 2 of this thesis, we present the theoretical background of first-principles methods used to study aqueous interfaces and HPT water. Starting from the electronic problem, we introduce the nonrelativistic time-independent Schrödinger equation and the Born-Oppenheimer approximation. Next, we present the Hohenberg and Kohn theorems, which set the foundation of DFT. We discuss the Kohn-Sham equations [34, 27] for the calculation of the electronic ground state and the choice of the exchange-correlation functionals used in this thesis. Then we present the theory of FPMD simulations, which couples the electronic structure calculations with molecular Dynamics simulations, as well as finite field methods [35], which allow for the computation of the ground states energy of a solid or fluid in the presence of an electric field. In addition to the theoretical framework, Chapter 2 includes the description of computational methods used to interpret the experimental spectroscopic measurements for interfacial and/or bulk aqueous systems. We first discuss

the calculation of Raman spectra obtained from the system's polarzability and contributions from the effective polarizaility of molecules, and then we introduce a method to obtain the photoelectron (PE) spectra from absolute orbital energies.

Using the theoretical frameworks and computational methods of Chapter 2, we present our investigation of the electrochemical properties of semiconductor/water interface [36]. In Chapter 3, we focus on the the hydrogenated silicon (Si)/water interface, a system of interest in various electrochemical [37, 16, 38] and bioelectronic devices [1, 39]. As one of the most widely used semiconductor materials, Si-based devices are used in biosensors [40], photocathodes for water splitting cells [41] and transient electronics [1], and are in contact with a water-based electrolyte. In addition, in several instances the interfaces are under the effect of electric fields (e.g. an applied bias). The formation of an electrochemical interface leads to the generation of currents, i.e. capacitive and Faradaic currents. While understanding the behavior of the Si/water interfaces is beneficial for optimizing device performance, it is also a fundamental problem addressing complex aqueous environments, in particular the interplay between surface chemistry and solvation effects. Such effects are critical for interpreting challenging experiments on heterogeneous structures. In our work, we constructed an atomistic model of a Si/water interface by performing FPMD simulations in the presence of electric fields. We determined the electronic structure of the interface by computing flat-band potentials as a function of the electric field and calculating the tunnelling current images. Our work provides insight into the atomistic origin of currents generating at electrified aqueous interfaces. Our study reveals that capacitive currents depend linearly on the magnitude of the applied field, while Faradaic currents are weakly affected by the field and are related to the surface chemistry.

In Chapter 4, we focus on investigating the vibrational and dynamical properties of the Si/water interface. The properties of electrified aqueous interfaces critically depend on the structural arrangement of interfacial water molecules, in particular on the Hydrogen

bond (HB) structures. Vibrational spectroscopy is an ideal tool for exploring the bonding configurations of HBed systems. To comprehend the vibrational signatures of water at the electrode surfaces, the in-situ probing of the interfacial systems is essential. In recent years, the advancement of surface-enhanced Raman spectroscopy (SERS) [42] has allowed for the characterization of the HB networks of water at electrified solid/liquid interface. However, an atomistic interpretation is required to interpret measured Raman spectra. We combined computational method and an in-situ surface-enhanced Raman spectroscopy carried out by collaborators at the University of Illinois, Urbana, to study the vibrational properties of interfacial water at a H-terminated Si surface [43]. We analyzed the HB structures of water at the surfaces, and calculated the Raman spectra from time correlation functions of polarzaility tensors. To explore the experimental surface-enhanced Raman spectra at the molecular level, we calculated the effective polarizabilities, and thus obtained the Raman line shape for selected water molecules. The combined effect of surface and electric field on the interface was elucidated. The presence of the surface breaks the HB network of interfacial water molecules, leading to a blue-shift of O-H stretching mode in Raman spectra, relative to pure water. The negative electric field enhances the HB network between water molecules, but further weakens the HB between the H-Si surface and the topmost layer of water, yielding a merged O-H stretching peak in the Raman spectrum. The stable HB networks of interfacial water produced by a positive electric field leads instead to sharp peaks in the low frequencies region of Raman spectra.

In Chapter 5, we turn to studying the electronic properties of aqueous solutions and water under pressure and high temperature [44]. The deep-earth aqueous fluids play an essential role in transport process and may participate in chemical reactions when in contact with rocks in the Earth's interior [45]. Most of the current knowledge of HPT liquids comes from geophysical models and from limited vibrational spectroscopic measurements. The characterization of electronic properties of aqueous solutions and water at high pressure and

high temperature conditions is challenging. First-principles methods are a useful tool to predict the electronic properties of HPT aqueous systems and to interpret experiments. In our study, we calculated the photoelectron (PE) spectra of water and NaCl solutions, at conditions corresponding to those in the Earth's upper mantle (11GPa and 1000K); we used FPMD and DFT with dielectric-dependent hybrid (DDH) functionals [46, 47]. We computed the PE spectra of water and NaCl solution referenced to vacuum and observed a broadening of the HPT spectra relative to ambient conditions. We found that the ionization potentials of ions are underestimated by the semi-local functional PBE relative to DDH, and DDH results show a red shift with increasing P and T which is not reproduced by the PBE functional. To understand the electronic states involved in proton transfer events at HPT, we calculated the projected density of states of selected dissociating species. Our results illustrate the contributions of dissociated species in particular hydroxide, hydronium ions and H_4O_2 to the PE spectra.

The thesis is concluded in Chapter 6, with a discussion and perspective about future work.

CHAPTER 2

THEORETICAL BACKGROUNDS

2.1 Introduction

In this chapter, we present the theoretical methods employed in this thesis. We start from the nonrelativistic time-independent Schrödinger equation and introduce the Born-Oppenheimer approximation. We then provide an overview of density functional theory (DFT), beginning with the Hohenberg and Kohn theorems [34] that establish the connection between electron density and the external potential. The Kohn-Sham equations [27] are discussed, offering a practical approach for solving the electronic structure problem within DFT. We compare various approximations and exchange-correlation functionals used in DFT calculations, which are essential for approximating the unknown exchange-correlation energy functional.

Continuing our exploration, we introduce the concept of First-principles Molecular Dynamics (FPMD) [29], an approach combining electronic structure calculations with Molecular Dynamics simulations, and enabling the study of systems at finite temperatures. Then we introduce the finite-field method [35], which allows for FPMD simulations in finite electric fields. In the later section of this chapter, we shift our focus to the application of FPMD in computing the vibrational and electronic properties of both solid/liquid interfaces and pure water systems. Specifically, we discuss the computational Raman spectra and photoelectron spectra, leveraging the principles and techniques outlined earlier in the chapter.

2.2 The Electronic Problem

In quantum chemistry, solving the electronic problem involves calculating the eigenvalues and eigenvectors of the nonrelativistic time-independent Schrödinger equation.

$$H\Psi = \mathscr{E}\Psi \tag{2.1}$$

Where H is the Hamiltonian operator for a system of nuclei and electrons, Ψ is the wave functions, and $\mathscr{E}$ is the energy. Various numerical methods and approximations have been employed to solve the Equation 2.1. The Born-Oppenheimer approximation simplifies the electronic problem by separating the electronic and nuclear motions. Within this approximation, the kinetic energy of nuclei can be neglected and the repulsion between nuclei can be considered to be constant, and hence, the electronic Hamiltonian for a system with N electrons and M nuclei can be expressed as

$$H_{ele} = \sum_{i=1}^{N} \frac{1}{2} {\nabla_i}^2 - \sum_{i=1}^{N} \sum_{I}^{M} \frac{Z_I}{|\boldsymbol{r_i} - \boldsymbol{R_I}|} + \sum_{i=1}^{N} \sum_{j>i}^{N} \frac{1}{|\boldsymbol{r_i} - \boldsymbol{r_j}|} \tag{2.2}$$

In the above equation, the indices i and j represent electrons, while I denotes the nucleus. $\boldsymbol{r_i}$ and $\boldsymbol{R_I}$ are the position vectors for electron and nucleus, respectively. Z_I is the atomic number of nucleus I. The Laplacian operators ${\nabla_i}^2$ involve differentiation with respect to the coordinates of the i-th electron. The three terms in Equation 2.2 correspond to the kinetic energy of the electrons, the attraction between electrons and nuclei, and the repulsion between electrons. Solving the Schrödinger equation that includes the term H_{ele} yields the electronic wave function and electronic energy, which depend explicitly on the coordinates of electrons and parametrically on the coordinates of nuclei [48].

2.3 Density Functional Theory

2.3.1 The Hohenberg-Kohn Theorems

In the landmark paper published in 1964 [34], P. Hohenberg and W. Kohn proposed the foundation of density functional theory (DFT). The influential work proved what later became known as the Hohenberg-Kohn theorems (H-K theorems). The first theorem states that

The external potential acting on a system of interacting electrons is a unique

functional of the electron density.

This theorem can also be expressed as stating that the total energy of a system of interacting electrons in the presence of an external potential (e.g., that of the nuclei in a solid) is a unique functional of the electron density. We denoted the functional as $E[\rho(\boldsymbol{r})]$. The second theorem states that

For any trial density ρ_t, such that $\rho(t) \geq 0$ and $\int \rho_t(\boldsymbol{r})d\boldsymbol{r} = N$, then $E_{[}\rho_t] \geq E_0$.

This theorem states that the density that minimizes the total energy is the ground state density, and the minimum energy is the ground state energy.

The H-K theorems state that a universal energy functional $E_{HK}[\rho]$ exists. Such functional may be written as the sum of the kinetic energy $T[\rho]$ of the interacting electrons, the external potential $E_{ext}[\rho]$ (e.g., the interaction of electron with the nuclei), and electron-electron interaction $E_{ee}[\rho]$, which includes the Hartree energy:

$$E_{HK}[\rho] = T[\rho] + E_{ext}[\rho] + E_{ee}[\rho] = F_{HK}[\rho] + \int V_{ext}(\boldsymbol{r})\rho(\boldsymbol{r})d\boldsymbol{r} \tag{2.3}$$

The HK theorems do not provide any expression for the energy functional E, which remains unknown.

2.3.2 The Kohn-Sham Equations

In 1965, W. Kohn and L. J. Sham (KS) proposed an approach to evaluate the energy functional E_{HK} in equation 2.3 by considering an auxiliary system that can be solved in a simpler manner [27]. KS assumed that there exits a system of non interacting electrons (auxiliary system) that has the same change density at that of the system of interacting electrons. For a system of non interacting electrons, the charge density ρ can be written as the sum of the square moduli of single particle orbitals ψ, and the kinetic energy functional can be easily

obtained from the single particle wavefunctions. KS then included all of the many body effects of the interacting system (including those present in the kinetic energy of the interacting system) into an unknown functional, called exchange correlation functional $E_{XC}[\rho]$. The total energy functional is then expressed as

$$E_{KS}[\rho] = T_s[\rho] + E_{ext}[\rho] + E_H[\rho] + E_{XC}[\rho] \tag{2.4}$$

The external potential energy functional $E_{ext}[\rho]$ and Hatree energy functional $E_H[\rho]$ can be determined directly from their classical expressions,

$$E_{ext}[\rho] = \int V_{ext}(\boldsymbol{r})\rho(\boldsymbol{r})d\boldsymbol{r} = -\sum_{I}^{N_{nuclei}} \int \frac{Z_I}{|\boldsymbol{R_I} - \boldsymbol{r}|}\rho(\boldsymbol{r})d\boldsymbol{r} \tag{2.5}$$

and

$$E_H[\rho] = \frac{1}{2}\int\int \frac{\rho(\boldsymbol{r})\rho(\boldsymbol{r'})}{|\boldsymbol{r} - \boldsymbol{r'}|}d\boldsymbol{r}d\boldsymbol{r'} \tag{2.6}$$

The kinetic energy functional of non-interacting electron $T_s[\rho]$ is

$$T_s[\rho] = \sum_{i}^{N_{electron}} \left\langle \psi_i \middle| -\frac{1}{2}\nabla^2 \middle| \psi_i \right\rangle \tag{2.7}$$

The unknown term, the exchange-correlation energy functional $E_{XC}[\rho]$ includes all the electron-electron interactions. The minimization of $E_{KS}[\rho]$ with respect to the density, subject to the constraint of orthonormality condition of the single particle orbitals results in a set of partical differential equations to be solved self-consistently, the KS equations:

$$H_{KS}\psi_i(\boldsymbol{r}) = \varepsilon_i\psi_i(\boldsymbol{r}) \tag{2.8}$$

Where

$$H_{KS} = -\frac{1}{2}\nabla^2 + V_{ext} + V_H + V_{XC} \tag{2.9}$$

The external potential is:

$$V_{ext} = -\sum_{I}^{N_{nuclei}} \frac{Z_I}{|\boldsymbol{R_I} - \boldsymbol{r}|} \tag{2.10}$$

The Hartree potential is

$$V_H = \frac{1}{2}\int\int \frac{\rho(\boldsymbol{r'})}{|\boldsymbol{r} - \boldsymbol{r'}|} d\boldsymbol{r'} \tag{2.11}$$

The exchange-correlation potential is the derivative of exchange-correlation energy

$$V_{XC} = \frac{\delta E_{XC}}{\delta \rho(\boldsymbol{r})} \tag{2.12}$$

As mentioned above, the electron density is the sum of the square moduli of single particle orbitals, the KS orbital ψ_i,

$$\rho(\boldsymbol{r}) = \sum_{i}^{N_{electron}} |\psi_i|^2 \tag{2.13}$$

The ε_i are KS eigenvalues. Note that these eigenvalues are not the energies to add or subtract the electrons from the many-body system.

2.3.3 Approximations and Exchange-correlation Functionals

The accuracy of DFT calculations depends on the choice of the exchange-correlation energy functional. The exact from of exchange-correlation is not known and remains an active area of research. As a result, approximations are used to describe this term in practical calculations. The quality of the selection of exchange-correlation energy functional is typically assessed by comparing the computational properties with experimental data, or with results obtained via the calculation from quantum chemistry wave-function methods [49]. Some

early approximations include the local density approximations (LDA) [27] and semi-local generalized gradient approximation (GGA) methods [50].

LDA assumes that the density locally can be approximated as a uniform electron gas. The LDA functional has the form

$$E_{xc}^{LDA}[\rho] \approx \int \rho(\boldsymbol{r})\varepsilon_{xc}(\rho(\boldsymbol{r}))d\boldsymbol{r} \tag{2.14}$$

where $\rho(\boldsymbol{r})$ is the electron density at position $\boldsymbol{r}$, and ε_{xc} is the exchange-correlation energy per electron of a uniform electron gas of density $\rho(\boldsymbol{r})$.

LDA can provide reasonable accuracy for many systems; however, it does not capture important non-local effects and can lead to limitations in describing systems with strong electron correlation or weak dispersion forces. The GGA considers an inhomogeneous electron gas, with which the exchange and correlation energy depend not only on the electron density but the derivative of the density. The typical form for a GGA functional is

$$E_{xc}^{GGA}[\rho] \approx \int \rho(\boldsymbol{r})\varepsilon_{xc}(\rho,\ \nabla\rho)d\boldsymbol{r} \tag{2.15}$$

The use of GGA has improved the accuracy in calculating certain properties of materials when compared to LDA, such as atomization energies of molecules [50] and binding energies of rare-gas dimers [51]. The introduction of GGA functionals led to widespread acceptance of DFT in the 1990s in the chemistry community [52]. Among the various GGA functionals, the Perdew, Burke, and Ernzerhof (PBE) functional [50] has gained popularity due to its favorable performance-to-cost ratio for electronic structure calculations. PBE has been extensively applied to study a wide range of systems, including solid-state materials, and in the context of this thesis, the PBE functional serves as the primary functional used for the investigations.

The PBE functional may not always provide sufficient accuracy in representing the elec-

tronic properties of certain systems. To overcome this limitation, an improvement can be achieved by incorporating exact Hartree-Fock exchange, leading to hybrid functionals. One example is PBE0[53].

$$E_{xc}^{PBE0} = \alpha E_x^{HF} + (1-\alpha)E_x^{PBE} + E_c^{PBE} \tag{2.16}$$

The inclusion of exact exchange helps to better capture non-local effects, and in some cases, may improve the treatment of systems with strong electron correlation or weak dispersion forces. The mixing coefficient for the exchange α is argued to be 0.25 for the PBE0 functional from perturbation arguments. For dielectric-dependent hybrid functional (DDH) [46, 47], this parameter is determined from the dielectric constant of the system.

Some calculations present in this thesis also employed a vdW density functional. A proper description of vdW interaction is an important prerequisite to gain insight into the interfacial effects. Many schemes have been developed to enable the dispersion interaction to be accounted for within DFT, one of the most promising methods being the non-local van der Waals density functional (vdW-DF) [54]. The exchange correlation functional for vdW-DF has the form

$$E_{xc} = E_x^{GGA} + E_c^{LDA} + E_c^{nl} \tag{2.17}$$

where E_x^{GGA} and E_c^{LDA} are the exchange energy defined for GGA functionals and correlation energy obtained with LDA, respectively, and E_c^{nl} is the non-local correlation energy, which is based on electron densities interacting via a model response function.

It has been observed that the performance of non-local vdW-DF methods is highly dependent on the choice of the exchange functional. In the original vdW-DF, E_x^{GGA} was derived from a revised version of the PBE functional (known as revPBE). However, an optimized exchange functional called B88 (referred to as 'optB88') was introduced as a replacement

for the revPBE-based functional [55]. This modification resulted in a new functional that exhibits improved performance, particularly when evaluated against the S22 dataset [56], which consists of 22 weakly interacting dimers, primarily of biological significance.

2.3.4 Planewave Pseudopotential Method

The DFT calculations performed in this thesis use a planewave basis set and periodic boundary conditions. The eigenfunctions $\psi_{n,\boldsymbol{k}}$ of a single-particle Schrödinger equation with a periodic potential can be written as a periodic function $u_{n,\boldsymbol{k}}$ modulated by a plane wave with wave vector $\boldsymbol{k}$

$$\psi_{n,\boldsymbol{k}}(\boldsymbol{r}) = u_{n,\boldsymbol{k}} e^{i\boldsymbol{k}\cdot\boldsymbol{r}} \tag{2.18}$$

Since $u_{n,\boldsymbol{k}}$ is periodic, the wave function may be expressed as a linear combination of plane waves

$$\psi_{n,\boldsymbol{k}}(\boldsymbol{r}) = \sum_{\boldsymbol{G}} c_{n,\boldsymbol{k}}(\boldsymbol{G}) e^{i(\boldsymbol{k}+\boldsymbol{G})\cdot\boldsymbol{r}} \tag{2.19}$$

where $\boldsymbol{G}$ is the reciprocal lattice vector. The larger the number of G vectors, the more accurate the results but the longer the computational time. Hence, the wave functions are truncated by keeping the plane wave vectors $\boldsymbol{k}+\boldsymbol{G}$ with a kinetic energy lower than the cutoff value E_{cut}

$$\frac{\hbar^2}{2m}|\boldsymbol{k}+\boldsymbol{G}|^2 \leq E_{cut} \tag{2.20}$$

One advantage of using planewave basis sets in DFT is the speedup provided by the FFT algorithm [57] for various calculations. For FPMD simulation, the use of planewave basis sets allows for a convenient way of calculating the ionic forces without basis set superposition effects [58] in comparison with Gaussian basis sets. However, planewave basis sets suffer from slow convergence due to the sharp nodes of core electron wave functions, and therefore,

all-electron calculations require a large number of planewaves. To address this challenge, pseudopotentials are employed to effectively represent the nucleus and core electrons with valence electrons while reducing computational costs. The pseudopotential approximation assumes that valence electrons are sensitive to the chemical bonding environment, while core electrons are chemically inert. The work presented in this thesis utilizes optimized norm-conserving Vanderbilt (ONCV) pseudopotentials [59]. The construction process involves fitting the pseudo wavefunctions to the all-electron valence electron wave functions such that the integral of the squared magnitude of the pseudopotential wave functions is equal to that of the all-electron wave functions.

2.4 Many-Body Perturbation Theory

Although the DFT provides a computationally efficient way to calculate the ground-state electronic properties of condensed-phase systems, accurate description of band structures requires advanced electronic structure theories including the calculations of electronic excited states. In Chapter 3 of this thesis, we employed many-body perturbation theory (MBPT) with the GW approximation to obtain better agreement with experimental measured band gaps of Si and water slabs.

The GW approximation is a specific implementation of MBPT that focuses on improving the description of charged electronic excitations. In 1965, Hedin published the GW method [60]; however, owning to the computational complexity, the first application of the GW method to the solid-state materials was reported 20 years later [61]. The GW method overcomes some of the deficiencies of DFT calculations and is based on the representation of single particle Green's functions, G, whose pole describes single particle excitation energies. The GW method replaces the unknown exchange-correlation term in the DFT calculation by a non-local energy and dependent self-energy Σ, and thus, the KS equation is replaced into a self-consistent set of quasiparticle (QP) equations. The QP states ψ_n^{qp} and QP energies

E_n^{qp} can be obtained from

$$[T + V_{ext}(\boldsymbol{r}) + V_H(\boldsymbol{r})]\psi_n^{QP}(\boldsymbol{r}) + \int d\boldsymbol{r'}\Sigma(\boldsymbol{r}, \boldsymbol{r'}; E_n^{QP})\psi_n^{QP}(\boldsymbol{r'}) = E_n^{QP}\psi_n^{QP}(\boldsymbol{r}) \tag{2.21}$$

where T is the kinetic energy, V_{ext} is the external potential, and V_H is Hartree potential. Within the GW approximation, Σ can be expressed as

$$\Sigma(\boldsymbol{r}, \boldsymbol{r'}, \boldsymbol{\omega}) = i \int \frac{d\omega'}{2\pi} G(\boldsymbol{r}, \boldsymbol{r'}; \omega + \omega')W(\boldsymbol{r}, \boldsymbol{r'}; \omega') \tag{2.22}$$

The G_0W_0 approximation is the simplest version of the GW method. It involves calculating the self-energy without any self-consistent procedure. The G_0W_0 method provides a reasonable balance between accuracy and computational cost, and the QP energies are computed as first-order correction to the KS energies:

$$E_n^{QP} = \epsilon_n + \langle\psi_n|\Sigma_{G_0W_0}(E_n^{QP}) - V_{xc}|\psi_n\rangle \tag{2.23}$$

where ϵ_n is the KS energies and V_{xc} is the exchange-correlation potential from the KS equation.

The demonstrated effectiveness has rendered the GW method a valuable tool for exploring the electronic properties of various materials with diverse applications [62, 63]. For example, previous studies using the GW approximation have included the band structures of semiconductors with defects [64], the band alignment at metal-molecule interfaces [65], and the ionization potentials of organic semiconductors [66]. Additionally, the knowledge of the full spectrum of QP states facilitates the computation optical excitation spectra [63, 67].

2.5 First-Principles Simulations in Finite Temperatures

Classical Molecular dynamics (MD) simulations are valuable tools for studying the structural and thermodynamic properties of materials at finite temperatures. Classical MD generates molecular trajectories based on the classical statistical mechanics with the use of a force field to describe the interactions between atoms and molecules [68]. However, classical MD does not consider the quantum mechanical effects, such as electron-electron and electron-nucleus interactions and therefore lacks the ability to accurately describe properties like bonding in molecular systems, electronic structures, and chemical reactions. To investigate the structural and vibrational behaviors of complex aqueous systems, MD has been coupled with DFT, resulting in First-Principles Molecular Dynamics (FPMD) [29].

2.5.1 First-Principles Molecular Dynamics

In FPMD, for N atoms with coordinates $R_I(t)$ at time t, based on the Hellmann-Feynman theorem [69], the ionic forces F_I are obtained from the gradient of the ground state energy, which is calculated by solving the KS equations within DFT. The appropriate exchange-correlation functionals are employed to describe the electronic interactions in the system.

$$F_I = -\nabla_I E\left(\left\{R_I\left(t\right)\right\}\right) \tag{2.24}$$

Since the time evolution of electrons is much more rapid than that of the nuclei due to the difference in mass, in Born-Oppenheimer molecular dynamics, the motion of electrons and nuclei are treated separately to obtain the trajectory of molecular configurations, where the ground state wave function is first computed by solving KS equation (electronic step), then the coordinates of ions in the system are updated (ionic step) based on

$$M_I \ddot{R}_I = F_I \tag{2.25}$$

where M_I is the mass of the atom associated with the the I-th coordinate.

FPMD simulations offer an accurate description of various structural and dynamical properties of aqueous systems at finite temperatures. The atomistic structures constructed through FPMD simulations enable theoretical predictions of various experiments. For water and aqueous solutions, FPMD-generated trajectories allow for the computation of time-dependent properties, such as Raman [43, 70] and infrared (IR) spectra [71, 72]. In addition to reproducing measurable experimental quantities, FPMD simulations play a crucial role in predicting materials' properties and are vital for materials design [73]. FPMD has become a major tool to investigate the impact of synthetic tunable parameters on performance of electrochemical devices, such as photoelectrochemical cells (PECs) [74, 75, 76], batteries [77, 78], and bioelectronics [36].

It is worth noting that the GGA exchange-correlation functionals, such as the commonly used PBE functional, do not adequately capture nondirectional van der Waals (vdW) interactions, resulting in overstructured properties when simulating liquid water at room temperature [79, 80]. To retain the realistic properties of liquid water at room temperature, PBE simulations are usually conducted at an elevated temperature of 400K [81, 82].

2.5.2 Neural Network Potential

The computational cost of FPMD simulations in evaluating the energy and forces of molecules restrict its application to systems contain thousands of atoms.

In recent years, the use of machine learning (ML) potentials has allowed for large-system calculations with first-principle accuracy; ML potentials include neural network potential (NNP) [83], Gaussian approximation potential (GAP) [84], the moment tensor potentials (MTP) [85] and the spectral neighbor analysis potential (SNAP)[86]. In Chapter 5, we use DeePMD [87] to simulate a HPT water slab in a vacuum.

Behler and Parrinello proposed the first neural network potential [83]. The fundamental

concept, grounded in the locality assumption, posits that the overall energy of a system results from the accumulation of individual atomic energy contributions.

$$E = \sum_i E_i \tag{2.26}$$

where E_i is the atomic energy of i-th atom with neighbors within a pre-defined cutoff radius R_c.

$$E_i = E_{s(i)}(\boldsymbol{R_i}, \boldsymbol{R_j}) \tag{2.27}$$

$\boldsymbol{R_i}$ is atomic position of atom i, $\boldsymbol{R_j}$ is neighbor atoms within the R_c, and $|R_i - R_j| \leq R_c$. s(i) is the chemical species of atom i. In NNPs, where descriptors are often used to represent the atomic coordinates, it is a numerical representation that summarizes the characteristics of input data. In the DeePMD potential, the descriptor is constructed by shifting the position of neighbors by the position of atom i, i.e. $\boldsymbol{R_{ij}} = \boldsymbol{R_i} - \boldsymbol{R_j}$, and then introducing a local frame and recording the local coordinate for each atom. Finally, the descriptive information of atoms in the cutoff is segregated into full and radial-only information. The NNPs map the descriptors to atomic energy. The NNs are fully connected layers of linear transformations, and these contain the input descriptor vectors $\boldsymbol{x}$, weights $\boldsymbol{W}$, biases $\boldsymbol{b}$, nonlinear activation function φ, hidden layer $\boldsymbol{h}$ and output vectors $\boldsymbol{y}$[88]. To construct a deep NN with L hidden layers

$$\boldsymbol{h_1} = \boldsymbol{\sigma}(\boldsymbol{W_1 x} + \boldsymbol{b_1}) \tag{2.28}$$

$$\boldsymbol{h_2} = \boldsymbol{\sigma}(\boldsymbol{W_2 h_1} + \boldsymbol{b_2}) \tag{2.29}$$

$$\vdots \tag{2.30}$$

$$\boldsymbol{h_L} = \boldsymbol{\sigma}(\boldsymbol{W_L h_{L-1}} + \boldsymbol{b_L}) \tag{2.31}$$

$$\boldsymbol{y} = \boldsymbol{W_{L+1} h_L} + \boldsymbol{b_{L+1}} \tag{2.32}$$

The parameters $\boldsymbol{W}$ and $\boldsymbol{b}$ are initialized randomly and optimized to minimize the loss function that measures the discrepancy between the predicted output and reference data. In DeepMD the loss function is defined as the mean square error (MSE).

$$L(p_\epsilon, p_f, p_\xi) = \frac{p_\epsilon}{N}\Delta E^2 + \frac{p_f}{3N}\sum_i |\Delta \boldsymbol{F_i}|^2 + \frac{p_\xi}{9N}||\Delta \Xi||^2 \tag{2.33}$$

The p_ϵ, p_f, p_ξ are prefactors that relate to the learning rate and can be adjusted during the training process. ΔE, $\Delta \boldsymbol{F_i}$, $\Delta \Xi$ are root mean square error of energy, force, and virial.

The development of NNP has unlocked possibilities of exploring large and complex systems, and enabled significant progress that was previously impeded by the computational costs associated with conventional electronic-structure methods. In addition to the advantages in investigating the structural properties of large-scale systems [89, 90, 11, 91], NNPs have proven to be an essential tool to study electrochemical systems [92], including the proton transfer on TiO_2 surfaces [93], the Hydrogen evolution reactions on Pt [94], and ion transport in Li-ion batteries [95].

2.6 First-Principles Simulations in Finite Electric Fields

First-principles simulations may be performed in the presence of a finite electric field through two methods: linear response and the finite field methods. The linear response method based on density functional perpurbation theory (DFPT) [96] treats the electric field as a perturbation and computes response properties[97]. For the finite field method, the electric field is introduced by carrying out the calculation of the electronic ground state using the electric enthalpy as defined by Souza et al. [35]. This latter method has been implemented in the massively parallel, open source Qbox code [98], hence in this thesis, we mainly use the finite field approach to simulate an electrified interfacial model from first-principles.

To calculate the ground state of an insulating system under a finite electric field, we solve

for the field-polarized Bloch functions by minimizing the electric enthalpy functional [99],

$$\mathcal{F}[u_{n\boldsymbol{k}};\boldsymbol{E}] = E_{KS} - \Omega \boldsymbol{P}_{mac} \cdot \boldsymbol{E} \tag{2.34}$$

where $u_{n\boldsymbol{k}}$ is the periodic part of the field-polarized Bloch function $\psi_{n\boldsymbol{k}}(\boldsymbol{r})$,

$$\psi_{n\boldsymbol{k}}(\boldsymbol{r}) = e^{i\boldsymbol{k}\cdot\boldsymbol{r}} u_{n\boldsymbol{k}}(\boldsymbol{r}) \tag{2.35}$$

and $\boldsymbol{E}$ is the macroscopic field, Ω is the unit cell volume, and E_{KS} is Kohn–Sham energy. The macroscopic polarization $\boldsymbol{P}_{mac}$ was obtained using the Berry-phase approach [100, 101]

$$\boldsymbol{P_{mac}} = \frac{-2e}{(2\pi)^3} \sum_n \int_{BZ} d\boldsymbol{k} \langle u_{n\boldsymbol{k}} | i\nabla_{\boldsymbol{k}} | u_{n\boldsymbol{k}} \rangle \tag{2.36}$$

It should be noted that the electric enthalpy will lose its minima when the **E** gets too big [35], which occurs for

$$e|\mathbf{E} \cdot \boldsymbol{a_i}| \simeq \frac{E_{gap}}{N_i} \tag{2.37}$$

where E_{gap} is the energy gap of the system, $\boldsymbol{a_i}$ is the lattice vector along the direction of the applied electric field, and N_i is the the number of k-points along the reciprocal lattice vector i, in the $N_1 \times N_2 \times N_3$ k-mesh.

First-principles simulations of the polarizability and dielectric properties of materials require electric field response calculations [102]. The development and implementation of finite electric field methods have enabled the evaluation of these quantities, allowing for the theoretical modeling of Raman and sum-frequency generation (SFG) spectra of water and aqueous interfaces [43, 103, 45]. Moreover, the construction of electrified structures brings us closer to modeling experimental setups, including batteries, photoelectrochemical cells, and bioelectronics [104]. In such devices, the electrode/electrolyte interface is subjected to an external electric field or undergoes an electrochemical charge transfer process. FPMD

simulations coupled with the finite field approach have been utilized to study the structural behavior of NaCl and methanol solutions under an electric field [105, 106], as well as phenomena occurring at electrode surfaces, such as water dissociation [107] and electrochemical currents [36].

Despite recent advancements in describing liquid and aqueous interfaces in the presence of electric fields, simulating electrified electrochemical systems still presents challenges, particularly in terms of computational cost due to the size of the simulation cell and the required time scale [8]. The finite field approach may suffer from slow convergence as a function of the supercell size [97]. However, to understand the microscopic properties of aqueous interfaces for electrochemical applications, the construction of realistic atomistic models of systems containing thousands of electrons is necessary. This challenge may be addressed in the future by integrating new algorithms with high-perforamnce computing capabilities.

2.7 Computational Raman Spectroscopy

As discussed in Section 2.5, the accurate calculation of Raman spectra of water and aqueous interface involves the evaluation of polarization tensors as the function of time, which requires first-principles simulations in the presence of external electric fields. The polarizability tensor can be accessed using density functional perturbation theory (DFPT) [43] or by carrying out simulations in a finite electric field, and obtaining the polarization from the maximally localized Wannier functions [108]. The Raman spectra are then obtained from the correlation function (TCF) of polarizability tensors computed for snapshots extracted from FPMD trajectories.

The polarizability tensor $\boldsymbol{\alpha}$ can be decomposed into an isotropic part

$$\bar{\alpha} = \frac{1}{3} Tr\boldsymbol{\alpha} \tag{2.38}$$

and an anisotropic part

$$\boldsymbol{\beta} = \boldsymbol{\alpha} - \mathbf{1}\bar{\alpha}, \tag{2.39}$$

These two terms correspond to the isotropic R_{iso} and anisotropic component R_{aniso} of Raman spectra, respectively:

$$R_{iso}(\omega) \propto \frac{\hbar\omega}{k_b T} \int dt e^{-i\omega t} \langle \bar{\alpha}(0)\bar{\alpha}(t) \rangle \tag{2.40}$$

$$R_{aniso}(\omega) \propto \frac{2}{15} \frac{\hbar\omega}{k_b T} \int dt e^{-i\omega t} \langle Tr\beta(0)\beta(t) \rangle \tag{2.41}$$

where ω is the frequency shift of Raman spectra. Equations 2.40 and 2.41 originate from the differential cross section of Raman scattering and relate to the polarization directions of the incident and scattered light. In practice, experimental measurements of Raman scattering are the linear combinations of isotropic and anisotropic Raman component.

2.7.1 Maximally Localized Wannier Functions

Obtaining the molecular contributions of Raman spectra requires the calculation of Maximally localized Wannier functions (MLWFs) [108]. Wannier functions are a set of orthogonal functions obtained from unitary transformation of Bloch orbitals that provide a localized description of the electronic structure. MLWFs are a subset of Wannier functions that are optimized to be as localized as possible in real space. The goal of MLWFs is to minimize the spread of the electronic wave function while still preserving the important features of the underlying electronic structure. Wannier centers are a measure of the spatial localization of electrons within a crystal. They provide information about the average position of the electronic charge density associated with a particular Wannier function. The Wannier center of the nth MLWF w_n is defined as

$$r^0_{n,i} = \frac{L_i}{2\pi} Im ln \langle w_n | e^{i\frac{2\pi}{L_i} r_i} | w_n \rangle \tag{2.42}$$

where L_i denotes i-th cell dimension, w_n is obtained by applying a unitary transformation to the occupied KS eigenstates.

2.7.2 Effective Polarizability

To identify molecular contributions to the total Raman line shapes, we can calculate the effective polarizability [43] of individual molecules in the system, as obtained from the derivative of the molecular dipole moment with respect to the electric filed. The dipole moment can be obtained using MLWFs, as a function of simulation time $\boldsymbol{\mu}(t)$:

$$\boldsymbol{\mu}(t) = 6e \sum_i \boldsymbol{r_i^O}(t) + e \sum_j \boldsymbol{r_j^H}(t) - 2e \sum_k \boldsymbol{r_k^{MLWF}}(t) \tag{2.43}$$

where $\boldsymbol{r_i^O}(t)$ and $\boldsymbol{r_j^H}(t)$ are the coordinates of the Oxygen and Hydrogen atoms. The third term $\boldsymbol{r_k^{MLWF}}(t)$ is the coordinate of MLWFs centers belonging to a water molecule. Within the Born-Oppenheimer approximation, the polarzaibility tensor $\boldsymbol{\alpha}$ at time t can be obtained from the response of the dipole moment under a small electric field $\boldsymbol{E}$.

$$\boldsymbol{\alpha}(t) = \frac{\delta \boldsymbol{\mu}(t)}{\delta \boldsymbol{E}} \tag{2.44}$$

In this thesis, the effective polarizability tensor, denoted as $\boldsymbol{\alpha}_{ij}$ for a molecule i, is obtained by applying a small electric field along each of the Cartesian axes. To compute the molecular dipole moment $\boldsymbol{\mu}_i$ for an individual molecule in the system, we rely on its atomic coordinates and the centers of MLWFs. By employing the centered finite difference expression in six different directions, we can determine the change in dipole moment resulting from a small perturbation of an electric field.

$$\boldsymbol{\alpha}_{ij}^{\text{eff}} = \frac{\boldsymbol{\mu}_i(+\delta E_j) - \boldsymbol{\mu}_i(-\delta E_j)}{2\delta \boldsymbol{E}_j} \tag{2.45}$$

Note that the effective polarizability is obtained by projecting the total polarizability tensor onto each individual molecule described by MLWFs. In the case of a water molecule, there are four MLWFs, which correspond to two covalent bond pairs (BP) and two lone pairs (LP).

$$\boldsymbol{\alpha}_{i}^{\text{eff}} = \boldsymbol{\alpha}_{i,BP1}^{\text{eff}} + \boldsymbol{\alpha}_{i,BP2}^{\text{eff}} + \boldsymbol{\alpha}_{i,LP1}^{\text{eff}} + \boldsymbol{\alpha}_{i,LP2}^{\text{eff}} \tag{2.46}$$

The effective polarizability also differs from the molecular polarizability; the latter only depends on the electronic structure of the molecule, and hence, it does not account for dipole-induced dipole contributions arising from the environment.

When summing the effective polarzailbity tensor over all i species in the system, we obtain the total polarizabilty of the system.

$$\boldsymbol{\alpha}(t) = \sum_i \boldsymbol{\alpha}_i^{\text{eff}}(t) \tag{2.47}$$

We decomposed the Raman spectra into interfacial contributions by selecting surface water molecules and calculating their corresponding effective polarizability tensors. The Raman line shapes of interfacial water molecules could then be obtained from the TCF of effective polarizability tensors.

$$R_{iso}\left(\omega\right) \propto \frac{\hbar\omega}{k_b T} \int dt e^{-i\omega t} \langle \sum_{i,j} \bar{\alpha}_i^{\text{eff}}(0) \bar{\alpha}_j^{\text{eff}}(t) \rangle \tag{2.48}$$

$$R_{aniso}\left(\omega\right) \propto \frac{2}{15} \frac{\hbar\omega}{k_b T} \int dt e^{-i\omega t} \langle Tr \sum_{i,j} \beta_i{}^{\text{eff}}(0) \beta_j{}^{\text{eff}}(t) \rangle \tag{2.49}$$

Based on these theoretical foundations, Putrino et al. conducted one of the earliest

FPMD studies on Raman scattering utilizing DFPT to investigate H-bond structures of ice under varying high pressures [109, 110]. Quan et al. later carried out the first Raman spectra study of liquid water using DFPT with 64 heavy water molecules at 400K [43]. The analysis involved calculating the effective polarizabilities, which enables the decomposition of Raman spectra into individual molecules. The differences in intramolecular and intermolecular contributions were also discussed.

Since then, the computational Raman spectroscopy has predominantly focused on bulk systems like high-pressure Hydrogen [111], Methyloxirane [70], and $ZnCl_2$ melt [112]. Recent advancements include the use of deep neural network-based potentials to reproduce Raman spectra [4]. These neural network models accurately predict vibrational properties of water and heavy water with FPMD-level accuracy, bypassing the need for expensive simulations [113].

The invention of nanoparticle-enhanced Raman spectroscopy in 2010 [114] opened up new possibilities for experimental investigations of electrochemical interfaces. However, to gain a deeper understanding of the interfacial structures and their vibrational behavior under the influence of an electric field, it is essential to complement experimental findings with computational studies of Raman spectra using the finite-field method and FPMD. This approach not only provides an interpretation to the experimental spectra but also allows for the exploration of individual interfacial molecules' contributions to the spectral features. In Chapter 4 of this thesis, a comprehensive and detailed discussion of this topic will be presented, shedding light on the Raman spectroscopy of interfacial systems.

2.8 Computational Photoelectron Spectra

2.8.1 Absolute Orbital Energies

Photoelectron (PE) spectra can be obtained from the electronic density of states (DOS) using DFT. However, though the eigenvalue differences obtained from DFT are well defined, the eigenvalues obtained with the plane-wave pseudopotential method for periodic systems are not well defined [5, 115]. Hence, the computed energy states cannot be directly compared with experimental measured values. In order to obtain absolute energies $\tilde{\varepsilon}_i$, we reference the electronic energies with the energy level corresponding to vacuum,

$$\tilde{\varepsilon}_i = \varepsilon_i - \Delta V - V_{\text{bulk}} \tag{2.50}$$

where ε_i denotes Kohn-Sham eigenvalues computed for a bulk system in periodic plane-wave calculations. The term V_{bulk} is the averaged electrostatic potential $V(\boldsymbol{r})$ for bulk water samples.

2.8.2 The Electrostatic Potential

The electrostatic potential is defined as the sum of Hartree potential $V_H(\boldsymbol{r})$ due to the valence electron density, and a local part of the pseudopotential $V_{loc}(\boldsymbol{r})$, which includes the potential due to the nuclei and the core electrons, written as sum of spherical functions $V_{loc}^{(i)}$ centered at nucleus at $\boldsymbol{r_i}$ [116]

$$V(\boldsymbol{r}) = V_H(\boldsymbol{r}) + V_{loc}(\boldsymbol{r}) \tag{2.51}$$

where

$$V_H(\boldsymbol{r}) = \int \frac{n(\boldsymbol{r'})}{|\boldsymbol{r} - \boldsymbol{r'}|} d\boldsymbol{r'} \tag{2.52}$$

$$V_{loc}(\boldsymbol{r}) = \sum_i V_{loc}^{(i)}(|\boldsymbol{r} - \boldsymbol{r_i}|) \tag{2.53}$$

The term ΔV represents the electrostatic potential difference between the regions corresponding to the vacuum and bulk liquid.

$$\Delta V = \bar{V}_{\text{vacuum}} - \bar{V}_{\text{liquid}} \tag{2.54}$$

To determine this value, an interfacial model needs to be constructed. The potential difference for a specific structure can be calculated by taking the plane-average of $V(\boldsymbol{r})$ along the direction perpendicular to the interface[117]. In Cartesian coordinates, if the direction of interest is along the z-axis, the potential difference can be expressed as

$$\bar{V}(z) = \frac{1}{A}\langle \int\int V(x, y, z)dxdy \rangle \tag{2.55}$$

Here, A represents the cross-sectional area of the interface. The integral is taken over the region spanning the interface.

In the calculations of PE spectra for water or aqueous solutions, the term ΔV can be obtained by carrying out MD simulations of the liquid in contact with a vacuum and then carrying out electronic structure calculations on the trajectories generated for the liquid/vacuum slab.

CHAPTER 3

ELECTRONIC PROPERTIES OF ELECTRIFIED SEMICONDUCTOR AND WATER INTERFACES

This chapter is reproduced with permission from Ye, Z., Prominski, A., Tian, B., and Galli, G. (2021). Probing the electronic properties of the electrified silicon/water interface by combining simulations and experiments. Proceedings of the National Academy of Sciences, 118(46), e2114929118.

3.1 Introduction

Silicon-based materials have been used in a myriad of applications, including field-effect-transistor(FET)-based biosensing [118, 119], photoelectrochemical cells for water splitting [41, 37], transient electronics for minimally invasive implants [120], and photodiode-enhanced neuromodulation [1, 121, 122] (Figure 3.1). In all these devices, the Si surfaces are in contact with water, and the interfaces are either under the effect of an electric field (e.g., in the case of an FET biosensor or a photodiode-enhanced neuromodulator), or undergoing an electrochemical process (e.g., in the case of transient electronics or a water-splitting cell). These Si/water electrified interfaces can produce capacitive and/or Faradaic currents, which in turn can impact the signal transduction mechanism and efficacy of Si-based electrochemical or photoelectrochemical devices. Additionally, unintended electrochemical or photoelectrochemical current leakage at the Si/water interface may raise the noise level of the electronic or optoelectronic devices that are operated in an aqueous environment.

While the understanding and control of electrified semiconductor/water interfaces are important for both fundamental studies and technological applications, experimental approaches that can directly probe the interfacial dynamics and electrochemical reactivity at the atomistic level are still limited [123], especially in transient regimes. The aqueous envi-

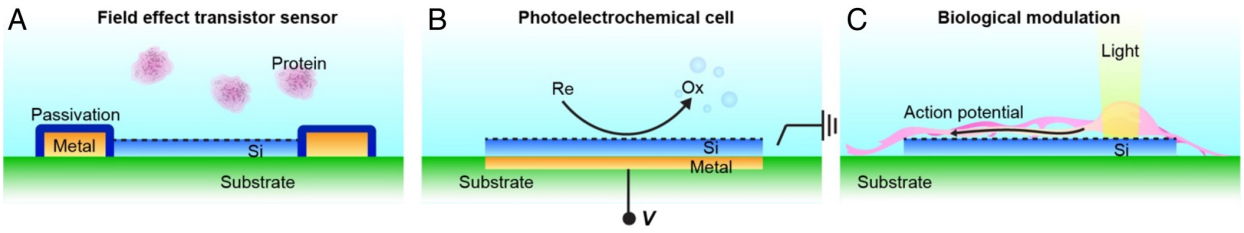

Figure 3.1: Electrified Si/water interfaces in silicon-based electronic, electrochemical, and photoelectrochemical devices. The dashed lines denote the Si/water interfaces. (A) Si nanowire FET sensor for proteins. The electrified Si/water interface may yield current leakage or corrosion, raising the noise level or causing device failure. (B) Si homojunction or heterojunction photoelectrochemical cells. Technically important applications such as water splitting can be assisted by this process. (C) Si homojunction- or heterojunction-based biological modulation tool. In one important case, light can produce photoelectrochemical effect at the Si surface for neuromodulation[1].

ronment present in biological and electrochemical systems is often rather complex; it includes multiple surface absorbates leading to different charge-transfer mechanisms, and the interplay between the surface chemistry and solvation effects usually hampers a spectroscopic investigation of the electrified electrode/liquid interface at the atomistic level. Computer simulations, on the other hand, can provide valuable information on the structural and electronic properties of aqueous interfaces [73, 22, 124, 125, 126] at the atomistic level, especially when first-principles methods [29] are used to describe interatomic forces and bond breaking and formation. When integrated with experiments [127], these simulations may help us understand specific Faradaic and non-Faradaic processes occurring at interfaces that in turn underpin the functions of bioelectronic and electrochemical devices. In Faradaic processes, currents cross the interface by virtue of an electrochemical reaction, while there is no transfer of ions or electrons across the electrode in non-Faradaic (or capacitive) processes. In the latter case, an equilibrium charge–voltage (σ-V) curve can be constructed, while in Faradaic processes one can construct a steady-state current–voltage (i-V) curve [128].

Here we focus on processes relevant to transient electronics and photoelectrochemical modulation of biological cells and tissues, where hydrogenated Si surfaces are initially in contact with water. Si-based transient electronics are largely based on the dissolution of Si

in water [129], where the Si–H bond attack by water molecules is typically expected to occur. In photoelectrochemical modulation, freshly etched Si nanowires or multilayered membranes are usually prepared and the surface of Si is hydrogen-terminated [1]. To investigate these aqueous interfaces, we generated an atomistic model of the electrified interface between the hydrogenated Si(100) surface and water by performing first-principles molecular dynamics (FPMD) [29] simulations in the presence of an electric field [130, 35]. We determined the electronic structure of the interface as a function of the applied bias, including band offsets, flat-band potentials, and interfacial scanning tunneling microscope (STM) images. We then investigated the origin of capacitive and Faradaic processes by directly comparing simulation and experimental results obtained for Si wafers etched in hydrofluoric acid (HF) so as to yield a hydrogen-terminated surface. Our work provides a strategy and a protocol to study electrified interfaces for biological and transient electronic applications, and it gives insight into the atomistic origin of capacitive and Faradaic currents. Interestingly, our simulations, validated by pulsed chronoamperometry measurements, show that capacitive currents depend almost linearly on the magnitude of the applied field, while Faradaic currents are weakly affected by the presence and magnitude of the applied electric field or by doping of the sample.

3.2 Methods

3.2.1 Computer Simulations and Electronic Structure Calculations

In our simulations we constructed a hydrogenated Si slab to model the electronic properties of Si in contact with water before the formation of the oxidation layer. In order to validate the results of the simulations, in our experiments we etched the Si surfaces with HF to remove any oxidized layers. This treatment yields Si surfaces mostly covered with H atoms, with a small amount of Si dangling bonds due to the corrosion of HF.

In particular, we modeled an H-Si/water interface with a supercell consisting of 124 water

molecules interfaced with a eight-layer hydrogenated Si(100) slab with 128 Si atoms, and we terminated the surface with hydrogen atoms. We also introduced a dangling bond on the surface, before equilibration, to mimic the presence of defects that are expected to be present in freshly prepared experimental samples. The interfacial thickness between Si and water was determined using the results of a previous study [22].

We first carried out first-principles Molecular Dynamics (FPMD) simulations using the erdew-Burke-Ernzerho (PBE) exchange-correlation functional [50], norm-conserving pseudopotentials [59], and a plane wave basis set and kinetic energy cutoff of 60 Ry. The Γ point was used to sample the Brillouin zone of the supercell. We generated trajectories in the NVT ensemble using the Qbox code [98] at a target temperature of 400K with the Bussi, Donadio, and Parrinello (BDP) thermostat [131]. The target temperature was chosen to be higher than room temperature to model structural properties of water in better agreement with experiments, when using the PBE functional [132]. The whole slab was equilibrated at 400 K, including the Si part.

To understand the effect of van der Waals interactions on the description of the properties of liquid water, bulk Si, and the interface we also conducted additional FPMD simulations with the van der Waals density functional optB88 [55] at a target temperature of 330 K. We calculated the lattice parameter of bulk Si related with optB88 and PBE, and compared with the experimental value, as shown in Table 3.1. The lattice constants of bulk Si obtained with PBE and opbB88 calculated in the present work are similar to reported computational values, as well as to the experimental measurement.

We also compared the structural properties of water obtained with optB88 and PBE functionals in the absence of bias. We present a detailed comparison between the results obtained with the two functionals. Sepecifically, We conducted FPMD simulations with van der Walls density functional optB88 at 330K and PBE at 400K. The two temperature were chosen to correct for inaccuracies of the two functionals in modeling the structure of water

Table 3.1: The lattice parameter of bulk Si relaxed with the van der Waals functional optB88 and semi-local functional PBE. The lattice constant of bulk Si obtained with the PBE and optB88 functionals are compared with previous simulation results as well as with experimental values. The lattice constants obtained with PBE and opbB88 differ by $\sim 0.1\%$.

Functional	Reference, Å[133]	Present work, Å
optB88	5.460	5.450
PBE	5.466	5.456

Exp. 5.416Å[133].

(See Ref. [3] and [134] for optB88 and PBE, respectively).

To analyze the structural properties of interfacial water, we computed the molecular dipole moment of water using maximally localized Wannier functions. A comparison of the results of the two functionals have been presented in Figure 3.2 and 3.3 showing similar results.

The calculations of the lattice parameters of Si slab and the structural properties of water using two functionals, have led us to conclude that for the objectives of this work using the PBE functional is sufficiently accurate and hence we conducted the simulations under bias using PBE.

To model the electrified interface, we performed simulations in the presence of an finite electric field by carrying out the calculation of the electronic ground state using the electric enthalpy as defined by Souza et al. [35]. A detailed theoretical introduction of FPMD simulations under an finite electric field calculation can be found in Chapter 2, Section 2.6.

At each step of the FPMD we minimized the electric enthalpy functional,

$$\mathcal{F}[u_{n\mathbf{k}};\mathbf{E}] = E_{KS} - \Omega \mathbf{P}_{mac} \cdot \mathbf{E} \tag{3.1}$$

Where $u_{n\mathbf{k}}$ is the periodic part of the field-polarized Bloch function, E is the macroscopic field, Ω is the unit cell volume, and E_{KS} is Kohn–Sham energy. The macroscopic polarization

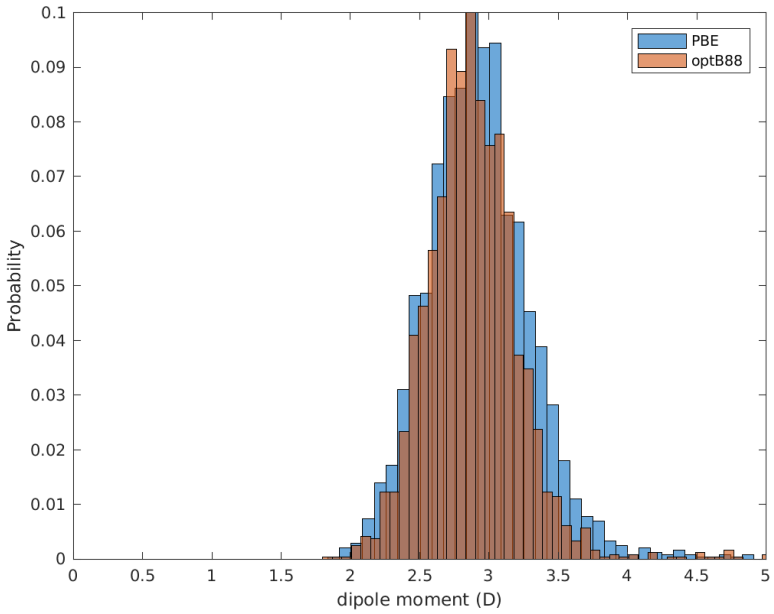

Figure 3.2: The probability distribution of molecular dipole moment of water obtained for PBE and optB88 equilibrated samples. The simulations were conducted with 124 water molecules and the BDP thermostat. When using PBE, the average dipole moment of water molecules is $\sim$ 2.93D, slightly smaller than that of the bulk PBE water $\sim$ 3.06D by 4.2%. Such a decrease has been previously observed close to surfaces and under confinement. [2] The average dipole moment of water molecules calculated with the optB88 functional ($\sim$ 2.88D) is slightly smaller than the PBE one, yet similar (1.7% difference), again consistent with previous reports [3]. The decrease relative to the optB88 bulk values $\sim$ 3.00D is 4.0%, similar to the decrease 4.2% found in the PBE case.

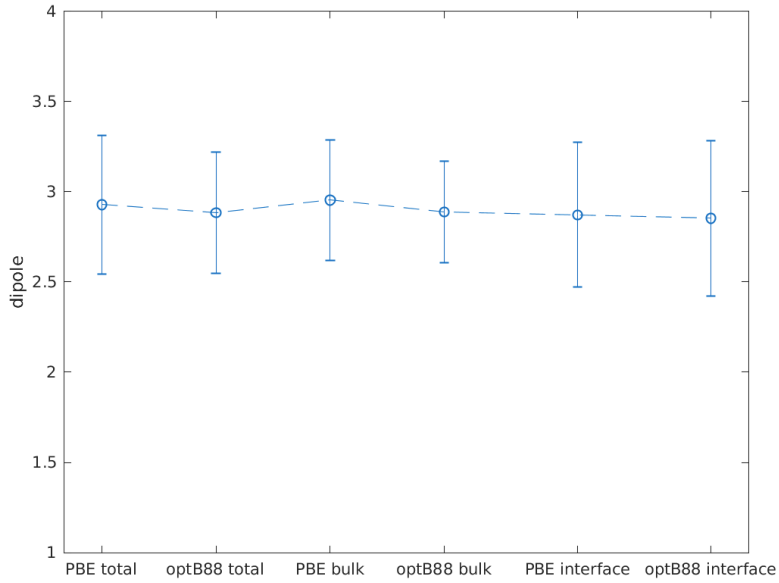

Figure 3.3: Molecular dipole moment (D) of water molecules in bulk and interfacial regions (within 5Åfrom the surface) of a simulation conducted with 124 water molecules using PBE and optB88 equilibrated samples. When using the PBE functional, we find that water molecules in the bulk region show a slightly larger dipole moment compared with those in the interfacial region, (2.95D vs. 2.87D). When using the optB88 functional, we find the same the trend: water molecules in the bulk region have a larger dipole than the interfacial region (2.89D vs. 2.85D). Comparing quantitatively the PBE and optB88 results, we find that the reduction of dipole moment from the bulk to the interfacial region is slightly more significant for PBE ($\sim 2.7\%$) than optB88 water ($\sim 1.4\%$).

$\mathbf{P}_{mac}$ was obtained using the Berry-phase theory [100, 101].

The electric field was applied along the direction perpendicular to the surface to model the accumulation of charge that results experimentally when using n-type Si interfaced with water. The field intensities were chosen so that built-in potentials are comparable to those of experimental PIN-Si structures [135], assuming the experimental thickness of the intrinsic layer to be around 150 nm [1]. The electric field intensities and built-in potentials used in our work are listed in Table 3.2. We note that the intensity of the electric field considered here corresponds to energies smaller than thermal energies, and hence the dynamics and structure of water were not perturbed during our FPMD simulations.

Table 3.2: The intesnisties of electric field applied to the H-Si/water interface in this study and the corresponding built-in potentials. The electric field was determined based on the thickness of the intrinsic layer ($\sim 150nm$) of the experimental PIN-Si structure, and the built-in voltage across a Si p-n diode junction ($\sim 0.7V$). We also considered smaller electric fields relevant to the electronic properties of Si-based bioelectronic devices.

Electric field, a.u	Voltage, V
0	0
4.6×10^{-6}	0.35
7.0×10^{-6}	0.54
9.5×10^{-6}	0.73

We equilibrated and collected FPMD trajectories for pristine and electrified samples for ~ 10 and 5 ps, respectively. For the equilibration process, we collected FPMD trajectories for pristine and electrified samples for ~ 10 and 5ps, respectively. We checked the equilibration process by monitoring whether the total energy of the system fluctuated at a stable value and whether the system temperatures reached the target. We also calculated the equipartition of energy between different species to verify the equilibration process, the normalized probability distribution of temperature for H, O and Si have been illustrated in Figure 3.4.

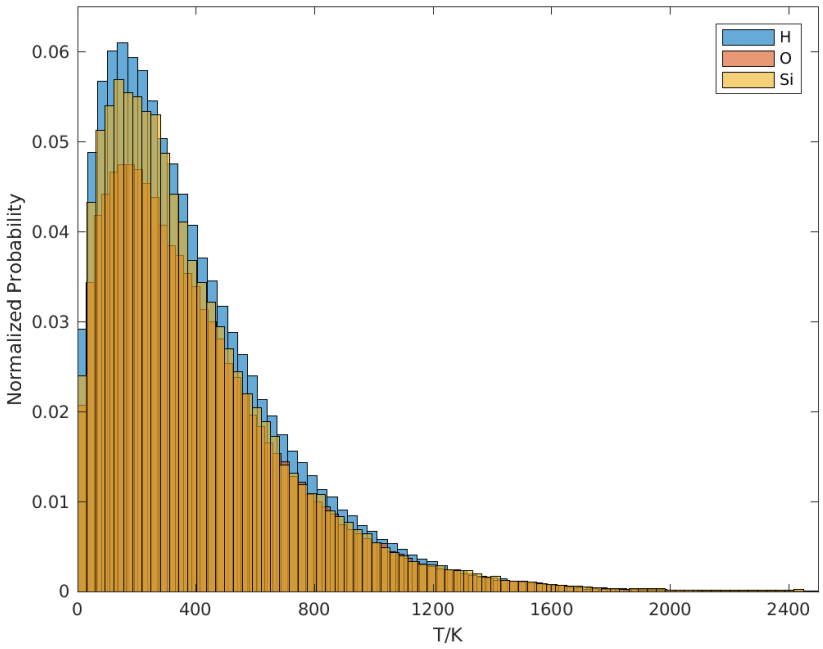

Figure 3.4: Normalized probability distribution of temperature (in terms of squared velocity) of individual species of the FPMD with a thermostat set to 400K for PBE functional. The average temperature for H, O and Si atoms are all reached the target temperature of 400K

The data for electronic structure calculations beyond DFT were originally obtained with the WEST code interfaced with Quantum ESPRESSO[136, 137]. The latter code was also used for STM image calculations.

3.2.2 Pulsed Chronoamperometry Measurements

In order to measure capacitive and Faradaic currents we performed pulsed chronoamperometry using silicon electrodes. Electrodes were prepared from (100) silicon wafers (550 μm, n-type, 0.001 to 0.005 Ω cm; Nova Electronic Materials). In short, a 5-nm chromium layer and 10-nm gold layer were deposited sequentially on the back side of the 10- $\times$ 10-mm wafer using an electron-beam evaporator (EvoVac; Angstrom Engineering). The connecting copper wires were then soldered to the gold contact. The connection, together with part of the front wafer surface, was insulated using a fast-set epoxy (MG Chemicals). The area of

tested electrode was ∼0.77 cm^2. Right before the measurement, the electrodes were cleaned in isopropanol in an ultrasonic bath for 5 min. Subsequently, the surface oxide was removed in concentrated HF (48 to 51%; Acros Organics) for 1 min. Finally, the electrode was soaked in ultrapure water for 1 min, washed with copious amounts of ultrapure water, and dried using compressed nitrogen.

Pulsed chronoamperometry was performed using a potentiostat (SP-200; BioLogic) controlled with EC-Lab Express. The time base of measurements was 140 μs. A platinum wire was used as a counterelectrode and an Ag/AgCl (1 M) electrode was used as a reference. For the measurement, the silicon electrode was put into the electrochemical cell filled with phosphate-buffered saline solution at room temperature and had the resting potential of ∼300 mV. A series of 500-ms pulses with variable negative potentials vs. initial electrode resting potential was applied to silver electrode and current transients were measured. The rest period between subsequent pulses was 1,000 ms. Transient currents were taken as a difference between the holding current and the specific points on the response curve: The capacitive current for each pulse was defined as a maximal negative recorded current and the Faradaic current as an average current observed in the last 25 ms of a pulse. The values represent a mean of three recordings from a representative electrode.

3.3 Results and discussion

After equilibrating the H-Si/water interface using FPMD, we computed band offsets and flat-band potentials as a function of the applied field to understand the qualitative behavior of capacitive currents as a function of the applied voltage. The magnitude of the electric field was chosen to be similar to that present when operating Si-based electronic, electrochemical, and photoelectrochemical devices in water [122]. Capacitive and Faradaic currents were also measured with the pulsed chronoamperometry method [138, 139] and used to validate our simulation results; in addition, computed STM images were used to characterize and

understand the origin of Faradaic processes.

3.3.1 Capacitive Currents

We start by discussing capacitive currents, which originate from an electron accumulation near the solid/water interfacial region, giving rise to an energy barrier at the interface. We investigate such an energy barrier by computing the band offsets between water and the silicon surface and the flat-band potential. The changes of band offsets and flat-band potential as a function of the electric field are indicative of changes in the electron accumulation at the interface, which in turn regulates the presence and magnitude of capacitive currents.

We computed band offsets of several snapshots and averaged the results, following the protocol of Ref. [22]. Twenty snapshots, evenly spaced in time, were extracted from an equilibrated MD trajectory, for which we computed the electronic structure at the density functional theory (DFT) level of theory.

We then corrected our DFT results for single particle energy levels using the G_0W_0 approximation [61, 60]. Our findings for nonelectrified samples were consistent with previous literature reports [22, 140]. The computed position of the valence band maximum of Si with respect to vacuum (-5.049 eV) is consistent with the experimental ionization potential 5.29 eV measured for an H-terminated Si(111) surface [141]. The band edge positions calculated at the PBE [50] level of theory and with G_0W_0 corrections, as a function of the applied field, are summarized in Table 3.3.

Our results show that the conduction band offset of the electrified samples is decreased with increasing intensity of the applied electric field (see Table 3.4), suggesting a lower energy barrier for electron accumulation at the Si surface or for electron injection into water. To quantify the energy barrier and the effect of the electric field on band bending, we computed the flat-band potentials U_{fb} of the Si surface at the electrochemical interface.

The flat-band potential U_{fb} is defined as the electrochemical potential of an interface at

Table 3.3: Valence band maximum (VBM) and conduction band minimum (CBM) of the H-Si/water interface, as a function of the applied electric field. The values were calculated using DFT with PBE functional and corrected using G_0W_0 approximation.

Voltage, V	VBM_{DFT}, eV	CBM_{DFT}, eV	$VBM_{G_0W_0}$, eV	$CBM_{G_0W_0}$, eV
0	-3.80	-4.55	-5.05	-3.70
0.35	-3.67	-4.42	-4.92	-3.57
0.54	-3.58	-4.33	-4.83	-3.48
0.73	-3.43	-4.18	-4.68	-3.33

Table 3.4: Computed valence band offsets (VBO), conduction band offsets (CBO), and flat-band potentials (U_{fb}) of the H-Si(100)/water interface as a function of the applied voltage. We report results including G_0W_0 corrections on results obtained by carrying out FPMD simulations at the DFT level.

Voltage, V	VBO, eV	CBO, eV	U_{fb} vs. vacuum, eV	U_{fb} vs. SCE, eV
0	4.01	2.60	-4.37	-0.31
0.35	4.14	2.47	-4.12	-0.56
0.54	4.23	2.38	-3.93	-0.75
0.73	4.38	2.23	-3.64	-1.04

which the semiconductor bands are flat [74]. For an n-type semiconductor, which we want to mimic here, it may be expressed with reference to vacuum as

$$U_{fb} = E_{CB} - \Delta E_F + V_{dip} + V_H \tag{3.2}$$

where E_{CB} is the position of the conduction band edge and $\Delta E_F$is the energy difference between the Fermi level and the conduction band edge. We determined the position of the Fermi level referenced to vacuum $E_F = E_{CB} - DeltaE_F$ as the midpoint between the conduction band minimum (CBM) and VBM. In Eq. 3.2, V_{dip} is the potential drop due to the dipole layer formed at the interface [142]. The electric field and solvation effect both contribute to determine the values of V_{dip}; since the VBM and CBM were computed in the presence of explicit water molecules, solvation effects are automatically included in our calculations. The contribution from the electric field was obtained from the difference of the electrostatic potential between electrified and nonelectrified samples. The values of E_F and V_{dip} are summarized in Table 3.5.

Table 3.5: The computed flat-band potential U_{fb} of different electrified samples at point of zero conditions; the V_{dip} and E_F were obtained from band alignment calculations. V_{dip} is the electrostatic potential difference between electrified and non-electrified Si(100)/Water structure. The E_F is determined as the midpoint between the CBM and VBM. Since the band edge positions were computed in the presence of water molecules, solvation effects are included.

Voltage, V	V_{dip}, eV	E_F, eV	U_{fb} vs. vacuum, eV
0	0	-4.37	-4.37
0.35	0.129	-4.25	-4.12
0.54	0.224	-4.15	-3.93
0.73	0.368	-4.00	-3.64

Finally, V_H is the potential drop across the Helmholtz layer due to ion accumulation

and absorption at the interface, which in the case of our simulation is zero since we did not include any ions. According to the Nernst equation, at room temperature

$$V_H = 0.059(pH - pH_{PZC}) \tag{3.3}$$

where pH_{PZC} is the pH value at which the point of zero charge (PZC) condition is realized. By setting V_H to zero, we computed the flat-band potential at PZC conditions; for an Si surface, such a condition corresponds to $pH = pH_{PZC} \sim 2$ to 3 [143]. In order to compare with experiments, the computed flat-band potential was referenced to the standard calomel electrode (SCE) on the absolute scale (-4.68 eV) [144]. Since the experimental flat-band potential for n-type Si can be sensitive to the exact surface termination and oxidation conditions (32), we compared our computed value with data measured from HF-treated Si samples which are expected to yield hydrogen-terminated surfaces such as those investigated in our simulations. The results, shown in the last two columns of Table 3.4, indicate that the computed U_{fb} are qualitatively in the range of the experimental U_{fb}, which is around -0.2 $\sim$ -0.6 at the PZC [145]. We note that the variability of experimental results may be due to measurements carried out in slightly different conditions; for example, the results may depend on the stage of the oxidation process at which the flat-band potential is measured.

Our simulations indicate that for n-type Si in solution the U_{fb} decreases with increasing magnitude of a negative electric field. Such a decrease is expected to lead to a higher degree of electron accumulation at the interface and hence to higher capacitive currents, or to an easier charge injection into water, which would produce Faradaic currents at the electrified n-type Si/water interface. These results are consistent with prior experimental observations, where the photoelectrochemical current produced from a photodiode subject to a larger photovoltage yields stronger amplitude of photocapacitive currents [1].

In order to validate the predictions of our FP simulations and the validity of the model used here, we performed pulsed chronoamperometry experiments (Figure 3.5) [138, 139],

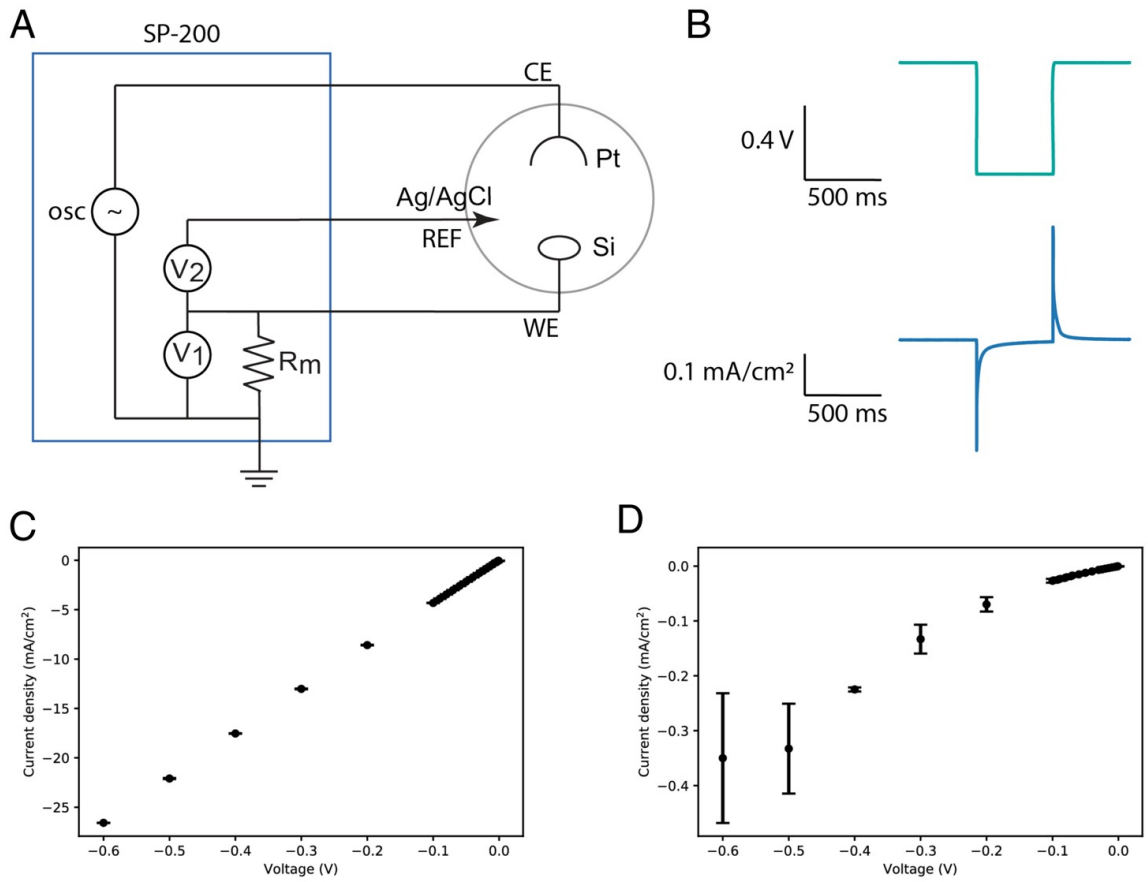

Figure 3.5: Pulsed chronoamperometry experiments using silicon electrodes. (A) Three-electrode experimental setup used for the measurements. (B) Representative voltage traces and recorded current response of the silicon electrode. (C) Capacitive current density and (D) Faradaic current density as the function of applied voltage. Both the capacitive and Faradaic current of wired Si wafer increases with the increasing of external electric field intensity.

where negative voltage pulses with different amplitudes were applied to newly prepared n-type Si wafers in an electrochemical setup. We observed that capacitive currents substantially increase with increasing applied voltage intensity (Figure 3.5C), consistent with the trend observed in our simulations (see Table 3.4), where the capacitive currents are predicted to increase with the increasing intensity of the electric field. In addition, we found that the Faradaic currents are significantly smaller than the capacitive ones and are weakly dependent on voltage in the high voltage range (Figure 3.5D).

3.3.2 Faradic Currents

We turned again to simulations to investigate Faradaic processes at the atomistic level, and to this end we computed STM images of the pristine and electrified H-Si/water interfaces. In the electrochemical measurements, the Faradaic current is associated with surface redox reactions. The change of ion concentrations leads to a charge redistribution in the interfacial region. Such process can be probed by placing a conductive tip near the surface (patch-clamp method), where the ionic flow from the surface to the tip are measured as Faradaic current signals.

The physical processes occurring in STM experiments are similar to those probed by the patch-clamp method [146] used to study Faradaic currents in several devices.

Here, we computed two-dimensional (2D) STM tunneling current images in planes parallel to the interface using the Tersoff–Hamann approximation[147, 148], and we evaluated the local density of states (LDOS):

$$LDOS(\epsilon, x, y) = 2\Sigma_i \left|\psi_i(x, y)\right|^2 \delta(\epsilon - \epsilon_i)|_z \tag{3.4}$$

where $(\epsilon, x, y$ is the single particle wave function projected on a given x–y plane, the factor of 2 accounts for the spin degeneracy, Σ_i denotes the Kohn–Sham eigenvalues, and z represents the position of the tip above the interface. The tunneling current (I) in the x–y plane can then be obtained from the integral of the LDOS:

$$I \propto \int_{\epsilon_f - eV}^{\epsilon_f} LDOS(\epsilon, x, y) d\epsilon \tag{3.5}$$

where ϵ_f is the Fermi energy and eV is the bias applied by the tip, which is chosen to be negative to model the electron transfer from the surface to the tip. We first determined the position of the virtual tip by identifying the interfacial region from the LDOS plotted along the direction perpendicular to the interface [149], as shown in Figure 3.6. The interfacial

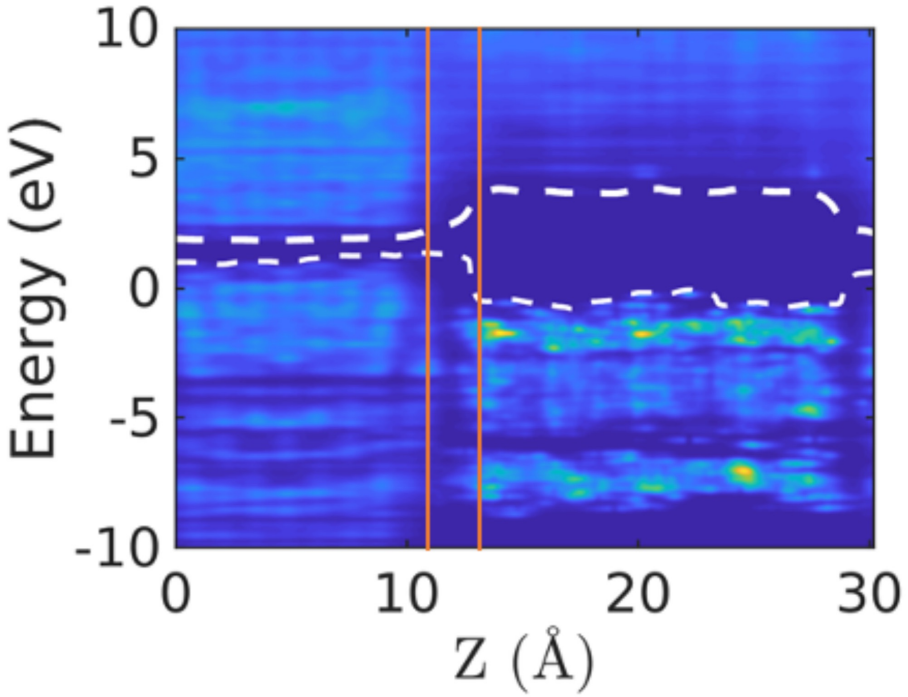

Figure 3.6: LDOS projected in the direction perpendicular to the interface (z); the VBM and CBM are indicated by white dashed lines. Note that the LDOS is computed here at the DFT/PBE level for the purpose of identifying an interfacial region, although our computed eigenvalues in Table 3.4 are all corrected using the $G0_W0$ approximation. The interfacial region is shown by the two orange lines.

region is approximately defined by the two lines parallel to the interface shown in the figure. In our model, we positioned the tip inside the interfacial region, i.e., around 2Å above the H atoms of the hydrogenated Si(100), thus capturing the current stemming from the interaction between the surface and the interfacial water molecules.

Figure 3.7 shows the tunneling current at constant voltage conditions (-200 meV, -700 meV, and -1 eV) obtained from Eq. 3.5 for the nonelectrified interface. Higher voltage probes energy levels of crystalline structure of Si, as apparent from Figure 3.7C. Note that increasing the tip bias does not change the position or area of the high-current-density region. We found that the high-current region originates from an interface state (shown in Figure 3.8A) which is generated by the presence of a dangling bond at the Si surface. Such a defect was introduced manually in our computational sample by removing an H terminating a Si

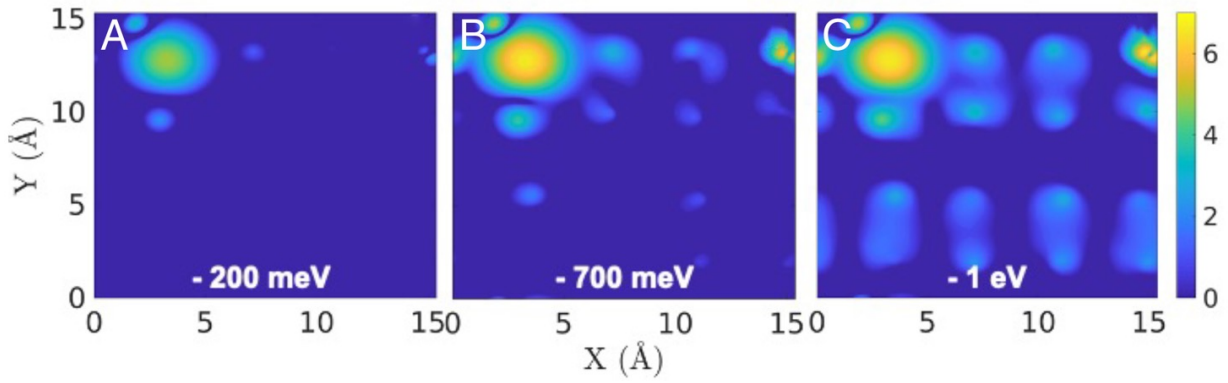

Figure 3.7: STM images computed at the interfacial region of the H-Si surface (see Figure 3.6) using Eq 3.5 at (A) -200 meV, (B) -700 meV, and (C) -1 eV. The high current density stemming from the surface reaction corresponds to the brighter region in the images. The color bar is in logarithm scale.

atom and letting it diffuse in the bulk of the water sample. This dangling bond in the computational sample mimics one of the processes which may occur experimentally in the early stages of the oxidization of a freshly prepared H-terminated Si substrate; such a process has been shown to produce hydrogen gas [150, 151].

We note that in our simulation the formation of Si–OH bonds, shown in Figure 3.8B, can be observed over short time scales, and we expect that such an event would appear multiple times in longer simulations. We also note that the occurrence of this bond was observed in simulations carried out with different density functionals (Figure 3.2 and Figure 3.3), and thus appears to be a robust feature of our computational model.

The oxidation of Si dangling bonds suggests that the Faradaic current might be measurable experimentally only for newly treated surface samples, before the reactive sites are gradually oxidized by water. We note that in the presence of Faradaic currents, devices with aqueous interfaces might degrade over time, consistent with experimental observations in transient electronics and the degradation of Si-based FET sensors.

We also computed the STM images for electrified samples shown in Figure 3.9, and found that the area or position of high-current-density regions showed barely any difference relative to the nonelectrified sample, confirming that the origin of Faradaic currents is related

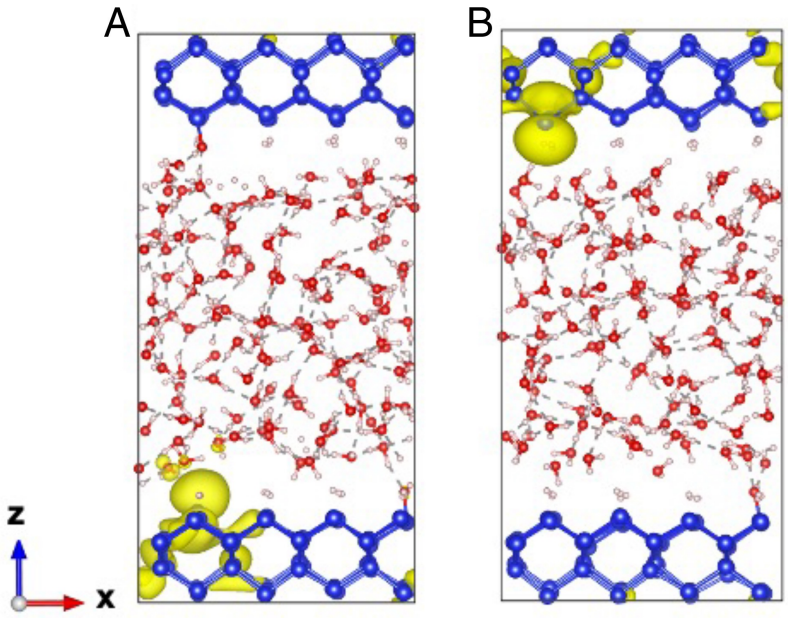

Figure 3.8: Iso-surface of the charge density (in yellow) for the states corresponding to a dangling bond at the surface (see main text). Silicon, oxygen, and hydrogen atoms are indicated by blue, red, and white spheres, respectively. A and B show two configurations of the surface.

to surface chemistry, on which the influence of the electric field is weak; however, the current density for electrified samples under the tip bias is slightly larger than for the nonelectrified counterpart, consistent with our electronic structure findings.

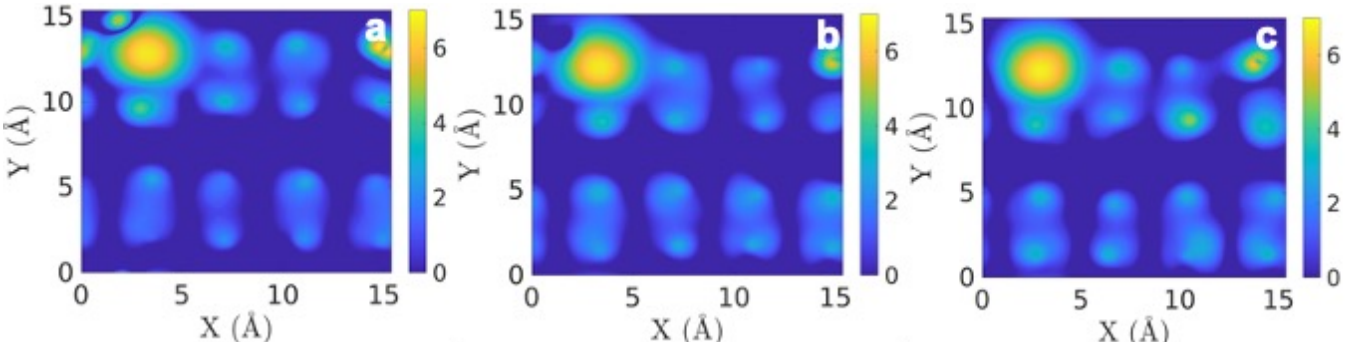

Figure 3.9: Computed tunneling current images (see main text) for a bias voltage -1eV for nonelectrified (a) and electrified (b,c) samples. In (b) and (c) the voltage applied to the interface is 0.35V, and 0.67V, espectively. The area and position for high current density regions is the same for electrified and non-electrified samples; the maximum current value is slightly larger in electrified samples than in non-electrified ones.

The results of our calculations showing that the Faradaic processes are weakly dependent

on the applied bias are validated by the trends observed in our pulsed chronoamperometry (Figure 3.5C and D) experiments: While the capacitive currents are linearly proportional to the applied volage, the Faradaic current grows slower in the voltage regime investigated in this study, where presumably not all dangling bond defects present at the surface have been oxidized. This observation also agrees with previous neuromodulation studies, where the intensity of Faradaic currents from Si-based modulators is not significantly enhanced by an increase of the photovoltage (i.e., use of p-i-n diode configuration versus a pure p-type Si)[1].

3.4 Conclusions

In this work we derived an atomistic model of electrified H-Si/water interfaces from FP to investigate capacitive and Faradaic currents at interfaces and gain insight into the functions of electrochemical devices at the microscopic level. We focused on Si(100), a prototypical semiconducting material, as Si is the most biocompatible and biodegradable of all known semiconductors, and thus relevant to many biological interface studies.

We explicitly devised experiments to validate our models and predictions. In particular, we computed the band offsets at the Si/water interface as a function of the electric field using methods based on DFT [29, 50] and many-body perturbation theory (GW) [61, 60]. We then determined the flat-band potentials of a Si electrode (energy barrier) as a function of bias and we found that it decreases when the intensity of the electric field increases, suggesting a high degree of electron accumulation in the case of n-type Si interfaced with water. Such an accumulation may lead to capacitive currents or to injection of charges ultimately responsible for Faradaic currents. The results of our simulations were validated by pulsed chronoamperometry measurements for Si wafers, which consistently showed that capacitive currents depend almost linearly on the magnitude of the applied field. These results are consistent with those of prior studies on the photoelectrochemical currents in Si

photodiode-based neuromodulation tools [1].

In addition, we analyzed Faradaic currents by computing 2D tunneling current images corresponding to STM experiments. Similar to the patch-clamp method in photoresponse measurements, STM experiments can probe the current originating from the electrode surface at a given bias and tip position. The tunneling current was obtained by integrating the local density of states (ILDOS) projected on a plane parallel to the surface [147, 148]. We found that the high-current-density regions observed in 2D tunneling current images correspond to interface electronic states arising from dangling bonds (defects) present at the Si surface, which we expect to be present in freshly prepared experimental samples. In our simulations we found that the magnitude of Faradaic currents is weakly affected by the presence and magnitude of the applied electric field or by doping, and these results were again confirmed by our patch-clamp experiments [1].

Our combined simulation and experimental study provided a comprehensive picture of the physical properties of the electrified H-Si/water interface and it represents a first, key step in understanding, at the microscopic levels, the Si-based electrochemical or photoelectrochemical devices relevant to transient electronics and biomodulation applications. Interestingly, our findings reveal a previously overlooked origin of Faradaic processes at the Si/water interface. As nanostructured Si has been widely used for a range of applications in solution, the defects of the Si surface (such as dangling bonds or Si–H bonds) may contribute significantly to Faradaic processes that are desirable for several applications, for example in the case of hydrogen evolution at the surface of nanoporous Si particles [152], or in the case of neural modulations with nanocrystalline Si nanowires [121].

CHAPTER 4

VIBRATIONAL SPECTROSCOPY OF ELECTRIFIED SEMICONDUCTOR AND WATER INTERFACES

This chapter is adapted from a preprint of a paper in preparation by Ye, Z., Zhao, F., Zhang, Y., Gygi, F., and Galli, G. (2023). "Computational and Experimental study of Raman spectra of electrified Si/Water interfaces".

4.1 Introduction

Aqueous interfaces play an important role in numerous electrochemical processes occurring, for example, in batteries [153, 154, 155, 156], bio-electronic devices [157, 158], and photo-electrochemical cells [159, 160, 161]. In many of these devices, the electrode surfaces are in contact with an aqueous electrolyte solution, and the interface is under the influence of an electric field. Electrons and ions are transferred at the interface, leading to chemical reactions and/or generation of electrical currents. The electrochemical properties of aqueous, electrified interfaces critically depend on the structural arrangement of interfacial water molecules, in particular on how the H-bond (HB) network is modified [162, 163], relative to that of pristine, bulk water [164]. The modifications of the network stem from the complex interplay between the influence of the surface in contact with the solution and the presence of an electric field [165, 164]. Therefore, investigating the structural and dynamical properties of water at electrified interfaces is an essential prerequisite to understanding and eventually optimizing the performance of electrochemical devices.

The number of hydrogen bonds between interfacial water molecules decreases with respect to the bulk liquid, leading, in many cases, to a weakening of the HB network and a spectral blue-shift of the O-H stretching band in vibrational sum frequency generation (SFG), Raman and infrared (IR) spectra [166, 167, 168]. The electric field is responsible for reorientation

of water molecules relative to the electrode surface [169, 170] and hence it is indirectly responsible for changes in the HB network. All of these effects contribute to a voltage-dependent evolution of the O-H stretching band of water at interfaces, as observed, for example, from in situ Raman spectroscopy [171].

Recently, the use of surface-enhanced Raman Spectroscopy (SERS) has enabled the study of aqueous interfaces with high sensitivity and selectivity [172, 42, 173]. In addition, the advancement of shell-isolated nanoparticle-enhanced Raman spectroscopy (SHINERS) has overcome the morphological constraints of SERS. Instead of being restricted to a rough plasmonic metal surface, SHINERS employs a monolayer of core shell nanoparticles [174, 175], enabling the measurements of Raman signals at the interface of water with several types of crystalline surfaces. This innovative technique has been applied to probe water dissociation and catalytic reactions occurring at electrified electrode surfaces [171, 176, 177].

While SHINERS has the potential to probe a wide range of material surfaces, its application has predominantly focused on metallic surfaces, where the local surface plasmonic resonance provided by nanoparticles can be further enhanced by the sample itself. However, for semiconductor/liquid interfaces, achieving high surface sensitivity remains a challenging task. Hence, a combined investigation using both computational and experimental techniques becomes indispensable for interpreting spectral features at the molecular level. This approach is particularly valuable in distinguishing the contributions of Raman signals from interfacial and bulk water molecules, which may facilitate a deeper understanding of electrochemical processes, including those relevant to photoelectrochemical water splitting and photocatalysis.

Computational studies of water at electrified interface have been carried out to explore electrochemical currents [36], surface-assisted proton transfer [178], and the structure of the electric double layer [179]. With the goal of interpreting Raman spectra, vibrational density of states (VDOS) have been calculated to investigate the O-H stretching mode of

water at electrified electrode surfaces [167]. However, the accurate calculation of Raman spectra of water at electrified interface is much more complex and demanding than that of the VODS, as it involves the calculation of polarization correlation functions [180, 181, 163], which require the use of first-principles electronic structure methods. The polarizability tensor can be evaluated using density functional perturbation theory (DFPT) [43] or by carrying out simulations in finite electric field, and obtaining the polarization from maximally localized Wannier functions (MLWFs) [134]. The Raman spectra are then obtained from the correlation function (TCF) of polarizability tensors [182] computed for snapshots extracted from first-principles Molecular dynamics (FPMD) [29] trajectories. Previous studies utilizing these methods have shown good agreement between experimental and computational spectra [43, 134, 113, 111, 45] of pristine water, but they have not yet been applied to electrified interfaces.

In this study, we combine computational and experimental methods to explore the Raman spectra of interfacial liquid water in contact with a semiconductor surface. In particular, we consider a hydrogenated silicon/water interface, as silicon(Si)-based materials are broadly used in electrochemical and photoelectrochemical devices. We employed FPMD to calculate the Raman spectra. In addition, by computing effective polarizability tensors we could establish a clear relationship between features in the spectra and structural properties of the water network at the interface and thus understand the influence and vibrational signatures of the electric field on the structure of the interfacial fluid. We found that in the case of the electrified interface under negative bias, the applied field leads to a reduction of the number of HBs formed between the H-terminated Si surface and the top most water layer, and to an enhancement of the HB interactions between water molecules, with signatures of these effects recognizable in the Raman spectra. Instead, for the electrified interface under positive bias, the applied field leads to an enhancement of both the HB interactions between water and the surface and between water molecules, leading to semi-ordered structures that give

rise to well-defined Raman peaks.

To validate our computational analysis, in-situ electrochemical surface-enhanced Raman spectroscopy measurements were conducted on electrified si/water interfaces. Notably, we observed a peak corresponding to the free OH group in the high-frequency region of the Raman spectra under a large negative bias. This observation indicates the presence of weakly hydrogen-bonded structures at the interface due to the combined effects of the surface and electric field, consistent with the proposed water structure identified in our computer simulations.

Overall, our work provides valuable insights into electrified semiconductor/water interfaces at the molecular level, and in particular into the identification of specific structural features through Raman spectroscopy. By combining first principles computational approaches and validating our results with experiments, we gained a deep understanding of the impact of an external electric field on water in contact with a semiconductor surface.

4.2 Method

4.2.1 Computational methods

Our model consists of 124 water molecules and an eight-layer H-terminated Si(100) slab [36]. We carried out FPMD simulations using the Qbox code [98] with the PBE exchange-correlation functional [183], and the Bussi, Donadio, and Parrinello thermostat [131]. The choice of the PBE functional is motivated by its ability to provide reasonable description of water at relatively low computational cost [132]. We used a plane wave basis set with a kinetic energy cutoff of 65 Ry and norm-conserving pseudopotentials [59]. The Γ point was used to sample the Brillouin zone of the periodically repeated slab used to represent the interface. The H-terminated Si(100) slab and liquid water were thermalized and equilibirated with FPMD at a target temperature of 400K (to correct for at least some of the inaccuracies

of the PBE functional for water), with a time step of 0.24 fs [132].

We modeled the presence of an electric field by calculating the electric enthalpy [35] and we obtained the macroscopic polarization using the using the Berry-phase method [100, 101]. The intensity of the electric field used in our calculations is 5.14×10^7 V/m. We note that the value chosen here is smaller than the field typically applied in experiments; our choice is based on the technical limit dictated by the band gap of silicon and the dimensions of the simulation slab along the direction of the applied field. The electric field is applied homogeneously along the direction perpendicular to the Si surface to model an electrified electrode/water interface, and Raman spectra calculations were performed for snapshots extracted from FPMD trajectories, by evaluating TCF of the polarizability tensor of the system. Details about calculations of the polarizability tensor and Raman spectra using the finite field method can be found in Chapter 2, Section 2.7.

The polarizability tensor $\boldsymbol{\alpha}$ can be decomposed into a isotropic $\bar{\alpha} = \frac{1}{3}Tr\boldsymbol{\alpha}$, and an anisotropic term $\boldsymbol{\beta} = \boldsymbol{\alpha} - \mathbf{1}\bar{\alpha}$, corresponding to the isotropic R_{iso} and anisotropic component R_{aniso} of the Raman spectra [43, 184], respectively:

$$R_{iso}(\omega) \propto \frac{\hbar\omega}{k_b T}\int dt e^{-i\omega t}\langle\bar{\alpha}(0)\bar{\alpha}(t)\rangle \tag{4.1}$$

$$R_{aniso}(\omega) \propto \frac{2}{15}\frac{\hbar\omega}{k_b T}\int dt e^{-i\omega t}\langle Tr(\beta(0)\beta(t))\rangle \tag{4.2}$$

where ω is the frequency shift of Raman spectra. In experimental measurements of Raman scattering, linear combinations of isotropic and anisotropic spectral components [182] are measured.

To further identify molecular contributions to the total Raman line shapes, we computed the polarizability tensor of individual water molecules in the liquid, as obtained from the derivative of the molecular dipole moment with respect to the electric field. We calculated

the dipole moment using MLWFs [108], as a function of simulation time $\boldsymbol{\mu}(t)$:

$$\boldsymbol{\mu}(t) = 6e\sum_i \boldsymbol{r_i^O}(t) + e\sum_j \boldsymbol{r_j^H}(t) - 2e\sum_k \boldsymbol{r_k^{MLWF}}(t) \tag{4.3}$$

where $\boldsymbol{r_i^O}(t)$ and $\boldsymbol{r_j^H}(t)$, are the coordinates of the Oxygen and Hydrogen atoms, and $\boldsymbol{r_k^{MLWF}}(t)$ is the coordinate of MLWFs centers belonging to a water molecule. Within the Born-Oppenheimer approximation, the polarzaibility tensor $\boldsymbol{\alpha}$ at time t can be obtained from the response of the dipole moment under a small electric field $\boldsymbol{E}$.

$$\boldsymbol{\alpha}(t) = \frac{\delta\boldsymbol{\mu}(t)}{\delta\boldsymbol{E}} \tag{4.4}$$

The effective polarzability $\boldsymbol{\alpha}_i$ of single water molecules was obtained by applying the electric field along each of the Cartesian axes. Note that the effective polarizability is the projection of the total poalrizability tensor onto each single molecule in the system, and it includes dipole-induced dipole contributions; hence, the effective polarizability differs from the molecular polarizability, which only depends on the electronic structure of the molecule. When summing the effective polarizability tensor over all of the species in the system, we obtain the total polarizabilty.

$$\boldsymbol{\alpha}(t) = \sum_i \boldsymbol{\alpha}_i(t) \tag{4.5}$$

We decomposed the Raman spectra into interfacial contributions by selecting water molecules residing in proximity of the surface and calculating their corresponding effective polarizability tensors. The Raman line shapes of interfacial water molecules could then be obtained from the TCF of effective polarizability tensors.

4.2.2 In-situ electrochemical Raman measurements

In-situ electrochemical SHINERS measurements were carried out in a commercial cell from Dek Research. A 'Si film on Au nanoparticle' configuration was used to serve as the working electrode, and Ag/AgCl (BASi MF-2052) and Pt wire (CHI 115) were used as reference and counter electrodes, respectively. Specifically, the working electrode was prepared by sputtering 2 nm of Si onto Au nanoparticle decorated Au substrate. The thickness and coverage of the deposited Si layer were verified by scanning transmission electron microscopy (STEM, ThermoFisher Scientific Talos F200X G2), as shown in Figure 4.1. Electrochemical measurements were performed using a CH Instrument 600E potentiostat. Raman measurements were carried out using a Horiba LabRAM HR Raman spectroscopy imaging system. The objective lens was 50× and the grating was 300 grooves/mm. The laser source has a wavelength of 633 nm, and the power was selected to be $\sim$ 3.5 mW.

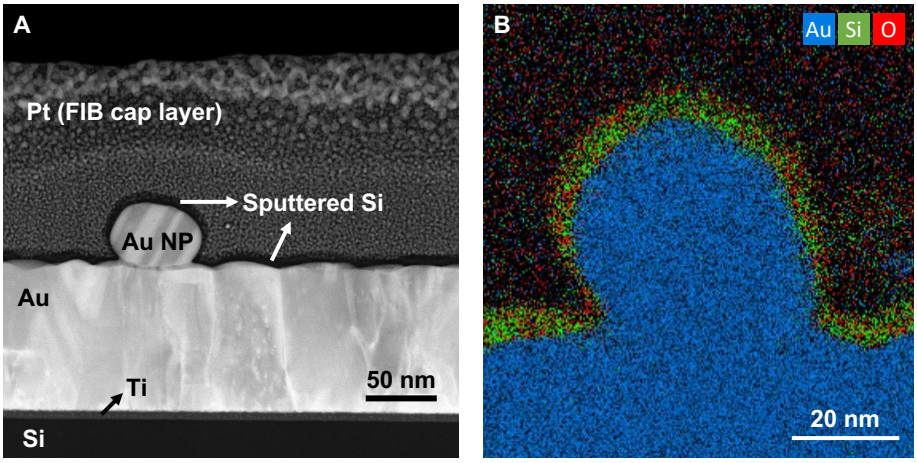

Figure 4.1: Thickness and coverage of SiO_2 layer (Si layer after oxidation). A. STEM image of the cross-section of the sample. The SiO_2 layer was proven to cover the entire surface of Au substrate and Au nanoparticles, though at the side-wall area it is a bit thinner. The thickness of the SiO_2 layer is around 4 nm. According to the expansion ratio of Si oxidation, the original Si layer is supposed to be around 2 nm thick, ensuring a good enhancement effect. The Pt layer was introduced in the slice sample preparation process with focused ion beam (FIB, FEI Helios 600i Dual Beam SEM/FIB). B. Energy dispersive spectra (EDS) mapping of elemental distribution.

4.3 Results and Discussion

4.3.1 Structural properties and Raman spectra of the pristine Si-H/Water interface

The analysis of HBs of water in the pristine H-Si/Water interface was conducted on FPMD trajectories [36], and we plotted the average number of H-bonds as the function of z (the direction perpendicular to the surface) in Figure 4.2 left.

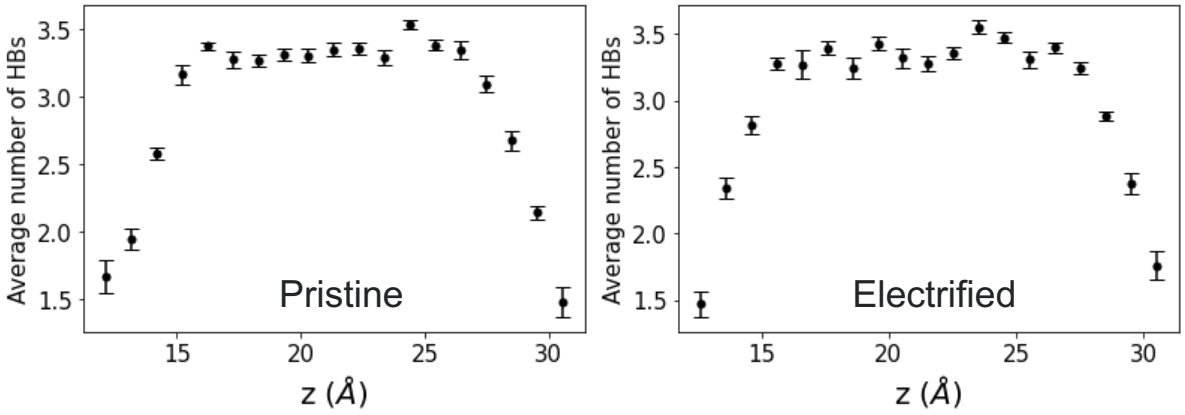

Figure 4.2: The computed average number of H-bonds as a function of the vertical distance from the surface (z) for a pristine (left) and electrified (right) interface.

We considered two molecules as H bonded if the distance between the Oxygen and Hydrogen atoms was in the range of 1.3 Å to 2.5 Å and the O-H$\cdots$H angle was less than 30 degrees [185]. The distance cutoff was based on the computed Oxygen-Hydrogen pair distribution function. As expected, the average number of HBs for water molecules in the bulk region was found to be approximately 3.5, while a reduced number of HBs of less than 3 was observed for water molecules near the substrate. The decrease in the number of HB at the surface is accompanied by a decrease of the dipole moment of interfacial water molecules relative to those in the bulk region (2.87D vs. 2.95D), consistent with other interfacial studies [2].

We first computed the vibrational density of state (VDOS) of the nonelectrified H-Si/Water structure from the TCF of the velocities and identified the contributions of different

species in the system to the various peaks, as illustrated in Figure 4.3. We observed that the vibrations of Si-H bonds give rise to the bands at approximately 600 cm^{-1} and 2100 cm^{-1}, corresponding to Si-H bending and stretching modes [186], respectively. The O-H stretching at 3000-3800 cm^{-1}, librations at 500-600 cm^{-1} and bending at 1600 cm^{-1} are related to contributions from liquid water [187].

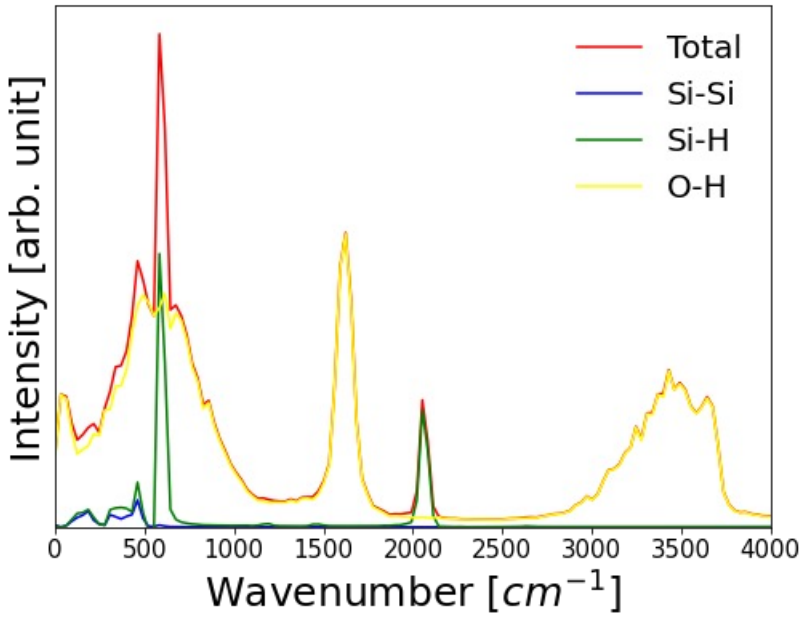

Figure 4.3: Vibrational density of states of the pristine H-Si/water interface computed from the velocity/velocity correlation function and averaged over first-principles MD trajectories.

We then calculated the isotropic and anisotropic Raman spectra of the nonelectrified Si/Water interface based on the system's polarizability tensors, as shown in Figure 4.4. We observed a peak at 2000-2100 cm^{-1}; these frequencies are within the range of vibrational frequency of the Si-H stretching mode calculated from the VDOS. The broad peak at 2800-3800 cm^{-1} is related to the O-H stretching mode of water. The peak at about 500-600 cm^{-1} arises from the librations of water and from the Si-H bending mode. The positions of all these peaks are consistent with those observed in the experimental Raman spectrum measured for Si films in contact with water [188, 189, 180].

The isotropic contribution of the Raman spectrum is independent of the orientation of

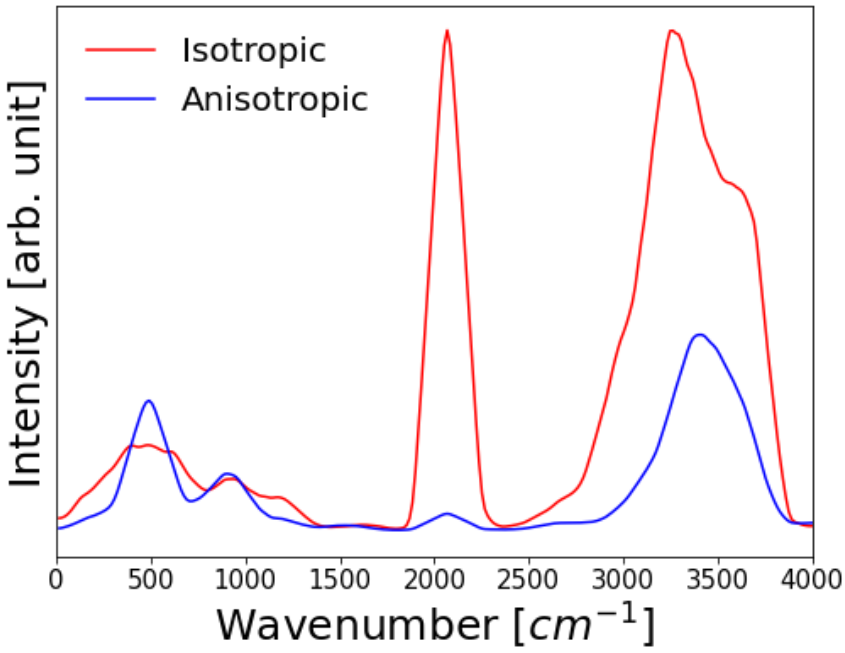

Figure 4.4: Computed isotropic (red) and anistropic (blue) Raman spectra of the H-Si/Water interface obtained from the time correlation function of the total polarizaiblity tensor of the slab used in our simulations.

the sample relative to the polarization of the incident light. Here, we find that the isotropic contribution is larger than the anisotropic one for both the Si-H stretching and O-H stretching modes, due to a more pronounced effect of the thermal contribution to these modes.

We also observe a shoulder at 3500-3700 cm^{-1} in the O-H stretching band of the isotropic spectrum. This feature arises from the weakened HB network in the interfacial water region [190], as discussed above. A similar peak shift was reported for the CCl_4/H_2O interface and attributed to the reduction in coordination number of interfacacial water molecules [166], but such a surface-dependent feature has not been observed before in the Raman spectra for electrode/water interfaces.

To further investigate and isolate the contribution to the Raman spectra from specific interfacial water molecules, we selected specific molecules in the interfacial regions, based on their vertical distance from the plane of the H atoms terminating the surface; we selected molecules within 3Åto 6Å. We then computed the contributions of those interfacial water

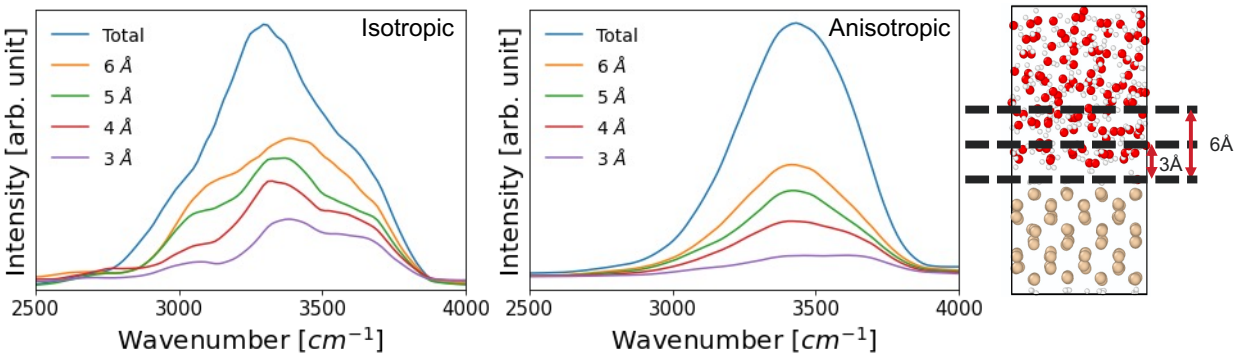

Figure 4.5: Isotropic (left panel) and anisotropic (middle panel) contributions to the Raman spectra of the pristine H-Si/Water interface, arising form water molecules at various distances from the surface, as indicated by the lines of different colors (see also rigth panel).

molecules to the O-H stretching mode of the Raman spectrum as a function of the distance from the surface, as shown in Figure 4.5. We observed a broad O-H stretching band in both the isotropic and anisotropic spectrum, arising from several different HB configurations in liquid water. We identified three prominent peaks present in the isotropic spectrum, at 3100-3200 cm^{-1}, 3300-3400 cm^{-1}, and 3500-3700 cm^{-1}, which we assigned to four-fold coordinated (4HB), three-fold coordinated (3HB) water molecules and to free OH groups present in the interfacial water layer, respectively. Peaks in the same frequency range were also observed in the experimental in-situ electrochemical Raman spectra of Pt-Ni nanoparticles in contact with water [191].

By computing the area under each peak, we could estimate the percentage ratio corresponding to four-fold, three-fold coordinated water molecules and free OH groups, as shown in Figure 4.6.

The number of 4HB water molecules responsible for the peak at 3100-3200 cm^{-1} decreases when approaching to the surface, while the number of free OH groups responsible for the peak at 3500-3700 cm^{-1} increases. Three-fold coordinated configurations dominate in the interfacial region. Hence we conclude that the overall blue-shift feature observed in the O-H stretching band of the Raman spectrum arises from three-fold coordinated water molecules at the interface.

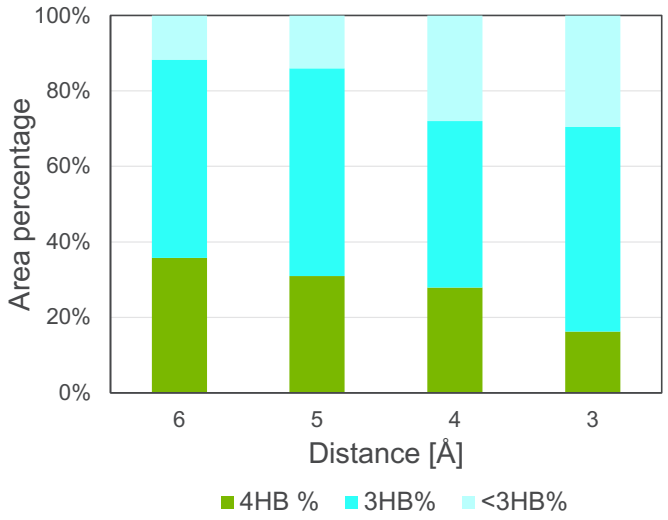

Figure 4.6: Area percentage for peaks correspond to tetrahedral 4HB, trihedral 3HB and H-bond acceptor < 3HB structures, respectively, measured from isotropic Raman contributions as the function of different interfacial regions.

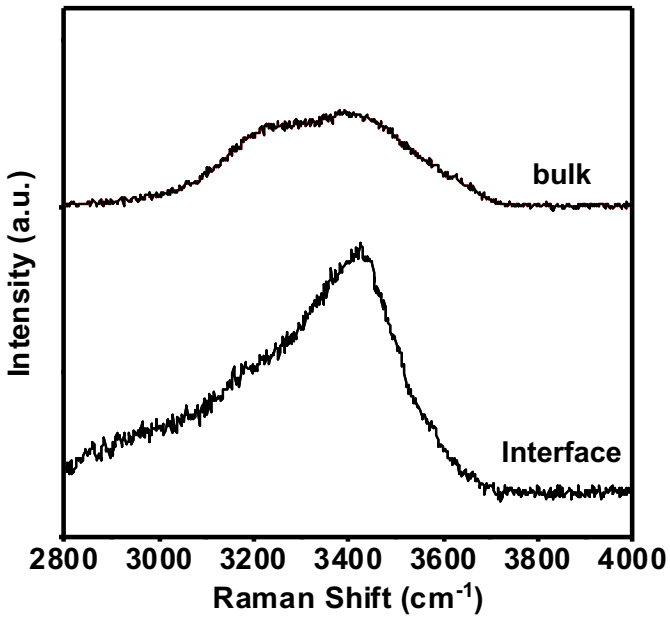

Figure 4.7: The Raman spectra of bulk and interfacial water in contact with a Si surface measured by in-situ electrochemical SHINERS.

Figure 4.7 displays the experimental Raman spectra of water obtained in the bulk and interfacial regions. We note that the surface enhancement effect is weak as no potential was applied during the measurement; hence, the signal from the free OH structure was not enhanced. Nevertheless, a comparison between the Raman spectrum of bulk water and that of interfacial water does reveal the effect of the surface on the liquid. The interfacial water spectrum exhibits a sharp peak at approximately 3400 cm^{-1}, corresponding to 3-fold HB molecules, while the peak arising from 4HB molecules at approximately 3200 cm^{-1} is weaker. These results are consistent with our computed Raman line shapes, where a decrease in the intensity of 4-fold coordinated molecules was observed in the interfacial region.

In the next section, we investigate the impact of an electric field on the structural properties of water molecules, addressing realistic operation conditions encountered in many electrochemical devices.

4.3.2 Structural properties and Raman spectra of the electrified Si-H/Water interface

In our FPMD simulations, we applied a homogeneous external electric field along the direction perpendicular to the surface, as shown in Figure 4.8. Hence, two electrified surfaces were created in the periodically repeated slab, one subject to a positive bias and the other one subject to a negative bias. In this section, we discuss the effect of the electric field on water under both positive and negative bias conditions, mimicking conditions leading to either hydrogen evolution reactions (HER) or oxygen evolution reactions (OER) [192] at electrode surfaces. Further, as well known, Si-based devices such as supercapacitors and transistors rely on an applied voltages for their operation [1, 120].

As expected, we find that when the electric field is pointing towards the surface (electrified surface under negative bias), the H atoms of the topmost layer of water in contact with the semiconductor tend to be closer to the Si slab than in the absence of the field; on the other

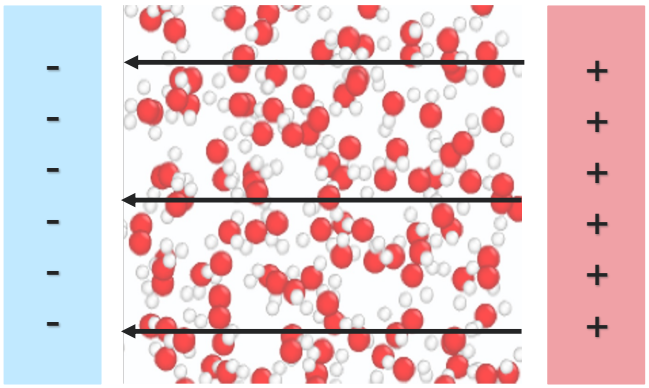

Figure 4.8: Schematic illustration of the direction of electric field and electrified interfaces.

hand, for electrified surfaces under positive bias, O atoms tend to be closer to the Si slab. To study the modification of water geometries due to the electric field, we calculated the average number of HBs as a function of the position of the water molecules along the z-axis, using the same criterion to define HBs as used in the previous section (see Figure 4.2 right).

We compare the percentage difference of HBs in nonelectrified and electrified interfaces, as a function of z: $\%\frac{nonelectrified-electrified}{nonelectrified}$ in Figure 4.9. Given the reorientation of molecules by the field, HBs are less likely to form between interfacial water molecules and the surface under negative bias; in the water region 1-2 Å from the surface, the number of HBs is larger in the nonelectrified surface under negative bias. Instead, in the case of positive bias, where O atoms are closer to the surface, HBs are easier to form between the first layer of water and the H-terminated surface, and the number of HBs at the electrified surface increases. The influence of the electric field goes beyond the topmost layer, where water molecules are also re-oriented, resulting in a relatively ordered layer of interfacial water molecules. As a result, we observe an increase of HBs formed in the region 2-3 Å above the surface for both electrified surfaces, regardless of the field direction.

In summary, we found that the HBs formed at electrified interfaces under negative bias decrease relative to pristine interfaces, while in the presence of a positive bias the number of HBs increases. However, in both cases a relatively ordered HB network above the topmost layer of interfacial water molecules forms, where the number of HBs increases. We now move

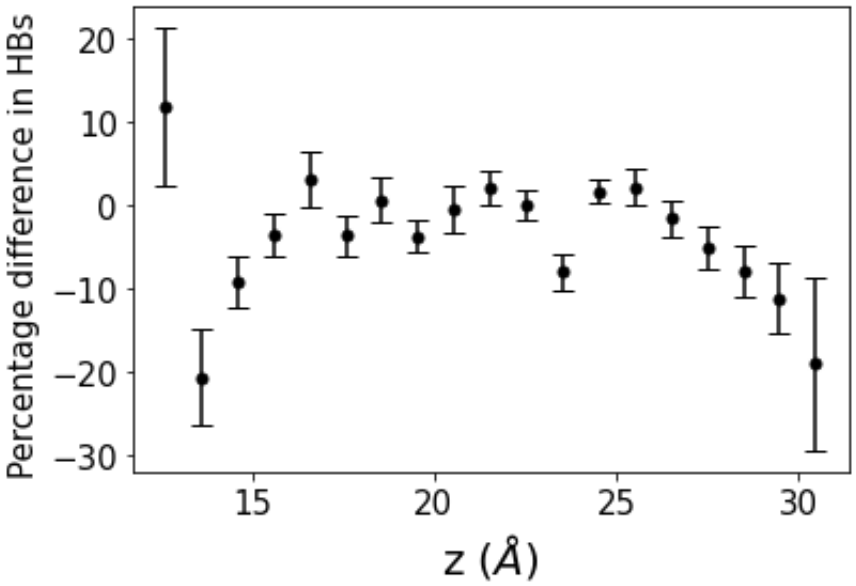

Figure 4.9: Difference in the number of hydrogen bonds (HB) between a pristine and electrified H-Si water interfaces. The interface under positive (negative) bias is positioned at approximately 30 and 12.5 Å, respectively, in the slabs used in our calculations.

to investigate the signatures of these interfacial modifications in the Raman line shapes.

The calculated the isotropic and anisotropic Raman line shapes of interfacial water molecules obtained from interfaces under positive and negative bias, respectively, are illustrated in Figure 4.10.

We find a splitting of the peaks at 3300-3400 cm^{-1} and 3500-3700 cm^{-1} in the anisotropic Raman line shape of the electrified interface, as shown in Figure 4.10, which is not present in anisotropic line shapes of the pristine surface (Figure 4.5). Based on our structural analysis, the splitting is ascribed to the effect of the external electric field on the orientations of water molecules, which in turn lead to a more ordered HB network above the first interfacial layer, compared to the pristine case.

The effect of the surface, which results from the low-coordinated configurations of interfacial water molecules, leads to peaks at 3500-3700 cm^{-1}. The effects arising from the electric field lead to the merging of the peak at 3100-3400 cm^{-1}, corresponding to 3- and 4-fold hydrogen bonded water molecules. In the case of the positively electrified interface,

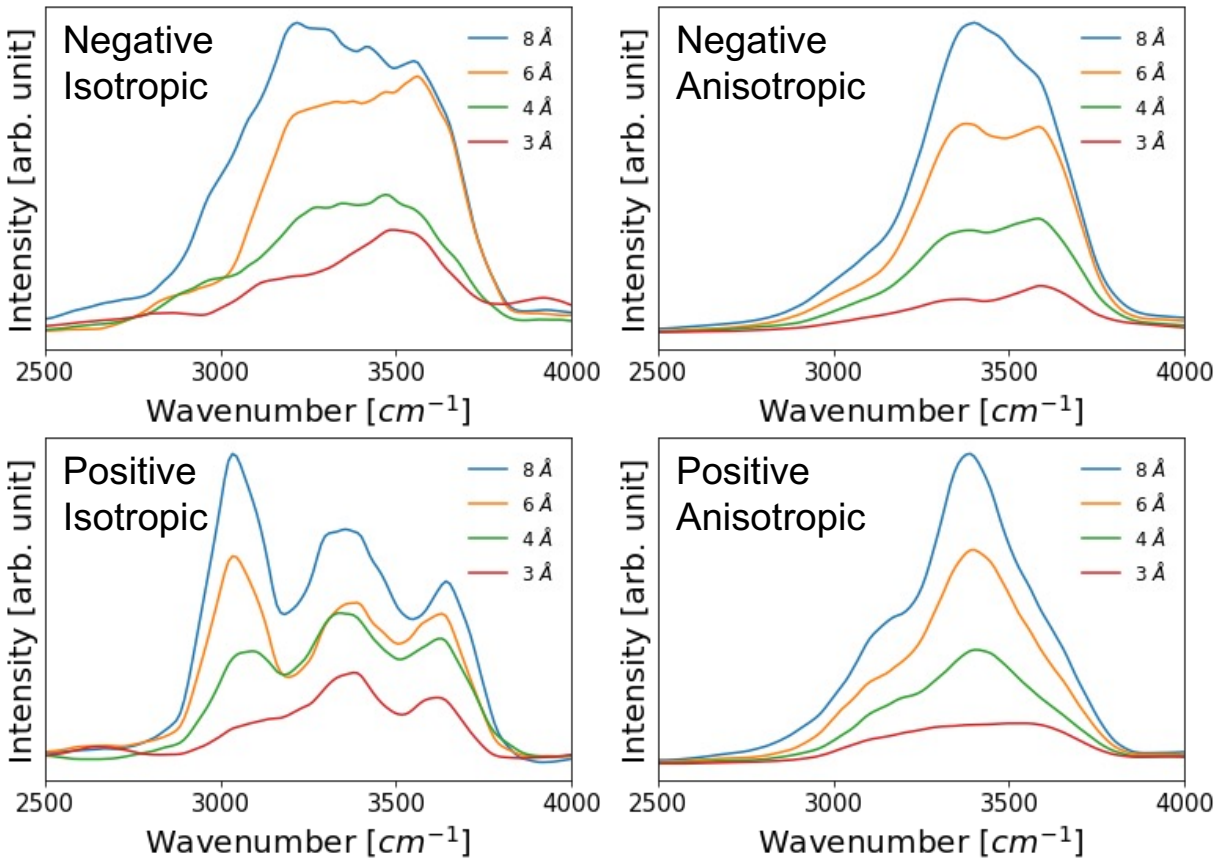

Figure 4.10: Isotropic (left panels) and anisotropic (panels) contributions to the Raman spectra of electrified H-Si/Water interfaces (negative bias, upper panels; positive bias, lower panels) , arising form water molecules at various distances from the surface, as indicated by the lines of different colors.

the presence of ordered structures lead to well-defined peaks at 3100-3200 cm^{-1} and 3300-3400 cm^{-1}. Although the peak corresponding to free OH bonds at 3500-3700 cm^{-1} is more intense for interfacial water molecules, the signal arising from 3-fold coordinated molecules is continuously observable from the bulk to the surface region, indicating the presence of a stable HB network induced by a positive bias at the H-terminated surface.

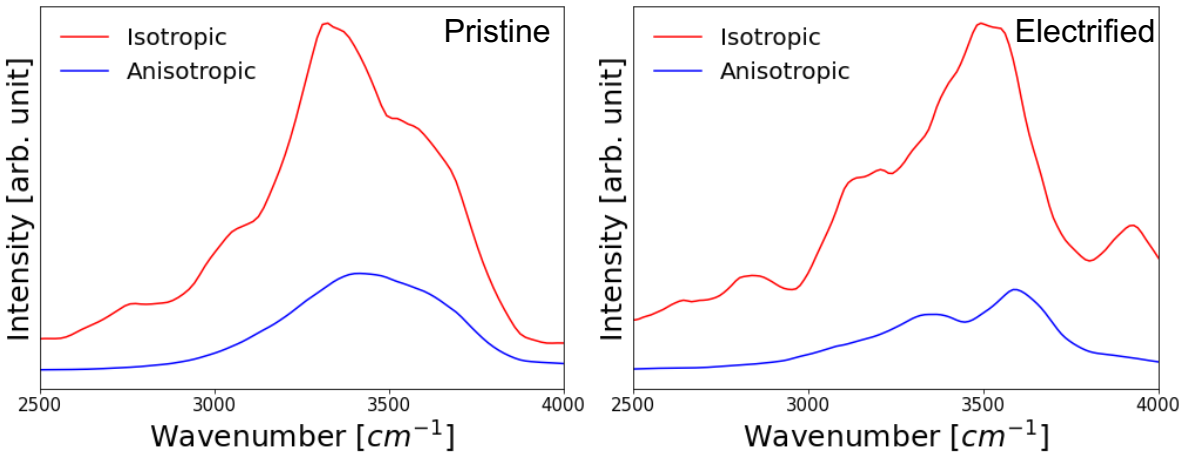

Figure 4.11: A. The isotropic and anisotropic contributions to the O-H stretching mode in Raman spectra from interfacial water molecules at 3 Å above the nonelectrified surface. B. The isotropic and anisotropic Raman contributions of interfacial water molecules at 3 Å above the surface under a negative bias.

We also compared the Raman contributions of interfacial water molecules in the case of nonelectrified and negatively electrified surfaces in the same region (3 Å from the surface), as shown in Figure 4.11 A and B. In the case of the electrified surface, we observed a relatively intense peak at 3100-3200 cm^{-1}, indicating that the number of 4-fold coordinated molecules is larger at the electrified interface. The ratio between the area of the 3100-3200 cm^{-1} peak and the total area of the stretching mode part of the spectrum is 16% and 9% for electrified and non electrified samples, consistent with our analysis of the geometry of water molecules in the interfacial layer, shown in Figure 4.9.

We obtained experimental in-situ Raman spectra of the Si/water surface using surface-enhanced Raman spectroscopy for a sample under negative bias. With the enhancement

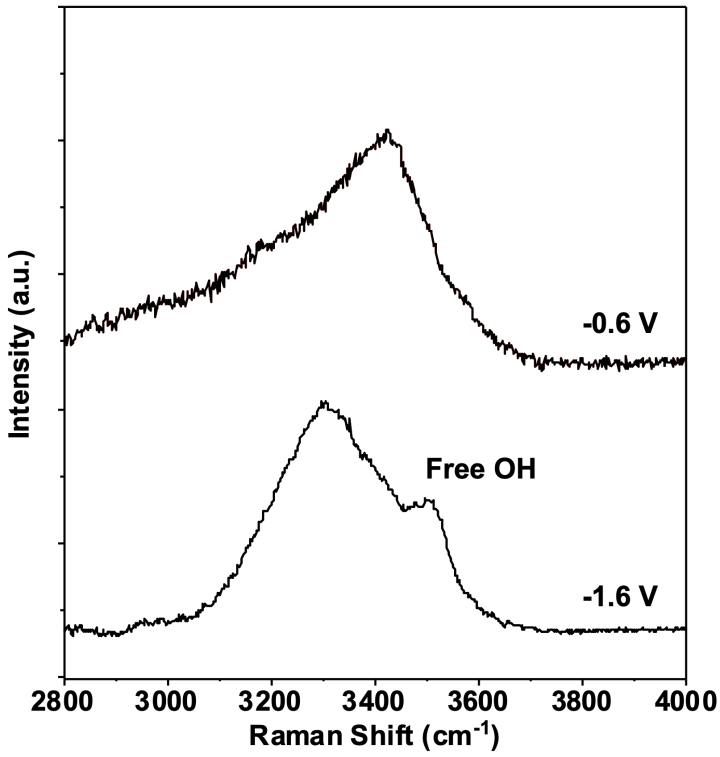

Figure 4.12: The Raman spectra of interfacial water measured by in-situ electrochemical SHINERS under a negative potential.

effect provided by Au nanoparticles, we could observe Raman signals from the interfacial water molecules. Figure 4.12 illustrates the effect of the applied negative voltage on the Raman peaks, resulting in an overall red-shift of the bands. At a voltage of -1.6V, a shoulder at 3500 cm^{-1} was observed in the spectrum, indicating the presence of free OH groups. This observation is consistent with our computed spectra for a negatively electrified Si-H/Water structure, where water molecules are less likely to form HB with the surface. Notably, the experimental peak corresponding to free OH becomes observable when the applied negative voltage exceeds 1.6V. This finding might suggest that the large negative potential further enhances surface signals and prevents the surface oxidation reactions that may influence the detection of interfacial water signals, specifically the presence of free OH groups.

4.4 Conclusion

We presented a first-principle study of water in contact with a H-Si surface and we identified Raman signatures of specific geometric arrangements at the interface, which were validated by experimental measurements. We studied both pristine and electrified interfaces under negative and positive bias. In the case of the pristine surface, we found that the shoulder present in the O-H stretching band can be ascribed to the modifications of the water HB network due to the presence of the surface. We also calculated the Raman contributions of interfacial water molecules and found that free OH bonds give rise to a peak in the high frequency region, which leads to a blue-shift of the O-H stretching band relative to that of bulk water. In the case of electrified interfaces we found that a negative bias weakens the HB interaction between the top most layer of water and the surface, while a well-defined HB network with sharp Raman peaks in the low frequency region are obtained for the interface under a positive bias. The free OH line of interfacial water molecules is observed from in-situ Raman spectroscopy under a large negative potential, validating the proposed water structure obtained in our simulations. By using validated first principles simulations

our work give insights on Raman signatures of the geometrical arrangements of water at an hydrophobic semiconductor interface. The approach employed in our study is general and can be used to explore intricate electrochemical characteristics of electrode-electrolyte systems.

CHAPTER 5

ELECTRONIC PROPERTIES OF WATER AND AQUEOUS SOLUTIONS UNDER EXTREME CONDITIONS

This chapter is reproduced with permission from Ye, Z., Zhang, C., and Galli, G. (2022). Photoelectron spectra of water and simple aqueous solutions at extreme conditions. Faraday Discussions, 236, 352-363.

5.1 Introduction

Water-rich fluids are important constituents of the Earth's crust and mantle [193, 194, 10]and they play a central role in many fundamental processes, including metasomatism [195], transport of oxidized carbon [23, 45] and ultimately in the evolution of the continental crust [10]. The presence of so called deep-earth aqueous fluids has been reported in aqueous pockets in diamond [196], metamorphic minerals [197, 198] and stable hydrous silicate minerals under pressure (P) [199], and inferred from seismic data [200] and conductivity measurements[201, 202].

While most of the current knowledge of deep-earth aqueous fluids comes from geophysical models [203, 204, 205, 206, 207, 208, 40, 209, 210, 211] and from vibrational spectroscopic measurements, progress has been made in recent years in understanding the properties of these fluids at the microscopic level, using first principles simulations. The latter have been used to investigate fundamental properties at high P and T (HPT) including the dielectric constant of water[212, 102], ionic speciation[23, 45], ion solvation [213, 31] and ionic conductivity of simple solutions [25, 214, 215, 30]. However, relatively little is known about the electronic structure [216] of aqueous fluids under extreme conditions, which is important to understand, for instance, electron and proton transfer processes in redox reactions occurring [217, 218] in water and solutions in contact with rocks in the Earth's interior.

Many electronic structure probes used at ambient conditions are difficult to employ at high temperature and pressure. For example, photoelectron (PE) spectroscopy has been widely used to probe the electronic properties of hydrogen bonded liquids, providing information on their occupied energy levels [219, 220, 221], including the ionization potentials (IP) of solvated ions [222, 223, 5, 224], e.g. hydrated OH^-, H_3O^+, Cl^-, Na^+, thus elucidating their structural and chemical environment. However, obtaining PE spectra for HPT water and solutions is a challenging task not only because of the reactivity of water at high P and T, but also for the difficulty in preparing super-critical liquids in contact with vacuum and detecting PE signals with high time-resolution in the presence of rapid thermal expansion[225, 226, 227].

First principles theoretical methods based on quantum mechanical calculations have been applied to predict the PE spectra of several aqueous solutions at ambient P and T (APT)[5, 224, 115, 228, 229], providing results in excellent agreement with experiments. In particular, recent investigations have shown that a combination of first-principles molecular dynamics (FPMD) and density functional theory calculations with dielectric-dependent hybrid (DDH) functionals [46] is a robust, predictive approach to study photoelectron spectra of aqueous fluids [5, 224]. It is hence interesting to explore how to predict PE under extreme conditions and gain insight into the electronic properties of aqueous fluids at high P and T.

Here, we generalize the approach recently used to compute PE spectra at ambient conditions to the study of aqueous fluids under pressure, at high temperature. We carry out first principles simulations with semilocal and hybrid functionals, and we consider two specific systems at conditions (11 GPa and 1000K) relevant to the Earth upper mantle, where pressure can reach $\sim$ 13 GPa and temperature $\sim$ 1700K [230, 231]; in particular we investigate pure water and a 0.68 M NaCl solution, whose structural and bonding properties have been previously studied[30, 31]. We report PE spectra on an absolute scale, by using a technique to refer energy levels to vacuum which is appropriate for hot compressed fluids; we discuss

results obtained with dielectric-dependent hybrid functionals, and with a fraction of exact exchange determined for the specific conditions studied here [216]. We also analyze the contribution of dissociated species to the PE spectra, in particular hydroxide (OH^-), hydronium (H_3O^+) ions and H_4O_2, which play an important role in proton transfer processes and acid-base chemistry [232, 233, 234], and contribute to the increased ionic conductivity [30] of water under extreme conditions.

The rest of the paper is organized as follows: the methods used here are described in the next section, followed by a discussion of our results and conclusions.

5.2 Methods

5.2.1 First-principles simulations and electronic structure calculations

We consider the FPMD trajectories generated at 11 GPa and 1000 K by Rozsa et al. and Zhang et al.[30, 31] to model pure water and a 0.68 M NaCl solution, respectively. These trajectories were obtained with the Qbox [98] code, employing the Perdew–Burke–Ernzerhof (PBE) [50] functional, with 64 water molecules to model pure water and 126 water molecules and 1 NaCl formula to model the solution.The length of the trajectory is $\sim$ 240 (300) ps for pure water (NaCl solution). We note that in the case of the solution, the Na-Cl distance was constrained to be < 6 Å in Ref. [31] to sample ion-pair configurations. From the FPMD trajectories we extracted 500 (285) snapshots by every ~ 0.5 (~ 1) ps for pure water (NaCl solution), which we then used to compute the electronic density of state (EDOS), as well as the projected EDOS, with the Quantum ESPRESSO [137, 235] code, using both the PBE semi-local and dielectric dependent hybrid (DDH) functionals[46]. The DDH functional was previously shown to provide an excellent description of PE spectra at ambient conditions, in good agreement with experimental measurements [5, 224]. In order to model HPT conditions, we used a DDH functional with a fraction of exact exchange (42%) equal to the inverse of the

macroscopic dielectric constant of water at 11 GPa and 1000 K, which was determined to be 2.37 in a recent study [216]. In our electronic structure calculations, we used norm-conserving pseudopotentials [59] to describe the interactions between core and valence electrons, a plane-wave basis set with a kinetic energy cutoff of 60 Ry and only the Γ-point to sample the Brillouin zone.

To predict PE spectra comparable to experiments, the calculation of absolute energies referenced to vacuum is required, and the strategy chosen to do so in our work is described in detail in the next section.

5.2.2 Evaluation of Absolute Orbital Energies

A complete method of obtaining the absolute orbital energies from FPMD simulations can be found in Chapter 2, Section 2.8.

While eigenvalue and total energy differences are well defined, the energies obtained with the plane-wave pseudopotential method for periodic systems are not[5, 115, 116]. In order to obtain absolute energies $\tilde{\varepsilon}_i$, i.e. to refer the electronic energies to vacuum, we evaluate:

$$\tilde{\varepsilon}_i = \varepsilon_i - \Delta V - V_{\text{bulk}} \tag{5.1}$$

where ε_i denotes Kohn-Sham eigenvalues computed for either bulk water or a NaCl solution in periodic plane-wave calculations. The term V_{bulk} is the average electrostatic potential for bulk water samples, which can be easily computed following the procedure outlined in Ref. [117]. Consistent with the results reported in Ref. [5], we found that the value of V_{bulk}, 0.81 eV, is insensitive to the choice of the energy functional.

The term ΔV is the difference between the electrostatic potential in the bulk region of a water sample interfaced with vacuum, and the vacuum region. In previous calculations of PE spectra at ambient conditions, the term ΔV was obtained by carrying out MD simulations of water in contact with vacuum using empirical potentials and then carrying out electronic

structure calculations on the trajectories generated for the water/vacuum slab. However, this scheme is not applicable at HPT, where hot, compressed water in contact with a vacuum region would immediately expand. Hence, here we adopt a different approach to compute ΔV that we call *Slice* and that we compare in Figure 5.1 with other approaches adopted in the literature.

Figure 5.1 illustrates three possible strategies to obtain ΔV, which are summarized below.

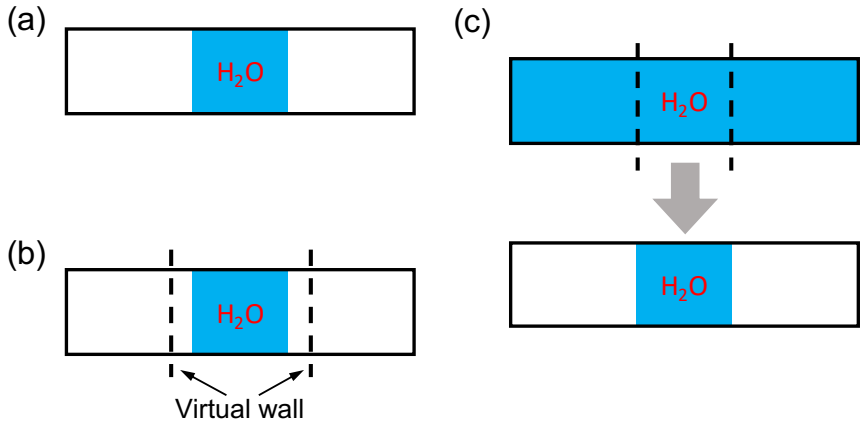

Figure 5.1: Strategies to generate water samples in contact with vacuum: $Vacuum$ (a), $Wall$ (b) and *Slice* (c) (See text). The three rectangles schematically represent a slab used and periodically repeated in our pseudopotential-plane-wave calculations, and the white and blue regions denote vacuum and a water sample, respectively.

- $Vacuum$: A water sample at a chosen, initial density is in contact with vacuum within a periodically repeated slab that is equilibrated using MD at a given temperature. This scheme was used for calculations of PE spectra at APT and is applicable if the density of water is such that immediate evaporation is not observed, over the time scale of the simulations. Hence it is not applicable to simulate water at high P and T, where the sample would tend to expand into vacuum over short time scales.

- $Wall$: Similar to the previous approach, a water sample is in contact with vacuum within a periodically repeated slab that is equilibrated using MD at given temperature.

However in this case a repulsive potential is added to the Hamiltonian so as to maintain the water sample at a density corresponding to the desired pressure. Such a repulsive potential prevents water from evaporating into the vacuum portion of the slab. This method can in principle be used at any $P-T$ conditions, however the results may be affected by the choice of the specific form of the repulsive potential and the approach requires the use of relatively large systems to obtain a converged electrostatic potential.

- *Slice*: A relatively large bulk water model is equilibrated in a periodically repeated supercell at desired P and T conditions. A slice of the sample is then extracted after equilibration and placed in contact with vacuum, with no further MD simulations of the whole slab. To avoid dangling bonds at the interface, when taking the slice, we retain the H-O covalent bonds. This scheme is applicable to any $P-T$ conditions, provided a slice of sufficient thickness is chosen.

To reduce the computational cost in preparing the samples required to obtain ΔV, we carried out simulations with empirical potentials first, for benchmarking purposes, and then we used the deep-MD potential [4, 236] implemented in the DeePMD-kit package [87]. The deep-MD potential (DP) [237] is trained on first principle data obtained with the SCAN functional [238] at HPT and allows for the proper description of dissociated species at extreme conditions, unlike empirical potentials. In addition, using the DP potential, simulations with cells larger than those affordable with FPMD can be carried out and longer time scales can be sampled with first-principle accuracy, as described below.

In order to assess the robustness of our methodology, we first carried our simulations with the TIP3P [239] potential and we compared results obtained with the $Vacuum$ and *Slice* procedures at ambient conditions; we also compared our results with those previously reported in the literature. We then further compared the results obtained with the $Wall$ and *Slice* methods at HPT. MD simulations were carried out in the NVT ensemble with the LAMMPS package [240, 241]. A timestep of 2 (1) fs was used for TIP3P simulations at APT

(11 GPa & 1000 K). When using the $Vacuum$ method, our samples consisted of 108 water molecules interfaced with vacuum in a cell of dimensions 12.77×12.77×80 Å. When using the *Slice* method, we equilibrated water samples with 435 and 683 molecules at APT and 11 GPa & 1000 K, respectively, corresponding to the densities of 1.0 and 1.57 g/cm^3 in a cell of dimensions 12.77×12.77×80 Å. The thickness of a slice was chosen to be 20 (18) Å at APT (11 GPa & 1000 K). When adopting the $Wall$ method, we considered 300 water molecules at 11 GPa & 1000 K, and the $wall/lj126$ scheme implemented in the LAMMPS code. The distance between two virtual walls simulating a repulsive potential in the Hamiltonian was set to be 39 Å. The repulsive part of Lennard-Jones interactions between the wall and water was described by using carbon-oxygen Lennard-Jones parameters [242] to mimic the interaction with water oxygen atoms only. For all the procedures adopted here, the MD simulations with the TIP3P potential were performed for 4 ns following a 2 ns equlibration, with 200 equally-spaced snapshots extracted every 20 ps.

The results for the average potential obtained with the PBE functional on the configurations extracted from our MD simulations are presented in Figure 5.2. Our results with the $Vacuum$ method are nearly identical with those reported using the same scheme in the literature: 3.53 eV versus 3.54 eV [5]. When using the *Slice* method we obtain a value of 3.36 eV and we consider the difference relative to the result with the $Vacuum$ method (0.17 eV) to be negligible, given that the position of the valence band maximum (VBM) of water is at approximately 10 eV [5, 228, 223, 224] relative to vacuum. The difference of 0.17 eV may be ascribed to the specific surface of the chosen slice (the statistical error in our evaluation of ΔV is smaller than 0.1 eV).

At 11 GPa and 1000 K, as reported in Figure 5.2 (b), ΔV is computed to be 5.43 (*Slice*) and 5.58 ($Wall$) eV . Again, we consider the difference of 0.15 eV to be small for the purpose of our study.

Next we compared the results obtained with the *Slice* method and the TIP3P potential

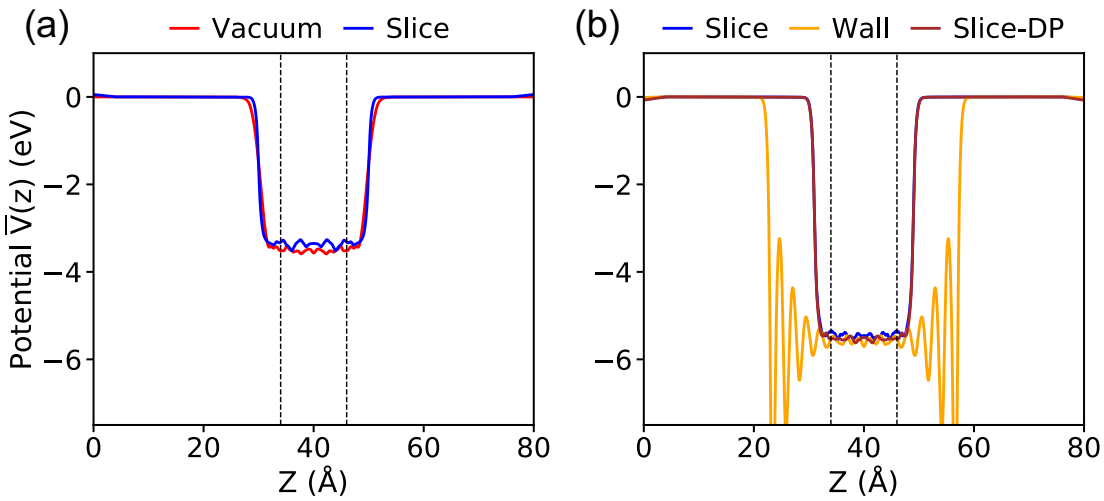

Figure 5.2: Plane-average electrostatic potential $\bar{V}$ along the z direction perpendicular to the interface between water and vacuum, calculated with the PBE functional at ambient conditions (a) and 11 GPa & 1000 K (b). The vacuum level is set to zero. The equilibrium configurations were generated using molecular dynamics simulations and the TIP3P potential except for the case denoted as Slice-DP, for which we used the deep-MD potential [4]. See Figure 5.1 for the definition of different procedures. The dashed lines define the region used for averaging the electrostatic potential.

with those obtained with the DP potential. When using the DP potential, we performed 210 independent MD simulations (with a time step of 0.25 fs) each of 13 ps long, at the end of which we extracted configurations for our electronic structure calculations. We obtained $\Delta V = 5.53$ eV, in good agreement with the value computed with TIP3P, indicating that the value of ΔV depends rather weakly on subtle structural differences in the liquid samples. These comparisons between different approaches gave us confidence that the *Slice* method is a reliable technique to use both at APT and HPT.

Therefore, in the following we compute ΔV with the *Slice* method and the DP potential to obtain the spectra at HPT and to discuss the physical properties of water and the NaCl solution. We note that when using the DDH functional, we could only carry out calculations of ΔV for a small number of configurations (5), much smaller than with the PBE functional. Hence we estimated the difference between ΔV computed with PBE and DDH for those limited number of configurations, and we applied the same difference between the DDH and

PBE result (5.31 vs. 5.53 eV) to all eigenvalues obtained at the DDH level of theory for the bulk samples.

5.3 Results and Discussion

5.3.1 Photo-electron spectra of water and NaCl solution at high pressure and temperature

The PE spectra are evaluated as the EDOS of single-particle eigenvalues referred to vacuum, as an approximation to the electronic binding energies (BE). In Figure 5.3, we compare low and high pressure spectra of the NaCl solution computed at the PBE (left hand side) and DDH (right hand side) level of theory. The positions in energy of peaks' maxima are summarized in Table. 5.1.

Table 5.1: Electron binding energy (eV) of NaCl solution at ambient conditions(APT) and high pressure and temperature (HPT) (11 GPa & 1000 K) obtained with the PBE and DDH functionals. See Figure 5.3 for the labeling of the electronic states.

Method	2p (Na^+)	$2a_1$	3s (Cl^-)	$1b_2$	$3a_1$	$1b_1$	3p (Cl^-)
PBE-APT[a]	26.90	24.71	18.06	12.63	9.03	6.99	6.20
DDH-APT[a]	34.04	32.57	24.15	17.14	13.56	11.34	9.46
PBE-HPT[b]	27.02	24.81	18.62	12.84	8.98	7.12	6.28
DDH-HPT[b]	31.92	30.18	22.93	15.98	12.01	10.02	8.41

[a] Results at APT of a 1 M NaCl solution from Ref. [5].
[b] Results at 11 GPa & 1000 K of a 0.68 M NaCl solution.

The four major peaks (labeled, in order of increasing BE as: $2a_1$, $1b_2$, $3a_1$, and $1b_1$) are notably broadened at HPT, with the $3a_1$ and $1b_1$ features strongly overlapping with each other, consistent with larger structural fluctuations in the HPT samples. The DDH results show that the relative spacing of the water $2a_1$ band with respect to the $1b_1$ peak

is decreased by $\sim$ 1.1 eV at high P, while that of $1b_2$ and $3a_1$ bands are less affected at extreme conditions. Interestingly, calculations with the DDH functional predict a reduction of the BE by roughly 1.1$\sim$2.4 eV at high pressure, depending on the character of electronic states; however calculation with the PBE or standard hybrid functionals such as PBE0 [243, 53] yield negligible differences between the band positions in the PE spectra at high and low pressure. This finding is important and highlights the need to correctly take into account screening effects at HPT and correspondingly adjust the amount of exact exchange used to define hybrid functionals ($\sim$60% in DDH at APT [5, 224]; $\sim$42% in DDH at the HPT conditions of this study, corresponding to the dielectric constants ϵ_∞ = 1.78 and 2.37, respectively).

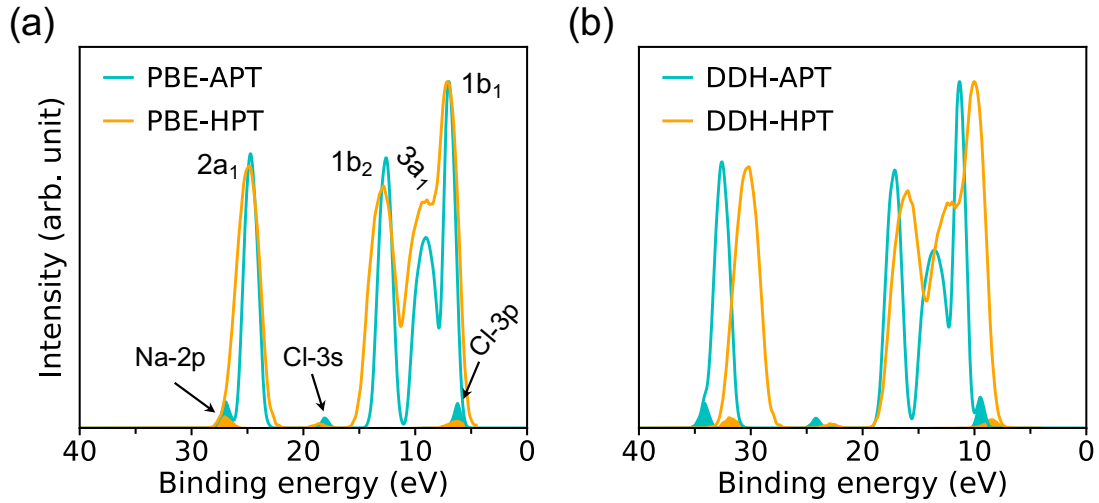

Figure 5.3: Photoelectron spectra of a 1M NaCl solution at ambient conditions (APT) [5] and a 0.68 M NaCl solution at high pressure conditions (HPT) (11 GPa & 1000 K) obtained with the PBE (a) and DDH (b) functionals. The intensities are rescaled to those of the water $1b_1$ peak; the shaded areas show the distribution of ionization potentials of solvated Cl^- and Na^+ ions

The ionization potentials (IPs) of hydrated Cl^- and Na^+ at APT and HPT are indicated in Figure 5.3 as shaded areas. Similar to the BE of water electronic states, the IPs of ions are underestimated by PBE, relative to DDH, and DDH results show a red shift with increasing P and T which is not reproduced by the PBE functional. In addition, when using the DDH

functional, the relative positions of IPs referenced to water is slightly different at low and high P. In particular, the separation between the 3p-level of Cl^- and the $1b_1$ peak of water is decreased by 0.27 eV, suggesting a modified electronic structure near the band edges of water at high P, which in turn may affect the chemical reactivity of solutions under extreme conditions. Our results hint at a possible tendency of anion levels to move below the valence band of water as a function of increasing pressure, at high T. We note that the BE of water and IP of ions are not sensitive to the $Cl^- - Na^+$ distance, hence the results reported here should be representative of weakly concentrated solutions.

5.3.2 Water dissociation

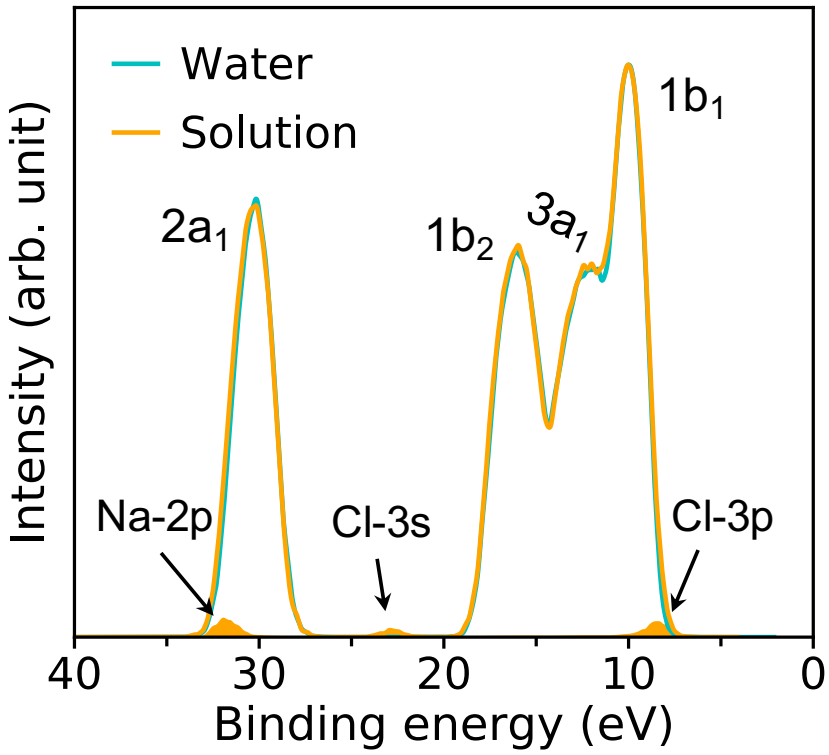

Figure 5.4: Photoelectron spectra of water and a 0.68 M NaCl solution obtained with the DDH functional at 11 GPa & 1000 K. The intensities of the spectra are rescaled to the water $1b_1$ peak; the shaded areas indicate the ionization potential of solvated Cl^- and Na^+ ions.

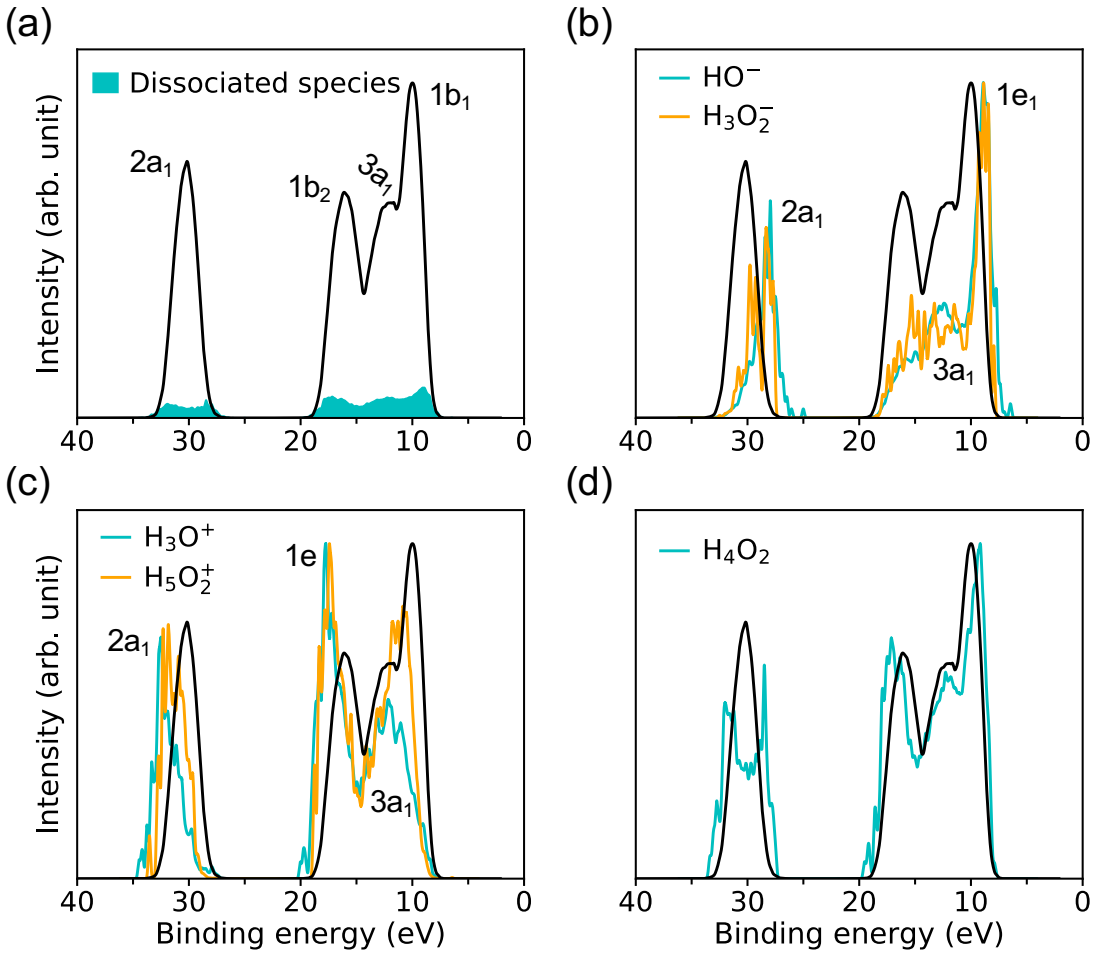

Figure 5.5: Signals of dissociated water species contributing to the photoelectron spectra (PE) of water under pressure, at high temperature, calculated with the DDH functional at 11 GPa & 1000 K. The full spectrum of bulkwater is represented by the black line. (a) The shaded areas (cyan) represent the total PE spectrum from all dissociated species (magnified five times for clarity). The intensities in (b) HO^- and $H_3O_2^-$, (c) H_3O^+ and $H_5O_2^+$, (d) H_4O_2 are magnified between $\sim$ 100 (e.g. HO^- and H_4O_2) and $\sim$1000 (e.g. $H_3O_2^-$) times.

Figure 5.4 compares the spectra obtained at HPT for water and the solution. We find that the effects of ions on the electronic properties of water are minor at the concentrations considered here (0.68∼1 M) [224]; for example, the centers of the $1b_1$ and $1b_2$ peaks obtained in HPT water and in the solutions with the DDH functional differ by only 0.03 and 0.13 eV, respectively.

In our FPMD simulations, we directly observe frequent dissociation events at HPT, indicating that water itself becomes an electrolyte. The short-lived dissociated products [30, 31] are characterized using a cutoff distance for O-H bonds of 1.25 Å. A detailed analysis reveals that about 2% of water molecules are dissociated, into species including solvated HO^-, H_3O^+ and H_4O_2. These species play a critical role in proton transfer events and acid-base reactions in water.

As shown in Figure 5.5 (a), the signal coming from ionic species resulting from water dissociation spans the entire spectrum range. The signal is weak and expected to become more prominent at higher pressure and temperature, where the concentration of dissociated species will increase. The contributions to the overall PE signal of hydrated HO^- and H_3O^+ are presented in Figure 5.5 (b) and (c), and it has been identified by carrying out projected EDOS calculations. Similar to ambient conditions, the solvated HO^- level is just above the VBM of water, and it originates from two degenerate lone-pair orbitals ($1e_1$) localized on the oxygen atom. The solvated H_3O^+ levels lie instead close to the high-energy edge of the $1b_2$ feature of bulk water and originates from the ionization from two degenerate covalent orbitals with mainly p-character (1e). However the IPs of hydrated HO^- and H_3O^+ at HPT, peaking at 8.9 and 17.75 eV, are red-shifted relative to ambient conditions, where they are centered at $\sim$ 9.2 and $\sim$ 20 eV ($\sim$ 9.99 and $\sim$ 19.01 eV) in the experiments of Ref. [223] (calculated by many-body perturbation approach [228]). In addition, the separation between $1e_1$ level of HO^- and $1b_1$ peak of water is $\sim$ 1.91 eV at APT based on experiment [223], while we find that at HPT is 1.12 eV, when using DDH. Hence our simulations show that

similar to the case of the Cl^-, the level of HO^- gets closer to the VBM of water as pressure is increased.

To understand the electronic states involved in proton transfer events at high pressure, we plot the IP distributions for three hydrated intermediate complexes $H_3O_2^-$, $H_5O_2^+$ and H_4O_2 in Figure 5.5 (b-d). With respect to HO^-, the IP of $H_3O_2^-$ is blueshifted with a slightly enhanced signal near the $1b_2$ region of bulk water, similar to what found in proton transfer events at APT [228]. Compared to H_3O^+, we observe a red shift in the IP of $H_5O_2^+$ with increased spectral weights near the $1b_1$ region of bulk water, again similar to what observed in proton transfer events at APT [228]. For solvated H_4O_2 cluster referenced to bulk water, the major change at high pressure is the double-peak near the $2a_1$ region of bulk water, giving rise to the $2a_1$ peaks with lower or higher IP in the resulting species HO^- and H_3O^+. The results reported here for ionization potentials of dissociated species in water may help, at least qualitatively, to understand proton transfer reactions at high pressure.

5.4 Conclusions

In summary, we proposed a new computational scheme to evaluate photo-electron spectra of water and simple aqueous solutions at high P and T (HPT). By combining deep-MD and first-principles simulations, and electronic structure calculations with hybrid functionals, we computed the absolute orbital energies of water and a 0.68 M NaCl solution at 11 GPa and 1000K, which are conditions relevant to the earth mantle. We found a broadening of the spectra relative to ambient conditions, particularly prominent for the merging of the $3a_1$ and $1b_1$ peaks of water. In addition we found an overall red shift of the HPT spectra relative to ambient conditions, which is however not constant over the whole energy range and varies between 1.1 and 2.4 eV. Our results also show that the anion energy levels are closer to the VBM of water at high pressure and temperature and we speculate that as P and T are increased, the "defect levels" of Cl^- and OH^- in water may eventually lie below the valence

band maximum. We also characterized the IP of hydrated species deriving from rapid water dissociation, e.g. hydrated hydroxide and hydronium, and elucidated the electronic states associated with proton transfer events at high pressure. Our results represent a first step in predicting the electronic properties of solutions in super-critical conditions. Finally we note that the prediction of hybrid and PBE functionals for the electronic properties of the APT and HPT fluids are markedly different; in addition PBE predicts no notable changes between high and low pressure spectra, at variance with dielectric dependent hybrid functionals, when used with a screening fraction computed for the specific HPT conditions investigated here.

CHAPTER 6

SUMMARY AND OUTLOOK

Summary and Outlook

This thesis provides a comprehensive investigation of the electronic and structural properties of two aqueous systems that hold both fundamental and applied significance: (1) a silicon/water interface and (2) water under extreme conditions. We studied these systems utilizing first-principles simulations based on DFT, and we performed detailed comparisons with experiments.

In our exploration of electrified aqueous interfaces, we unraveled the effects of solvation and electric fields on the electronic properties of silicon/water interfaces and we compared our calculations with experimentally measured electrochemical currents. Our simulations revealed that the capacitive current depends on the strength of the applied electric field, while the Faradaic currents are related to the presence of surface defect sites. Our study introduced a computational protocol enabling the systematic exploration of how experimentally adjustable parameters affect the performance of electronic devices, particularly those related to transient electronics and biomodulations.

We then studied the vibrational signatures of water at the silicon interface. We identified hydrogen bonding (HB) configurations of water molecules at the interface and correlated them with vibrational modes observed in computed Raman spectra. Our findings illustrate how the interplay of surface and applied electric fields (positive or negative) can individually disrupt or facilitate the formation of specific HBs. Overall, the analysis of time-series data provided molecular-level insights into the structural behavior of interfacial water, a critical factor influencing surface redox reactions in photoelectrochemical cells.

Our research on the behavior of water and aqueous solutions under extreme conditions mainly focused on the electronic properties of these systems, which are challenging to study

experimentally. We introduced a computational approach to predict the photoelectron spectra of water and a NaCl solution under conditions relevant to the Earth's interior. We found that the resulting spectra exhibit a significant broadening compared to ambient conditions, attributed to enhanced structural fluctuations in HPT water. When using a hybrid functional (DDH), we observed an overall red shift in the photoelctron spectra of HPT water relative to those obtained under ambient conditions. Our results highlighted the importance of accounting for screening effects to obtain the electronic properties of HPT water, which semi-local density functional cannot describe in a sufficiently accurate manner. Furthermore, we identified connections between proton transfer events in HPT water and the ionization potential of dissociated species in the liquid.

In summary, our research on aqueous systems has explored structural, vibrational and electronic properties at the microscopic scale and identified strategies to compare simulations data with experiments. The methods used in this thesis to study interfaces are general and applicable to other semiconducting and insulating aqueous interfaces and may be used in modeling complex electrochemical systems that involve surface reactions and defects. Our study on HPT water represents a first step towards predicting the electronic properties of aqueous solutions under supercritical conditions, where experimental measurements are often unavailable. The computational methods introduced in our work hold significant promise, enabling further investigations into the redox chemistry of other deep-earth aqueous solutions under various pressure and temperature conditions. They may also be integrated with the methods used and developed here for interfaces to understand the electronic and vibrational properties of HPT aqueous interface.

As mentioned in Chapter 2, the incorporation of machine learning (ML) methods into molecular simulations has brought about an important transformation in the field of quantum chemistry and computational materials [244, 88]. One interesting direction relevant to our research is the development of ML potentials (MLPs) for aqueous interfaces with

long-range electrostatic interactions. While many existing MLPs successfully predict atomic structures and forces based on the locality assumption [83], when studying heterogeneous systems, especially solid/water interfaces under the effect of electric fields, it becomes essential to account for the long-range interactions between polar and charged molecules. In such cases, the current MLPs, which primarily focus on short-range geometric information, may introduce quantitative errors when describing polarization and dielectric properties. Work has been done to develop MLPs that capture both short-range interactions and long-range electrostatics, although their application so far has been restricted to liquid water [245, 246, 247]. Another challenge in deriving accurate ML potentials — the use of which could in principle alleviate the time scale problem encountered in our FPMD simulations — is the choice of the exchange and correlation potential to generate data for the training set. The search for exchange and correlation potentials to accurately simulate the properties of interfaces, especially their electronic properties [248] is an active field of research, as is the generation of training sets using higher-level electronic structure theories. Recent advances have demonstrated a data-efficient training approach to generate MLPs with coupled cluster singles, doubles and perturbative triples, CCSD(T) or Auxiliary Field Quantum Monte Carlo, AFQMC-level accuracy [249, 250], but their applications have also been limited to small water clusters. Overall, the progress in MLPs aimed at achieving precise calculations of aqueous systems holds the potential to significantly impact the field of interfacial simmulations [251, 252].

In addition to MLPs, multiscale modeling offers another promising approach to gain insights into aqueous interfaces in electrochemical devices [253] not only at the miscroscopic scale, but also at the mesoscopic and perhaps macrosocpic scale. In this thesis, we employed first-principles simulations and compared them to surface-sensitive measurements to understand microscopic phenomena at the aqueous interface with atomic-level precision. However, due to the inherent multiscale nature of electrochemical processes, one would need

to go beyond the level of theory adopted here to simulate additional properties of interest for applications [254, 255], including coarse-grained methods [256, 257]. By integrating these diverse modeling approaches, one may eventually navigate the complexities of electrochemical systems, and gain a deeper understanding of aqueous interfaces at multiple length and time scales.

REFERENCES

[1] Yuanwen Jiang, Xiaojian Li, Bing Liu, Jaeseok Yi, Yin Fang, Fengyuan Shi, Xiang Gao, Edward Sudzilovsky, Ramya Parameswaran, Kelliann Koehler, et al. Rational design of silicon structures for optically controlled multiscale biointerfaces. *Nature biomedical engineering*, 2(7):508–521, 2018.

[2] Viktor Rozsa, Tuan Anh Pham, and Giulia Galli. Molecular polarizabilities as fingerprints of perturbations to water by ions and confinement. *The Journal of Chemical Physics*, 152(12), 2020.

[3] Cui Zhang, Jun Wu, Giulia Galli, and François Gygi. Structural and vibrational properties of liquid water from van der waals density functionals. *Journal of chemical theory and computation*, 7(10):3054–3061, 2011.

[4] Linfeng Zhang, Jiequn Han, Han Wang, Roberto Car, and EJPRL Weinan. Deep potential molecular dynamics: a scalable model with the accuracy of quantum mechanics. *Physical review letters*, 120(14):143001, 2018.

[5] Alex P Gaiduk, Marco Govoni, Robert Seidel, Jonathan H Skone, Bernd Winter, and Giulia Galli. Photoelectron spectra of aqueous solutions from first principles. *Journal of the American Chemical Society*, 138(22):6912–6915, 2016.

[6] Richard G Taylor, Bridget Scanlon, Petra Döll, Matt Rodell, Rens Van Beek, Yoshihide Wada, Laurent Longuevergne, Marc Leblanc, James S Famiglietti, Mike Edmunds, et al. Ground water and climate change. *Nature climate change*, 3(4):322–329, 2013.

[7] UN Water. Water and climate change. *The United Nations World Water Development Report*, 2020.

[8] Edward Barry, Raelyn Burns, Wei Chen, Guilhem X De Hoe, Joan Manuel Montes De Oca, Juan J De Pablo, James Dombrowski, Jeffrey W Elam, Alanna M Felts, Giulia Galli, et al. Advanced materials for energy-water systems: the central role of water/solid interfaces in adsorption, reactivity, and transport. *Chemical Reviews*, 121(15):9450–9501, 2021.

[9] Olle Bjorneholm, Martin H Hansen, Andrew Hodgson, Li-Min Liu, David T Limmer, Angelos Michaelides, Philipp Pedevilla, Jan Rossmeisl, Huaze Shen, Gabriele Tocci, et al. Water at interfaces. *Chemical reviews*, 116(13):7698–7726, 2016.

[10] Craig E Manning. Fluids of the lower crust: deep is different. *Annual Review of Earth and Planetary Sciences*, 46:67–97, 2018.

[11] Tobias Morawietz, Andreas Singraber, Christoph Dellago, and Jörg Behler. How van der waals interactions determine the unique properties of water. *Proceedings of the National Academy of Sciences*, 113(30):8368–8373, 2016.

[12] Javier Carrasco, Andrew Hodgson, and Angelos Michaelides. A molecular perspective of water at metal interfaces. *Nature materials*, 11(8):667–674, 2012.

[13] Rusong Chen, Qinghao Li, Xiqian Yu, Liquan Chen, and Hong Li. Approaching practically accessible solid-state batteries: stability issues related to solid electrolytes and interfaces. *Chemical reviews*, 120(14):6820–6877, 2019.

[14] Martin R Busche, Thomas Drossel, Thomas Leichtweiss, Dominik A Weber, Mareike Falk, Meike Schneider, Maria-Louisa Reich, Heino Sommer, Philipp Adelhelm, and Jürgen Janek. Dynamic formation of a solid-liquid electrolyte interphase and its consequences for hybrid-battery concepts. *Nature chemistry*, 8(5):426–434, 2016.

[15] Takashi Hisatomi, Jun Kubota, and Kazunari Domen. Recent advances in semiconductors for photocatalytic and photoelectrochemical water splitting. *Chemical Society Reviews*, 43(22):7520–7535, 2014.

[16] Wennie Wang, Marco Favaro, Emily Chen, Lena Trotochaud, Hendrik Bluhm, Kyoung-Shin Choi, Roel van de Krol, David E Starr, and Giulia Galli. Influence of excess charge on water adsorption on the bivo4 (010) surface. *Journal of the American Chemical Society*, 144(37):17173–17185, 2022.

[17] Chaoran Jiang, Savio JA Moniz, Aiqin Wang, Tao Zhang, and Junwang Tang. Photoelectrochemical devices for solar water splitting–materials and challenges. *Chemical Society Reviews*, 46(15):4645–4660, 2017.

[18] Andre E Nel, Lutz Mädler, Darrell Velegol, Tian Xia, Eric MV Hoek, Ponisseril Somasundaran, Fred Klaessig, Vince Castranova, and Mike Thompson. Understanding biophysicochemical interactions at the nano–bio interface. *Nature materials*, 8(7):543–557, 2009.

[19] Min Song, Xiaogang Lin, Zhijia Peng, Shibin Xu, Lifeng Jin, Xiaodong Zheng, and Haoyue Luo. Materials and methods of biosensor interfaces with stability. *Frontiers in Materials*, 7:583739, 2021.

[20] Simiao Niu, Naoji Matsuhisa, Levent Beker, Jinxing Li, Sihong Wang, Jiechen Wang, Yuanwen Jiang, Xuzhou Yan, Youngjun Yun, William Burnett, et al. A wireless body area sensor network based on stretchable passive tags. *Nature Electronics*, 2(8):361–368, 2019.

[21] Jian-ming Zheng, Wei-Chun Chin, Eugene Khijniak, Eugene Khijniak Jr, and Gerald H Pollack. Surfaces and interfacial water: evidence that hydrophilic surfaces have long-range impact. *Advances in colloid and interface science*, 127(1):19–27, 2006.

[22] Tuan Anh Pham, Donghwa Lee, Eric Schwegler, and Giulia Galli. Interfacial effects on the band edges of functionalized si surfaces in liquid water. *Journal of the American Chemical Society*, 136(49):17071–17077, 2014.

[23] Ding Pan and Giulia Galli. The fate of carbon dioxide in water-rich fluids under extreme conditions. *Science Advances*, 2(10):e1601278, 2016.

[24] Nore Stolte, Rui Hou, and Ding Pan. Nanoconfinement facilitates reactions of carbon dioxide in supercritical water. *Nature Communications*, 13(1):5932, 2022.

[25] Alexander F Goncharov, Nir Goldman, Laurence E Fried, Jonathan C Crowhurst, I-Feng W Kuo, Christopher J Mundy, and Joseph M Zaug. Dynamic ionization of water under extreme conditions. *Physical review letters*, 94(12):125508, 2005.

[26] Richard L Smith Jr and Zhen Fang. Techniques, applications and future prospects of diamond anvil cells for studying supercritical water systems. *The Journal of Supercritical Fluids*, 47(3):431–446, 2009.

[27] Walter Kohn and Lu Jeu Sham. Self-consistent equations including exchange and correlation effects. *Physical review*, 140(4A):A1133, 1965.

[28] Richard M Martin. *Electronic structure: basic theory and practical methods*. Cambridge university press, 2020.

[29] Richard Car and Mark Parrinello. Unified approach for molecular dynamics and density-functional theory. *Physical review letters*, 55(22):2471, 1985.

[30] Viktor Rozsa, Ding Pan, Federico Giberti, and Giulia Galli. Ab initio spectroscopy and ionic conductivity of water under earth mantle conditions. *Proceedings of the National Academy of Sciences*, 115(27):6952–6957, 2018.

[31] Cunzhi Zhang, Federico Giberti, Emre Sevgen, Juan J de Pablo, Francois Gygi, and Giulia Galli. Dissociation of salts in water under pressure. *Nature communications*, 11(1):3037, 2020.

[32] VI Ivashchenko, VI Shevchenko, and PEA Turchi. First-principles study of the atomic and electronic structures of crystalline and amorphous b 4 c. *Physical Review B*, 80(23):235208, 2009.

[33] Bo Xiao and Satoshi Watanabe. Oxygen vacancy effects on an amorphous-tao x-based resistance switch: A first principles study. *Nanoscale*, 6(17):10169–10178, 2014.

[34] Pierre Hohenberg and Walter Kohn. Inhomogeneous electron gas. *Physical review*, 136(3B):B864, 1964.

[35] Ivo Souza, Jorge Íniguez, and David Vanderbilt. First-principles approach to insulators in finite electric fields. *Physical review letters*, 89(11):117602, 2002.

[36] Zifan Ye, Aleksander Prominski, Bozhi Tian, and Giulia Galli. Probing the electronic properties of the electrified silicon/water interface by combining simulations and experiments. *Proceedings of the National Academy of Sciences*, 118(46):e2114929118, 2021.

[37] Michael G Walter, Emily L Warren, James R McKone, Shannon W Boettcher, Qixi Mi, Elizabeth A Santori, and Nathan S Lewis. Solar water splitting cells. *Chemical reviews*, 110(11):6446–6473, 2010.

[38] Yingying Wang, Jingnan Zhang, M-S Balogun, Yexiang Tong, and Yongchao Huang. Oxygen vacancy–based metal oxides photoanodes in photoelectrochemical water splitting. *Materials Today Sustainability*, 18:100118, 2022.

[39] Yao He, Chunhai Fan, and Shuit-Tong Lee. Silicon nanostructures for bioapplications. *Nano Today*, 5(4):282–295, 2010.

[40] DP Fernandez, ARH Goodwin, Eric W Lemmon, JMH Levelt Sengers, and RC Williams. A formulation for the static permittivity of water and steam at temperatures from 238 k to 873 k at pressures up to 1200 mpa, including derivatives and debye–hückel coefficients. *Journal of Physical and Chemical Reference Data*, 26(4):1125–1166, 1997.

[41] Steven Y Reece, Jonathan A Hamel, Kimberly Sung, Thomas D Jarvi, Arthur J Esswein, Joep JH Pijpers, and Daniel G Nocera. Wireless solar water splitting using silicon-based semiconductors and earth-abundant catalysts. *science*, 334(6056):645–648, 2011.

[42] Paul L Stiles, Jon A Dieringer, Nilam C Shah, and Richard P Van Duyne. Surface-enhanced raman spectroscopy. *Annu. Rev. Anal. Chem.*, 1:601–626, 2008.

[43] Quan Wan, Leonardo Spanu, Giulia A Galli, and François Gygi. Raman spectra of liquid water from ab initio molecular dynamics: vibrational signatures of charge fluctuations in the hydrogen bond network. *Journal of chemical theory and computation*, 9(9):4124–4130, 2013.

[44] Zifan Ye, Cunzhi Zhang, and Giulia Galli. Photoelectron spectra of water and simple aqueous solutions at extreme conditions. *Faraday Discussions*, 236:352–363, 2022.

[45] Ding Pan and Giulia Galli. A first principles method to determine speciation of carbonates in supercritical water. *Nature communications*, 11(1):421, 2020.

[46] Jonathan H Skone, Marco Govoni, and Giulia Galli. Self-consistent hybrid functional for condensed systems. *Physical Review B*, 89(19):195112, 2014.

[47] Jonathan H Skone, Marco Govoni, and Giulia Galli. Nonempirical range-separated hybrid functionals for solids and molecules. *Physical Review B*, 93(23):235106, 2016.

[48] Attila Szabo and Neil S Ostlund. *Modern quantum chemistry: introduction to advanced electronic structure theory*. Courier Corporation, 2012.

[49] Emily A Carter. Challenges in modeling materials properties without experimental input. *Science*, 321(5890):800–803, 2008.

[50] John P Perdew, Kieron Burke, and Matthias Ernzerhof. Generalized gradient approximation made simple. *Physical review letters*, 77(18):3865, 1996.

[51] Yingkai Zhang, Wei Pan, and Weitao Yang. Describing van der waals interaction in diatomic molecules with generalized gradient approximations: The role of the exchange functional. *The Journal of chemical physics*, 107(19):7921–7925, 1997.

[52] Aron J Cohen, Paula Mori-Sánchez, and Weitao Yang. Challenges for density functional theory. *Chemical reviews*, 112(1):289–320, 2012.

[53] Carlo Adamo and Vincenzo Barone. Toward reliable density functional methods without adjustable parameters: The pbe0 model. *The Journal of chemical physics*, 110(13):6158–6170, 1999.

[54] Max Dion, Henrik Rydberg, Elsebeth Schröder, David C Langreth, and Bengt I Lundqvist. Van der waals density functional for general geometries. *Physical review letters*, 92(24):246401, 2004.

[55] Jiří Klimeš, David R Bowler, and Angelos Michaelides. Chemical accuracy for the van der waals density functional. *Journal of Physics: Condensed Matter*, 22(2):022201, 2009.

[56] Petr Jurečka, Jiří Šponer, Jiří Černỳ, and Pavel Hobza. Benchmark database of accurate (mp2 and ccsd (t) complete basis set limit) interaction energies of small model complexes, dna base pairs, and amino acid pairs. *Physical Chemistry Chemical Physics*, 8(17):1985–1993, 2006.

[57] E Oran Brigham. *The fast Fourier transform and its applications*. Prentice-Hall, Inc., 1988.

[58] Samuel F Boys and FJMP Bernardi. The calculation of small molecular interactions by the differences of separate total energies. some procedures with reduced errors. *Molecular Physics*, 19(4):553–566, 1970.

[59] DR Hamann, M Schlüter, and C Chiang. Norm-conserving pseudopotentials. *Physical Review Letters*, 43(20):1494, 1979.

[60] Lars Hedin. New method for calculating the one-particle green's function with application to the electron-gas problem. *Physical Review*, 139(3A):A796, 1965.

[61] Mark S Hybertsen and Steven G Louie. First-principles theory of quasiparticles: calculation of band gaps in semiconductors and insulators. *Physical review letters*, 55(13):1418, 1985.

[62] Michiel J van Setten, Florian Weigend, and Ferdinand Evers. The gw-method for quantum chemistry applications: Theory and implementation. *Journal of chemical theory and computation*, 9(1):232–246, 2013.

[63] Dorothea Golze, Marc Dvorak, and Patrick Rinke. The gw compendium: A practical guide to theoretical photoemission spectroscopy. *Frontiers in chemistry*, 7:377, 2019.

[64] Wei Chen and Alfredo Pasquarello. First-principles determination of defect energy levels through hybrid density functionals and gw. *Journal of Physics: Condensed Matter*, 27(13):133202, 2015.

[65] Isaac Tamblyn, Pierre Darancet, Su Ying Quek, Stanimir A Bonev, and Jeffrey B Neaton. Electronic energy level alignment at metal-molecule interfaces with a g w approach. *Physical Review B*, 84(20):201402, 2011.

[66] Joseph W Knight, Xiaopeng Wang, Lukas Gallandi, Olga Dolgounitcheva, Xinguo Ren, J Vincent Ortiz, Patrick Rinke, Thomas Korzdorfer, and Noa Marom. Accurate ionization potentials and electron affinities of acceptor molecules iii: a benchmark of gw methods. *Journal of chemical theory and computation*, 12(2):615–626, 2016.

[67] Fujie Tang, Zhenglu Li, Chunyi Zhang, Steven G Louie, Roberto Car, Diana Y Qiu, and Xifan Wu. Many-body effects in the x-ray absorption spectra of liquid water. *Proceedings of the National Academy of Sciences*, 119(20):e2201258119, 2022.

[68] Juan J De Pablo and Jay D Schieber. *Molecular engineering thermodynamics*. Cambridge University Press, 2014.

[69] Georg Kresse and Jürgen Hafner. Ab initio molecular-dynamics simulation of the liquid-metal–amorphous-semiconductor transition in germanium. *Physical Review B*, 49(20):14251, 1994.

[70] Sandra Luber, Marcella Iannuzzi, and Jürg Hutter. Raman spectra from ab initio molecular dynamics and its application to liquid s-methyloxirane. *The Journal of chemical physics*, 141(9), 2014.

[71] Cui Zhang, Davide Donadio, Francois Gygi, and Giulia Galli. First principles simulations of the infrared spectrum of liquid water using hybrid density functionals. *Journal of chemical theory and computation*, 7(5):1443–1449, 2011.

[72] Edward Ditler and Sandra Luber. Vibrational spectroscopy by means of first-principles molecular dynamics simulations. *Wiley Interdisciplinary Reviews: Computational Molecular Science*, 12(5):e1605, 2022.

[73] Tuan Anh Pham, Yuan Ping, and Giulia Galli. Modelling heterogeneous interfaces for solar water splitting. *Nature materials*, 16(4):401–408, 2017.

[74] Matteo Gerosa, Francois Gygi, Marco Govoni, and Giulia Galli. The role of defects and excess surface charges at finite temperature for optimizing oxide photoabsorbers. *Nature Materials*, 17(12):1122–1127, 2018.

[75] Sencer Selcuk and Annabella Selloni. Facet-dependent trapping and dynamics of excess electrons at anatase tio2 surfaces and aqueous interfaces. *Nature Materials*, 15(10):1107–1112, 2016.

[76] Jia Chen, Ye-Fei Li, Patrick Sit, and Annabella Selloni. Chemical dynamics of the first proton-coupled electron transfer of water oxidation on tio2 anatase. *Journal of the American Chemical Society*, 135(50):18774–18777, 2013.

[77] Shuji Ogata, Nobuko Ohba, and Takahisa Kouno. Multi-thousand-atom dft simulation of li-ion transfer through the boundary between the solid–electrolyte interface and liquid electrolyte in a li-ion battery. *The Journal of Physical Chemistry C*, 117(35):17960–17968, 2013.

[78] Mitchell T Ong, Harsh Bhatia, Attila G Gyulassy, Erik W Draeger, Valerio Pascucci, Peer-Timo Bremer, Vincenzo Lordi, and John E Pask. Complex ion dynamics in carbonate lithium-ion battery electrolytes. *The Journal of Physical Chemistry C*, 121(12):6589–6595, 2017.

[79] Joost VandeVondele, Fawzi Mohamed, Matthias Krack, Jürg Hutter, Michiel Sprik, and Michele Parrinello. The influence of temperature and density functional models in ab initio molecular dynamics simulation of liquid water. *The Journal of chemical physics*, 122(1), 2005.

[80] Thomas D Kuhne, Matthias Krack, and Michele Parrinello. Static and dynamical properties of liquid water from first principles by a novel car- parrinello-like approach. *Journal of chemical theory and computation*, 5(2):235–241, 2009.

[81] Robert A DiStasio, Biswajit Santra, Zhaofeng Li, Xifan Wu, and Roberto Car. The individual and collective effects of exact exchange and dispersion interactions on the ab initio structure of liquid water. *The Journal of chemical physics*, 141(8), 2014.

[82] PH-L Sit and Nicola Marzari. Static and dynamical properties of heavy water at ambient conditions from first-principles molecular dynamics. *The Journal of chemical physics*, 122(20), 2005.

[83] Jörg Behler and Michele Parrinello. Generalized neural-network representation of high-dimensional potential-energy surfaces. *Physical review letters*, 98(14):146401, 2007.

[84] Daniele Dragoni, Thomas D Daff, Gábor Csányi, and Nicola Marzari. Achieving dft accuracy with a machine-learning interatomic potential: Thermomechanics and defects in bcc ferromagnetic iron. *Physical Review Materials*, 2(1):013808, 2018.

[85] Alexander V Shapeev. Moment tensor potentials: A class of systematically improvable interatomic potentials. *Multiscale Modeling & Simulation*, 14(3):1153–1173, 2016.

[86] Zhi Deng, Chi Chen, Xiang-Guo Li, and Shyue Ping Ong. An electrostatic spectral neighbor analysis potential for lithium nitride. *npj computational materials*, 5(1):75, 2019.

[87] Han Wang, Linfeng Zhang, Jiequn Han, and E Weinan. Deepmd-kit: A deep learning package for many-body potential energy representation and molecular dynamics. *Computer Physics Communications*, 228:178–184, 2018.

[88] Oliver T Unke, Stefan Chmiela, Huziel E Sauceda, Michael Gastegger, Igor Poltavsky, Kristof T Schutt, Alexandre Tkatchenko, and Klaus-Robert Muller. Machine learning force fields. *Chemical Reviews*, 121(16):10142–10186, 2021.

[89] Christoph Schran, Fabian L Thiemann, Patrick Rowe, Erich A Müller, Ondrej Marsalek, and Angelos Michaelides. Machine learning potentials for complex aqueous systems made simple. *Proceedings of the National Academy of Sciences*, 118(38):e2110077118, 2021.

[90] Albert P Bartók, Michael J Gillan, Frederick R Manby, and Gábor Csányi. Machine-learning approach for one-and two-body corrections to density functional theory: Applications to molecular and condensed water. *Physical Review B*, 88(5):054104, 2013.

[91] Elizabeth MY Lee, Thomas Ludwig, Boyuan Yu, Aayush R Singh, François Gygi, Jens K Nørskov, and Juan J de Pablo. Neural network sampling of the free energy landscape for nitrogen dissociation on ruthenium. *The Journal of Physical Chemistry Letters*, 12(11):2954–2962, 2021.

[92] Diddo Diddens, Williams Agyei Appiah, Youssef Mabrouk, Andreas Heuer, Tejs Vegge, and Arghya Bhowmik. Modeling the solid electrolyte interphase: Machine learning as a game changer? *Advanced Materials Interfaces*, 9(8):2101734, 2022.

[93] Marcos F Calegari Andrade, Hsin-Yu Ko, Linfeng Zhang, Roberto Car, and Annabella Selloni. Free energy of proton transfer at the water–tio 2 interface from ab initio deep potential molecular dynamics. *Chemical Science*, 11(9):2335–2341, 2020.

[94] Peter S Rice, Zhi-Pan Liu, and P Hu. Hydrogen coupling on platinum using artificial neural network potentials and dft. *The Journal of Physical Chemistry Letters*, 12(43):10637–10645, 2021.

[95] Taiping Hu, Jianxin Tian, Fuzhi Dai, Xiaoxu Wang, Rui Wen, and Shenzhen Xu. Impact of the local environment on li ion transport in inorganic components of solid electrolyte interphases. *Journal of the American Chemical Society*, 145(2):1327–1333, 2022.

[96] Stefano Baroni, Stefano De Gironcoli, Andrea Dal Corso, and Paolo Giannozzi. Phonons and related crystal properties from density-functional perturbation theory. *Reviews of modern Physics*, 73(2):515, 2001.

[97] Quan Wan. *First principles simulations of vibrational spectra of aqueous systems*. PhD thesis, PhD thesis, Ann Arbor, 2015.

[98] Francois Gygi. Architecture of qbox: A scalable first-principles molecular dynamics code. *IBM Journal of Research and Development*, 52(1.2):137–144, 2008.

[99] RW Nunes and Xavier Gonze. Berry-phase treatment of the homogeneous electric field perturbation in insulators. *Physical Review B*, 63(15):155107, 2001.

[100] RD King-Smith and David Vanderbilt. Theory of polarization of crystalline solids. *Physical Review B*, 47(3):1651, 1993.

[101] David Vanderbilt and RD King-Smith. Electric polarization as a bulk quantity and its relation to surface charge. *Physical Review B*, 48(7):4442, 1993.

[102] Ding Pan, Leonardo Spanu, Brandon Harrison, Dimitri A Sverjensky, and Giulia Galli. Dielectric properties of water under extreme conditions and transport of carbonates in the deep earth. *Proceedings of the National Academy of Sciences*, 110(17):6646–6650, 2013.

[103] Quan Wan and Giulia Galli. First-principles framework to compute sum-frequency generation vibrational spectra of semiconductors and insulators. *Physical Review Letters*, 115(24):246404, 2015.

[104] Yuan Ping, Dario Rocca, and Giulia Galli. Electronic excitations in light absorbers for photoelectrochemical energy conversion: first principles calculations based on many body perturbation theory. *Chemical Society Reviews*, 42(6):2437–2469, 2013.

[105] Giuseppe Cassone, Paolo V Giaquinta, Franz Saija, and A Marco Saitta. Liquid methanol under a static electric field. *The Journal of Chemical Physics*, 142(5), 2015.

[106] Giuseppe Cassone, Fabrizio Creazzo, Paolo V Giaquinta, Franz Saija, and A Marco Saitta. Ab initio molecular dynamics study of an aqueous nacl solution under an electric field. *Physical Chemistry Chemical Physics*, 18(33):23164–23173, 2016.

[107] A Marco Saitta, Franz Saija, and Paolo V Giaquinta. Ab initio molecular dynamics study of dissociation of water under an electric field. *Physical review letters*, 108(20):207801, 2012.

[108] Nicola Marzari, Arash A Mostofi, Jonathan R Yates, Ivo Souza, and David Vanderbilt. Maximally localized wannier functions: Theory and applications. *Reviews of Modern Physics*, 84(4):1419, 2012.

[109] Anna Putrino, Daniel Sebastiani, and Michele Parrinello. Generalized variational density functional perturbation theory. *The Journal of Chemical Physics*, 113(17):7102–7109, 2000.

[110] Anna Putrino and Michele Parrinello. Anharmonic raman spectra in high-pressure ice from ab initio simulations. *Physical Review Letters*, 88(17):176401, 2002.

[111] Chunyi Zhang, Cui Zhang, Mohan Chen, Wei Kang, Zhuowei Gu, Jianheng Zhao, Cangli Liu, Chengwei Sun, and Ping Zhang. Finite-temperature infrared and raman spectra of high-pressure hydrogen from first-principles molecular dynamics. *Physical Review B*, 98(14):144301, 2018.

[112] Abduljabar Q Alsayoud, Manga Venkateswara Rao, Angharad N Edwards, Pierre A Deymier, Krishna Muralidharan, BG Potter Jr, Keith Runge, and Pierre Lucas. Structure of zncl2 melt. part i: Raman spectroscopy analysis driven by ab initio methods. *The Journal of Physical Chemistry B*, 120(17):4174–4181, 2016.

[113] Grace M Sommers, Marcos F Calegari Andrade, Linfeng Zhang, Han Wang, and Roberto Car. Raman spectrum and polarizability of liquid water from deep neural networks. *Physical Chemistry Chemical Physics*, 22(19):10592–10602, 2020.

[114] Jian Feng Li, Yi Fan Huang, Yong Ding, Zhi Lin Yang, Song Bo Li, Xiao Shun Zhou, Feng Ru Fan, Wei Zhang, Zhi You Zhou, De Yin Wu, et al. Shell-isolated nanoparticle-enhanced raman spectroscopy. *nature*, 464(7287):392–395, 2010.

[115] T Anh Pham, Cui Zhang, Eric Schwegler, and Giulia Galli. Probing the electronic structure of liquid water with many-body perturbation theory. *Physical Review B*, 89(6):060202, 2014.

[116] Ravishankar Sundararaman and Yuan Ping. First-principles electrostatic potentials for reliable alignment at interfaces and defects. *The Journal of chemical physics*, 146(10), 2017.

[117] Chris G Van de Walle and Richard M Martin. Theoretical calculations of heterojunction discontinuities in the si/ge system. *Physical Review B*, 34(8):5621, 1986.

[118] Gengfeng Zheng, Xuan PA Gao, and Charles M Lieber. Frequency domain detection of biomolecules using silicon nanowire biosensors. *Nano letters*, 10(8):3179–3183, 2010.

[119] Xiaojie Duan, Ruixuan Gao, Ping Xie, Tzahi Cohen-Karni, Quan Qing, Hwan Sung Choe, Bozhi Tian, Xiaocheng Jiang, and Charles M Lieber. Intracellular recordings of action potentials by an extracellular nanoscale field-effect transistor. *Nature nanotechnology*, 7(3):174–179, 2012.

[120] Bozhi Tian, Tzahi Cohen-Karni, Quan Qing, Xiaojie Duan, Ping Xie, and Charles M Lieber. Three-dimensional, flexible nanoscale field-effect transistors as localized bioprobes. *Science*, 329(5993):830–834, 2010.

[121] Ramya Parameswaran, Joao L Carvalho-de Souza, Yuanwen Jiang, Michael J Burke, John F Zimmerman, Kelliann Koehler, Andrew W Philips, Jaeseok Yi, Erin Adams, Francisco Bezanilla, et al. Photoelectrochemical modulation of neuronal activity with free-standing coaxial silicon nanowires. *Biophysical Journal*, 114(3):393a, 2018.

[122] Yuanwen Jiang and Bozhi Tian. Inorganic semiconductor biointerfaces. *Nature Reviews Materials*, 3(12):473–490, 2018.

[123] Marco Favaro, Beomgyun Jeong, Philip N Ross, Junko Yano, Zahid Hussain, Zhi Liu, and Ethan J Crumlin. Unravelling the electrochemical double layer by direct probing of the solid/liquid interface. *Nature communications*, 7(1):12695, 2016.

[124] Chao Zhang, Thomas Sayer, Jürg Hutter, and Michiel Sprik. Modelling electrochemical systems with finite field molecular dynamics. *Journal of Physics: Energy*, 2(3):032005, 2020.

[125] Zachary K Goldsmith, Marcos F Calegari Andrade, and Annabella Selloni. Effects of applied voltage on water at a gold electrode interface from ab initio molecular dynamics. *Chemical Science*, 12(16):5865–5873, 2021.

[126] Luana S Pedroza, Pedro Brandimarte, Alexandre Reily Rocha, and M-V Fernández-Serra. Bias-dependent local structure of water molecules at a metallic interface. *Chemical science*, 9(1):62–69, 2018.

[127] Chao-Yu Li, Jia-Bo Le, Yao-Hui Wang, Shu Chen, Zhi-Lin Yang, Jian-Feng Li, Jun Cheng, and Zhong-Qun Tian. In situ probing electrified interfacial water structures at atomically flat surfaces. *Nature materials*, 18(7):697–701, 2019.

[128] PM Biesheuvel, S Porada, and JE Dykstra. The difference between faradaic and non-faradaic electrode processes. *arXiv preprint arXiv:1809.02930*, 2018.

[129] John A Rogers, Takao Someya, and Yonggang Huang. Materials and mechanics for stretchable electronics. *science*, 327(5973):1603–1607, 2010.

[130] Huihuo Zheng, Marco Govoni, and Giulia Galli. Dielectric-dependent hybrid functionals for heterogeneous materials. *Physical Review Materials*, 3(7):073803, 2019.

[131] Giovanni Bussi, Davide Donadio, and Michele Parrinello. Canonical sampling through velocity rescaling. *The Journal of chemical physics*, 126(1):014101, 2007.

[132] William Dawson and François Gygi. Equilibration and analysis of first-principles molecular dynamics simulations of water. *The Journal of chemical physics*, 148(12):124501, 2018.

[133] Jiří Klimeš, David R Bowler, and Angelos Michaelides. Van der waals density functionals applied to solids. *Physical Review B*, 83(19):195131, 2011.

[134] Michael D LaCount and François Gygi. Ensemble first-principles molecular dynamics simulations of water using the scan meta-gga density functional. *The Journal of Chemical Physics*, 151(16), 2019.

[135] Simon M Sze, Yiming Li, and Kwok K Ng. *Physics of semiconductor devices*. John wiley & sons, 2021.

[136] Marco Govoni and Giulia Galli. Large scale gw calculations. *Journal of chemical theory and computation*, 11(6):2680–2696, 2015.

[137] Paolo Giannozzi, Stefano Baroni, Nicola Bonini, Matteo Calandra, Roberto Car, Carlo Cavazzoni, Davide Ceresoli, Guido L Chiarotti, Matteo Cococcioni, Ismaila Dabo, et al. Quantum espresso: a modular and open-source software project for quantum simulations of materials. *Journal of physics: Condensed matter*, 21(39):395502, 2009.

[138] Allen J Bard, Larry R Faulkner, and Henry S White. *Electrochemical methods: fundamentals and applications*. John Wiley & Sons, 2022.

[139] A Molina and Joaquín González. Pulse voltammetry in physical electrochemistry and electroanalysis. *Monographs in electrochemistry*, 2016.

[140] T Anh Pham, Tianshu Li, Huy-Viet Nguyen, Sadasivan Shankar, Francois Gygi, and Giulia Galli. Band offsets and dielectric properties of the amorphous si3n4/si (100) interface: A first-principles study. *Applied Physics Letters*, 102(24):241603, 2013.

[141] Ralf Hunger, Rainer Fritsche, Bengt Jaeckel, Wolfram Jaegermann, Lauren J Webb, and Nathan S Lewis. Chemical and electronic characterization of methyl-terminated si (111) surfaces by high-resolution synchrotron photoelectron spectroscopy. *Physical Review B*, 72(4):045317, 2005.

[142] Yuan Ping, Ravishankar Sundararaman, and William A Goddard III. Solvation effects on the band edge positions of photocatalysts from first principles. *Physical chemistry chemical physics*, 17(45):30499–30509, 2015.

[143] Jean-Pierre Cloarec, Céline Chevalier, Jonathan Genest, Jacques Beauvais, Hassan Chamas, Yann Chevolot, Thierry Baron, and Abdelkader Souifi. ph driven addressing of silicon nanowires onto si3n4/sio2 micro-patterned surfaces. *Nanotechnology*, 27(29):295602, 2016.

[144] Sergio Trasatti. The absolute electrode potential: an explanatory note (recommendations 1986). *Pure and Applied Chemistry*, 58(7):955–966, 1986.

[145] S Ottow, GS Popkirov, and H Föll. Determination of flat-band potentials of silicon electrodes in hf by means of ac resistance measurements. *Journal of Electroanalytical Chemistry*, 455(1-2):29–37, 1998.

[146] Yuanwen Jiang, Ramya Parameswaran, Xiaojian Li, João L Carvalho-de Souza, Xiang Gao, Lingyuan Meng, Francisco Bezanilla, Gordon MG Shepherd, and Bozhi Tian. Nongenetic optical neuromodulation with silicon-based materials. *Nature protocols*, 14(5):1339–1376, 2019.

[147] Jerry Tersoff and Donald R Hamann. Theory and application for the scanning tunneling microscope. *Physical review letters*, 50(25):1998, 1983.

[148] Jerry Tersoff and Donald R Hamann. Theory of the scanning tunneling microscope. *Physical Review B*, 31(2):805, 1985.

[149] Han Yang, Marco Govoni, and Giulia Galli. Improving the efficiency of g 0 w 0 calculations with approximate spectral decompositions of dielectric matrices. *The Journal of Chemical Physics*, 151(22):224102, 2019.

[150] Wen-Shiang Liao and Si-Chen Lee. Water-induced room-temperature oxidation of si–h and–si–si–bonds in silicon oxide. *Journal of applied physics*, 80(2):1171–1176, 1996.

[151] Dong Liu, Leilei Li, Yang Gao, Chengming Wang, Jun Jiang, and Yujie Xiong. The nature of photocatalytic "water splitting" on silicon nanowires. *Angewandte Chemie International Edition*, 54(10):2980–2985, 2015.

[152] Fang Dai, Jiantao Zai, Ran Yi, Mikhail L Gordin, Hiesang Sohn, Shuru Chen, and Donghai Wang. Bottom-up synthesis of high surface area mesoporous crystalline silicon and evaluation of its hydrogen evolution performance. *Nature communications*, 5(1):3605, 2014.

[153] Maxim V Fedorov and Alexei A Kornyshev. Ionic liquids at electrified interfaces. *Chemical reviews*, 114(5):2978–3036, 2014.

[154] Bingbin Wu, Shanyu Wang, Willie J Evans IV, Daniel Z Deng, Jihui Yang, and Jie Xiao. Interfacial behaviours between lithium ion conductors and electrode materials in various battery systems. *Journal of Materials Chemistry A*, 4(40):15266–15280, 2016.

[155] Martin R Busche, Thomas Drossel, Thomas Leichtweiss, Dominik A Weber, Mareike Falk, Meike Schneider, Maria-Louisa Reich, Heino Sommer, Philipp Adelhelm, and Jürgen Janek. Dynamic formation of a solid-liquid electrolyte interphase and its consequences for hybrid-battery concepts. *Nature chemistry*, 8(5):426–434, 2016.

[156] Dongliang Chao, Wanhai Zhou, Fangxi Xie, Chao Ye, Huan Li, Mietek Jaroniec, and Shi-Zhang Qiao. Roadmap for advanced aqueous batteries: From design of materials to applications. *Science advances*, 6(21):eaba4098, 2020.

[157] Yuanwen Jiang, Xiaojian Li, Bing Liu, Jaeseok Yi, Yin Fang, Fengyuan Shi, Xiang Gao, Edward Sudzilovsky, Ramya Parameswaran, Kelliann Koehler, et al. Rational design of silicon structures for optically controlled multiscale biointerfaces. *Nature biomedical engineering*, 2(7):508–521, 2018.

[158] Xiaojie Duan, Ruixuan Gao, Ping Xie, Tzahi Cohen-Karni, Quan Qing, Hwan Sung Choe, Bozhi Tian, Xiaocheng Jiang, and Charles M Lieber. Intracellular recordings of action potentials by an extracellular nanoscale field-effect transistor. *Nature nanotechnology*, 7(3):174–179, 2012.

[159] Steven Y Reece, Jonathan A Hamel, Kimberly Sung, Thomas D Jarvi, Arthur J Esswein, Joep JH Pijpers, and Daniel G Nocera. Wireless solar water splitting using silicon-based semiconductors and earth-abundant catalysts. *science*, 334(6056):645–648, 2011.

[160] Michael G Walter, Emily L Warren, James R McKone, Shannon W Boettcher, Qixi Mi, Elizabeth A Santori, and Nathan S Lewis. Solar water splitting cells. *Chemical reviews*, 110(11):6446–6473, 2010.

[161] Wennie Wang, Andjela Radmilovic, Kyoung-Shin Choi, and Giulia Galli. Integrating computation and experiment to investigate photoelectrodes for solar water splitting at the microscopic scale. *Accounts of Chemical Research*, 54(20):3863–3872, 2021.

[162] Viktor Rozsa, Tuan Anh Pham, and Giulia Galli. Molecular polarizabilities as fingerprints of perturbations to water by ions and confinement. *The Journal of Chemical Physics*, 152(12):124501, 2020.

[163] Viktor F Rozsa and Giulia Galli. Molecular polarizabilities in aqueous systems from first-principles. *The Journal of Physical Chemistry B*, 125(9):2183–2192, 2021.

[164] Juan-Jesus Velasco-Velez, Cheng Hao Wu, Tod A Pascal, Liwen F Wan, Jinghua Guo, David Prendergast, and Miquel Salmeron. The structure of interfacial water on gold electrodes studied by x-ray absorption spectroscopy. *Science*, 346(6211):831–834, 2014.

[165] Angelo Montenegro, Chayan Dutta, Muhammet Mammetkuliev, Haotian Shi, Bingya Hou, Dhritiman Bhattacharyya, Bofan Zhao, Stephen B Cronin, and Alexander V Benderskii. Asymmetric response of interfacial water to applied electric fields. *Nature*, 594(7861):62–65, 2021.

[166] LF Scatena, MG Brown, and GL Richmond. Water at hydrophobic surfaces: weak hydrogen bonding and strong orientation effects. *Science*, 292(5518):908–912, 2001.

[167] Chao-Yu Li, Jia-Bo Le, Yao-Hui Wang, Shu Chen, Zhi-Lin Yang, Jian-Feng Li, Jun Cheng, and Zhong-Qun Tian. In situ probing electrified interfacial water structures at atomically flat surfaces. *Nature materials*, 18(7):697–701, 2019.

[168] Davide Donadio, Giancarlo Cicero, Eric Schwegler, Manu Sharma, and Giulia Galli. Electronic effects in the ir spectrum of water under confinement. *The Journal of Physical Chemistry B*, 113(13):4170–4175, 2009.

[169] Chao Cai, Kang Liu, Long Zhang, Fangbiao Li, Yao Tan, Pengcheng Li, Yanqiu Wang, Maoyu Wang, Zhenxing Feng, Debora Motta Meira, et al. Atomically local electric field induced interface water reorientation for alkaline hydrogen evolution reaction. *Angewandte Chemie International Edition*, page e202300873, 2023.

[170] Daobin Liu, Xiyu Li, Shuangming Chen, Huan Yan, Changda Wang, Chuanqiang Wu, Yasir A Haleem, Sai Duan, Junling Lu, Binghui Ge, et al. Atomically dispersed platinum supported on curved carbon supports for efficient electrocatalytic hydrogen evolution. *Nature Energy*, 4(6):512–518, 2019.

[171] Yao-Hui Wang, Shisheng Zheng, Wei-Min Yang, Ru-Yu Zhou, Quan-Feng He, Petar Radjenovic, Jin-Chao Dong, Shunning Li, Jiaxin Zheng, Zhi-Lin Yang, et al. In situ raman spectroscopy reveals the structure and dissociation of interfacial water. *Nature*, 600(7887):81–85, 2021.

[172] Christy L Haynes, Adam D McFarland, and Richard P Van Duyne. Surface-enhanced raman spectroscopy, 2005.

[173] Sebastian Schlücker. Surface-enhanced raman spectroscopy: Concepts and chemical applications. *Angewandte Chemie International Edition*, 53(19):4756–4795, 2014.

[174] Jian Feng Li, Yi Fan Huang, Yong Ding, Zhi Lin Yang, Song Bo Li, Xiao Shun Zhou, Feng Ru Fan, Wei Zhang, Zhi You Zhou, De Yin Wu, et al. Shell-isolated nanoparticle-enhanced raman spectroscopy. *nature*, 464(7287):392–395, 2010.

[175] Jaehyeon Kim, Fujia Zhao, Shan Zhou, Kaustubh S Panse, and Yingjie Zhang. Spectroscopic investigation of the structure of a pyrrolidinium-based ionic liquid at electrified interfaces. *The Journal of Chemical Physics*, 156(11):114701, 2022.

[176] Jin-Chao Dong, Xia-Guang Zhang, Valentín Briega-Martos, Xi Jin, Ji Yang, Shu Chen, Zhi-Lin Yang, De-Yin Wu, Juan Miguel Feliu, Christopher T Williams, et al. In situ raman spectroscopic evidence for oxygen reduction reaction intermediates at platinum single-crystal surfaces. *Nature Energy*, 4(1):60–67, 2019.

[177] Chao-Yu Li, Jin-Chao Dong, Xi Jin, Shu Chen, Rajapandiyan Panneerselvam, Alexander V Rudnev, Zhi-Lin Yang, Jian-Feng Li, Thomas Wandlowski, and Zhong-Qun Tian. In situ monitoring of electrooxidation processes at gold single crystal surfaces using shell-isolated nanoparticle-enhanced raman spectroscopy. *Journal of the American Chemical Society*, 137(24):7648–7651, 2015.

[178] Sara Laporte, Fabio Finocchi, Lorenzo Paulatto, Marc Blanchard, Etienne Balan, François Guyot, and Antonino Marco Saitta. Strong electric fields at a prototypical oxide/water interface probed by ab initio molecular dynamics: Mgo (001). *Physical Chemistry Chemical Physics*, 17(31):20382–20390, 2015.

[179] Jia-Bo Le, Ao Chen, Lang Li, Jing-Fang Xiong, Jinggang Lan, Yun-Pei Liu, Marcella Iannuzzi, and Jun Cheng. Modeling electrified pt (111)-had/water interfaces from ab initio molecular dynamics. *Jacs Au*, 1(5):569–577, 2021.

[180] GE Walrafen, MR Fisher, MS Hokmabadi, and W-H Yang. Temperature dependence of the low-and high-frequency raman scattering from liquid water. *The Journal of chemical physics*, 85(12):6970–6982, 1986.

[181] HJ Bakker and JL Skinner. Vibrational spectroscopy as a probe of structure and dynamics in liquid water. *Chemical reviews*, 110(3):1498–1517, 2010.

[182] Donald A McQuarrie. *Statistical mechanics*. Sterling Publishing Company, 2000.

[183] Matthias Ernzerhof and Gustavo E Scuseria. Assessment of the perdew–burke–ernzerhof exchange-correlation functional. *The Journal of chemical physics*, 110(11):5029–5036, 1999.

[184] O Faurskov Nielsen. Low-frequency spectroscopic studies and intermolecular vibrational energy transfer in liquids. *Annual Reports Section" C"(Physical Chemistry)*, 93:57–99, 1996.

[185] Alenka Luzar and David Chandler. Structure and hydrogen bond dynamics of water–dimethyl sulfoxide mixtures by computer simulations. *The Journal of chemical physics*, 98(10):8160–8173, 1993.

[186] Ranber Singh, S Prakash, Nitya Nath Shukla, and R Prasad. Sample dependence of the structural, vibrational, and electronic properties of a- si: H: A density-functional-based tight-binding study. *Physical Review B*, 70(11):115213, 2004.

[187] Sho Imoto, Sotiris S Xantheas, and Shinji Saito. Molecular origin of the difference in the hoh bend of the ir spectra between liquid water and ice. *The Journal of Chemical Physics*, 138(5):054506, 2013.

[188] C Garozzo, RA Puglisi, C Bongiorno, C Spinella, S Mirabella, R Reitano, S Di Marco, M Foti, and S Lombardo. Evolution of sih x hydrides during the phase transition from amorphous to nanocrystalline silicon films. *Journal of Applied Physics*, 111(4):043510, 2012.

[189] GE Walrafen, MS Hokmabadi, and W-H Yang. Raman isosbestic points from liquid water. *The Journal of chemical physics*, 85(12):6964–6969, 1986.

[190] B Auer, R Kumar, JR Schmidt, and JL Skinner. Hydrogen bonding and raman, ir, and 2d-ir spectroscopy of dilute hod in liquid d2o. *Proceedings of the National Academy of Sciences*, 104(36):14215–14220, 2007.

[191] Lin-fan Shen, Bang-an Lu, Yu-yang Li, Jia Liu, Zhi-chao Huang-fu, Hao Peng, Jin-yu Ye, Xi-ming Qu, Jun-ming Zhang, Guang Li, et al. Interfacial structure of water as a new descriptor of the hydrogen evolution reaction. *Angewandte Chemie International Edition*, 59(50):22397–22402, 2020.

[192] Charles CL McCrory, Suho Jung, Ivonne M Ferrer, Shawn M Chatman, Jonas C Peters, and Thomas F Jaramillo. Benchmarking hydrogen evolving reaction and oxygen evolving reaction electrocatalysts for solar water splitting devices. *Journal of the American Chemical Society*, 137(13):4347–4357, 2015.

[193] Kurt Bucher and Ingrid Stober. Fluids in the upper continental crust. *Geofluids*, 10(1-2):241–253, 2010.

[194] Axel Liebscher. Aqueous fluids at elevated pressure and temperature. *Geofluids*, 10(1-2):3–19, 2010.

[195] Andrew Putnis and H Austrheim. Fluid-induced processes: metasomatism and metamorphism. *Geofluids*, 10(1-2):254–269, 2010.

[196] Oliver Tschauner, Shichun Huang, E Greenberg, VB Prakapenka, C Ma, GR Rossman, AH Shen, D Zhang, M Newville, A Lanzirotti, et al. Ice-vii inclusions in diamonds: Evidence for aqueous fluid in earth's deep mantle. *Science*, 359(6380):1136–1139, 2018.

[197] JLR Touret. Fluids in metamorphic rocks. *Lithos*, 55(1-4):1–25, 2001.

[198] Bruce WD Yardley and Robert J Bodnar. Fluids in the continental crust. *Geochemical Perspectives*, 3(1):1–2, 2014.

[199] M Nishi, T Irifune, J Tsuchiya, Y Tange, Y Nishihara, K Fujino, and Y Higo. Stability of hydrous silicate at high pressures and water transport to the deep lower mantle. *Nature Geoscience*, 7(3):224–227, 2014.

[200] Gregory C Beroza and Satoshi Ide. Slow earthquakes and nonvolcanic tremor. *Annual review of Earth and planetary sciences*, 39:271–296, 2011.

[201] Thomas J Shankland and Mark E Ander. Electrical conductivity, temperatures, and fluids in the lower crust. *Journal of Geophysical Research: Solid Earth*, 88(B11):9475–9484, 1983.

[202] RD Hyndman and PM Shearer. Water in the lower continental crust: modelling magnetotelluric and seismic reflection results. *Geophysical Journal International*, 98(2):343–365, 1989.

[203] HAROLD C Helgeson and DAVID H Kirkham. Theoretical prediction of thermodynamic properties of aqueous electrolytes at high pressures and temperatures. iii. equation of state for aqueous species at infinite dilution. *Am. J. Sci.;(United States)*, 276(2), 1976.

[204] John C Tanger and Harold C Helgeson. Calculation of the thermodynamic and transport properties of aqueous species at high pressures and temperatures; revised equations of state for the standard partial molal properties of ions and electrolytes. *American Journal of Science*, 288(1):19–98, 1988.

[205] Dimitri A Sverjensky, Brandon Harrison, and David Azzolini. Water in the deep earth: the dielectric constant and the solubilities of quartz and corundum to 60 kb and 1200 c. *Geochimica et Cosmochimica Acta*, 129:125–145, 2014.

[206] D Dolejš and CE Manning. Thermodynamic model for mineral solubility in aqueous fluids: theory, calibration and application to model fluid-flow systems. *Geofluids*, 10(1-2):20–40, 2010.

[207] Craig E Manning. Thermodynamic modeling of fluid-rock interaction at mid-crustal to upper-mantle conditions. *Reviews in Mineralogy and Geochemistry*, 76(1):135–164, 2013.

[208] James W Johnson, Eric H Oelkers, and Harold C Helgeson. Supcrt92: A software package for calculating the standard molal thermodynamic properties of minerals, gases, aqueous species, and reactions from 1 to 5000 bar and 0 to 1000 c. *Computers & Geosciences*, 18(7):899–947, 1992.

[209] Jan-Marten Huizenga. Thermodynamic modelling of c-o-h fluids. *Lithos*, 55(1-4):101–114, 2001.

[210] David Dolejš. Thermodynamics of aqueous species at high temperatures and pressures: equations of state and transport theory. *Reviews in Mineralogy and Geochemistry*, 76(1):35–79, 2013.

[211] Dionysis I Foustoukos. On the ionic strength and electrical conductivity of crustal brines. *Chemical Geology*, 447:183–190, 2016.

[212] Rui Hou, Yuhui Quan, and Ding Pan. Dielectric constant of supercritical water in a large pressure–temperature range. *The Journal of Chemical Physics*, 153(10):101103, 2020.

[213] Viktor Rozsa and Giulia Galli. Solvation of simple ions in water at extreme conditions. *The Journal of Chemical Physics*, 154(14):144501, 2021.

[214] Martin French, Thomas R Mattsson, and Ronald Redmer. Diffusion and electrical conductivity in water at ultrahigh pressures. *Physical Review B*, 82(17):174108, 2010.

[215] Martin French, Sebastien Hamel, and Ronald Redmer. Dynamical screening and ionic conductivity in water from ab initio simulations. *Physical review letters*, 107(18):185901, 2011.

[216] Ding Pan, Quan Wan, and Giulia Galli. The refractive index and electronic gap of water and ice increase with increasing pressure. *Nature communications*, 5(1):1–6, 2014.

[217] Rudolph A Marcus. On the theory of oxidation-reduction reactions involving electron transfer. i. *The Journal of chemical physics*, 24(5):966–978, 1956.

[218] Rudolph A Marcus and Norman Sutin. Electron transfers in chemistry and biology. *Biochimica et Biophysica Acta (BBA)-Reviews on Bioenergetics*, 811(3):265–322, 1985.

[219] Bernd Winter and Manfred Faubel. Photoemission from liquid aqueous solutions. *Chemical reviews*, 106(4):1176–1211, 2006.

[220] Bernd Winter. Liquid microjet for photoelectron spectroscopy. *Nuclear Instruments and Methods in Physics Research Section A: Accelerators, Spectrometers, Detectors and Associated Equipment*, 601(1-2):139–150, 2009.

[221] Robert Seidel, Stephan Thurmer, and Bernd Winter. Photoelectron spectroscopy meets aqueous solution: studies from a vacuum liquid microjet. *The Journal of Physical Chemistry Letters*, 2(6):633–641, 2011.

[222] Bernd Winter, Ramona Weber, Ingolf V Hertel, Manfred Faubel, Pavel Jungwirth, Eric C Brown, and Stephen E Bradforth. Electron binding energies of aqueous alkali and halide ions: Euv photoelectron spectroscopy of liquid solutions and combined ab initio and molecular dynamics calculations. *Journal of the American Chemical Society*, 127(19):7203–7214, 2005.

[223] Bernd Winter, Manfred Faubel, Ingolf V Hertel, Christian Pettenkofer, Stephen E Bradforth, Barbara Jagoda-Cwiklik, Lukasz Cwiklik, and Pavel Jungwirth. Electron binding energies of hydrated h3o+ and oh-: Photoelectron spectroscopy of aqueous

acid and base solutions combined with electronic structure calculations. *Journal of the American Chemical Society*, 128(12):3864–3865, 2006.

[224] Tuan Anh Pham, Marco Govoni, Robert Seidel, Stephen E Bradforth, Eric Schwegler, and Giulia Galli. Electronic structure of aqueous solutions: Bridging the gap between theory and experiments. *Science advances*, 3(6):e1603210, 2017.

[225] Oliver Link, Esteban Vöhringer-Martinez, Eugen Lugovoj, Yaxing Liu, Katrin Siefermann, Manfred Faubel, Helmut Grubmüller, R Benny Gerber, Yifat Miller, and Bernd Abel. Ultrafast phase transitions in metastable water near liquid interfaces. *Faraday discussions*, 141:67–79, 2009.

[226] E Vöhringer-Martinez, O Link, E Lugovoy, KR Siefermann, F Wiederschein, H Grubmüller, and B Abel. Hydrogen bond dynamics of superheated water and methanol by ultrafast ir-pump and euv-photoelectron probe spectroscopy. *Physical Chemistry Chemical Physics*, 16(36):19365–19375, 2014.

[227] Thomas Gladytz, Bernd Abel, and Katrin R Siefermann. Expansion dynamics of supercritical water probed by picosecond time-resolved photoelectron spectroscopy. *Physical Chemistry Chemical Physics*, 17(7):4926–4936, 2015.

[228] Charles W Swartz and Xifan Wu. Ab initio studies of ionization potentials of hydrated hydroxide and hydronium. *Physical review letters*, 111(8):087801, 2013.

[229] Daniel Opalka, Tuan Anh Pham, Michiel Sprik, and Giulia Galli. The ionization potential of aqueous hydroxide computed using many-body perturbation theory. *The Journal of chemical physics*, 141(3):034501, 2014.

[230] Daniel J Frost. The upper mantle and transition zone. *Elements*, 4(3):171–176, 2008.

[231] Alan Bruce Thompson. Water in the earth's upper mantle. *Nature*, 358(6384):295–302, 1992.

[232] Mohan Chen, Lixin Zheng, Biswajit Santra, Hsin-Yu Ko, Robert A DiStasio Jr, Michael L Klein, Roberto Car, and Xifan Wu. Hydroxide diffuses slower than hydronium in water because its solvated structure inhibits correlated proton transfer. *Nature chemistry*, 10(4):413–419, 2018.

[233] Mark Tuckerman, Kari Laasonen, Michiel Sprik, and Michele Parrinello. Ab initio molecular dynamics simulation of the solvation and transport of hydronium and hydroxyl ions in water. *The Journal of chemical physics*, 103(1):150–161, 1995.

[234] Dominik Marx, Amalendu Chandra, and Mark E Tuckerman. Aqueous basic solutions: hydroxide solvation, structural diffusion, and comparison to the hydrated proton. *Chemical reviews*, 110(4):2174–2216, 2010.

[235] Paolo Giannozzi, Oliviero Andreussi, Thomas Brumme, Oana Bunau, M Buongiorno Nardelli, Matteo Calandra, Roberto Car, Carlo Cavazzoni, Davide Ceresoli, Matteo Cococcioni, et al. Advanced capabilities for materials modelling with quantum espresso. *Journal of physics: Condensed matter*, 29(46):465901, 2017.

[236] Linfeng Zhang, Jiequn Han, Han Wang, Wissam A. Saidi, Roberto Car, and E. Weinan. End-to-end symmetry preserving inter-atomic potential energy model for finite and extended systems. In *Proceedings of the 32nd International Conference on Neural Information Processing Systems*, NIPS'18, page 4441–4451, Red Hook, NY, USA, 2018. Curran Associates Inc.

[237] Linfeng Zhang, Han Wang, Roberto Car, and E Weinan. Phase diagram of a deep potential water model. *Physical Review Letters*, 126(23):236001, 2021.

[238] Jianwei Sun, Adrienn Ruzsinszky, and John P Perdew. Strongly constrained and appropriately normed semilocal density functional. *Physical review letters*, 115(3):036402, 2015.

[239] Daniel J Price and Charles L Brooks III. A modified tip3p water potential for simulation with ewald summation. *The Journal of chemical physics*, 121(20):10096–10103, 2004.

[240] Aidan P Thompson, H Metin Aktulga, Richard Berger, Dan S Bolintineanu, W Michael Brown, Paul S Crozier, Pieter J in't Veld, Axel Kohlmeyer, Stan G Moore, Trung Dac Nguyen, et al. Lammps-a flexible simulation tool for particle-based materials modeling at the atomic, meso, and continuum scales. *Computer Physics Communications*, page 108171, 2021.

[241] Steve Plimpton. Fast parallel algorithms for short-range molecular dynamics. *Journal of computational physics*, 117(1):1–19, 1995.

[242] Gerhard Hummer, Jayendran C Rasaiah, and Jerzy P Noworyta. Water conduction through the hydrophobic channel of a carbon nanotube. *Nature*, 414(6860):188–190, 2001.

[243] John P Perdew, Matthias Ernzerhof, and Kieron Burke. Rationale for mixing exact exchange with density functional approximations. *The Journal of chemical physics*, 105(22):9982–9985, 1996.

[244] Keith T Butler, Daniel W Davies, Hugh Cartwright, Olexandr Isayev, and Aron Walsh. Machine learning for molecular and materials science. *Nature*, 559(7715):547–555, 2018.

[245] Ang Gao and Richard C Remsing. Self-consistent determination of long-range electrostatics in neural network potentials. *Nature communications*, 13(1):1572, 2022.

[246] Jorg Behler. Four generations of high-dimensional neural network potentials. *Chemical Reviews*, 121(16):10037–10072, 2021.

[247] Linfeng Zhang, Han Wang, Maria Carolina Muniz, Athanassios Z Panagiotopoulos, Roberto Car, et al. A deep potential model with long-range electrostatic interactions. *The Journal of Chemical Physics*, 156(12), 2022.

[248] Jiawei Zhan, Marco Govoni, and Giulia Galli. Nonempirical range-separated hybrid functional with spatially dependent screened exchange. *Journal of Chemical Theory and Computation*, 2023.

[249] János Daru, Harald Forbert, Jörg Behler, and Dominik Marx. Coupled cluster molecular dynamics of condensed phase systems enabled by machine learning potentials: Liquid water benchmark. *Physical Review Letters*, 129(22):226001, 2022.

[250] Michael S Chen, Joonho Lee, Hong-Zhou Ye, Timothy C Berkelbach, David R Reichman, and Thomas E Markland. Data-efficient machine learning potentials from transfer learning of periodic correlated electronic structure methods: Liquid water at afqmc, ccsd, and ccsd (t) accuracy. *Journal of Chemical Theory and Computation*, 2023.

[251] Stephan Steinmann, Qing Wang, and Zhi Wei Seh. How machine learning can accelerate electrocatalysis discovery and optimization. *Materials Horizons*, 2023.

[252] Dylan M Anstine and Olexandr Isayev. Machine learning interatomic potentials and long-range physics. *The Journal of Physical Chemistry A*, 127(11):2417–2431, 2023.

[253] Xiao-Hui Yang, Yong-Bin Zhuang, Jia-Xin Zhu, Jia-Bo Le, and Jun Cheng. Recent progress on multiscale modeling of electrochemistry. *Wiley Interdisciplinary Reviews: Computational Molecular Science*, 12(1):e1559, 2022.

[254] Mark F Horstemeyer. Multiscale modeling: a review. *Practical aspects of computational chemistry: methods, concepts and applications*, pages 87–135, 2010.

[255] Xueqing Zhang and Anja Bieberle-Hütter. Modeling and simulations in photoelectrochemical water oxidation: from single level to multiscale modeling. *ChemSusChem*, 9(11):1223–1242, 2016.

[256] Alexander J Pak, Thomas Dannenhoffer-Lafage, Jesper J Madsen, and Gregory A Voth. Systematic coarse-grained lipid force fields with semiexplicit solvation via virtual sites. *Journal of Chemical Theory and Computation*, 15(3):2087–2100, 2019.

[257] S Miertuš, E Scrocco, and J Tomasi. Electrostatic interaction of a solute with a continuum. a direct utilizaion of ab initio molecular potentials for the prevision of solvent effects. *Chemical Physics*, 55(1):117–129, 1981.

[258] FAOSTAT FAO et al. Food and agriculture organization of the united nations. *Rome, URL: http://faostat. fao. org*, 2018.

[259] Adrián Fernández Gavela, Daniel Grajales García, Jhonattan C Ramirez, and Laura M Lechuga. Last advances in silicon-based optical biosensors. *sensors*, 16(3):285, 2016.

[260] Frank Jensen. *Introduction to computational chemistry*. John wiley & sons, 2017.

[261] Lixin Zheng, Mohan Chen, Zhaoru Sun, Hsin-Yu Ko, Biswajit Santra, Pratikkumar Dhuvad, and Xifan Wu. Structural, electronic, and dynamical properties of liquid water by ab initio molecular dynamics based on scan functional within the canonical ensemble. *The Journal of Chemical Physics*, 148(16), 2018.

[262] Mohan Chen, Hsin-Yu Ko, Richard C Remsing, Marcos F Calegari Andrade, Biswajit Santra, Zhaoru Sun, Annabella Selloni, Roberto Car, Michael L Klein, John P Perdew, et al. Ab initio theory and modeling of water. *Proceedings of the National Academy of Sciences*, 114(41):10846–10851, 2017.

[263] Achille Lambrecht, Carlo Massobrio, Mauro Boero, Guido Ori, and Evelyne Martin. Atomic structure of amorphous sin: Combining car–parrinello and born–oppenheimer first-principles molecular dynamics. *Computational Materials Science*, 211:111555, 2022.

[264] D Bruce Buchholz, Qing Ma, Diego Alducin, Arturo Ponce, Miguel Jose-Yacaman, Rabi Khanal, Julia E Medvedeva, and Robert PH Chang. The structure and properties of amorphous indium oxide. *Chemistry of Materials*, 26(18):5401–5411, 2014.

[265] Ferdi Aryasetiawan and Olle Gunnarsson. The gw method. *Reports on Progress in Physics*, 61(3):237, 1998.

[266] Bozhi Tian, Tzahi Cohen-Karni, Quan Qing, Xiaojie Duan, Ping Xie, and Charles M Lieber. Three-dimensional, flexible nanoscale field-effect transistors as localized bioprobes. *Science*, 329(5993):830–834, 2010.

[267] Lasse Jensen, Christine M Aikens, and George C Schatz. Electronic structure methods for studying surface-enhanced raman scattering. *Chemical Society Reviews*, 37(5):1061–1073, 2008.

[268] Jie Wei, Si-Na Qin, Ji Yang, Han-Long Ya, Wei-Hsiang Huang, Hua Zhang, Bing Joe Hwang, Zhong-Qun Tian, and Jian-Feng Li. Probing single-atom catalysts and catalytic reaction processes by shell-isolated nanoparticle-enhanced raman spectroscopy. *Angewandte Chemie International Edition*, 60(17):9306–9310, 2021.

[269] David M Carey and Gerald M Korenowski. Measurement of the raman spectrum of liquid water. *The Journal of chemical physics*, 108(7):2669–2675, 1998.

[270] CJ Fecko, JD Eaves, and A Tokmakoff. Isotropic and anisotropic raman scattering from molecular liquids measured by spatially masked optical kerr effect spectroscopy. *The Journal of chemical physics*, 117(3):1139–1154, 2002.

[271] José A Martinez-Gonzalez, Niall J English, and Aoife A Gowen. Understanding the interface between silicon-based materials and water: Molecular-dynamics exploration of infrared spectra. *AIP Advances*, 7(11):115105, 2017.

[272] Aleksandar R Zeradjanin, George Polymeros, Cigdem Toparli, Marc Ledendecker, Nejc Hodnik, Andreas Erbe, Michael Rohwerder, and Fabio La Mantia. What is the trigger for the hydrogen evolution reaction?–towards electrocatalysis beyond the sabatier principle. *Physical Chemistry Chemical Physics*, 22(16):8768–8780, 2020.

[273] JD Eaves, JJ Loparo, Ch J Fecko, ST Roberts, A Tokmakoff, and PL Geissler. Hydrogen bonds in liquid water are broken only fleetingly. *Proceedings of the National Academy of Sciences*, 102(37):13019–13022, 2005.

[274] François Gygi, Jean-Luc Fattebert, and Eric Schwegler. Computation of maximally localized wannier functions using a simultaneous diagonalization algorithm. *Computer physics communications*, 155(1):1–6, 2003.

[275] Kevin Leung. Surface potential at the air- water interface computed using density functional theory. *The Journal of Physical Chemistry Letters*, 1(2):496–499, 2010.

[276] Alex P Gaiduk, Jeffrey Gustafson, Francois Gygi, and Giulia Galli. First-principles simulations of liquid water using a dielectric-dependent hybrid functional. *The journal of physical chemistry letters*, 9(11):3068–3073, 2018.

[277] Haoxin Mai, Tu C Le, Dehong Chen, David A Winkler, and Rachel A Caruso. Machine learning for electrocatalyst and photocatalyst design and discovery. *Chemical Reviews*, 122(16):13478–13515, 2022.

[278] Albert Musaelian, Simon Batzner, Anders Johansson, Lixin Sun, Cameron J Owen, Mordechai Kornbluth, and Boris Kozinsky. Learning local equivariant representations for large-scale atomistic dynamics. *Nature Communications*, 14(1):579, 2023.

[279] Gerhard Hummer, Lawrence R Pratt, and Angel E Garcia. Free energy of ionic hydration. *The Journal of Physical Chemistry*, 100(4):1206–1215, 1996.

[280] Muralikrishna Raju, Sung-Yup Kim, Adri CT Van Duin, and Kristen A Fichthorn. Reaxff reactive force field study of the dissociation of water on titania surfaces. *The Journal of Physical Chemistry C*, 117(20):10558–10572, 2013.